The Next Generation BioPhotonics Workstation

Bañas, Andrew Rafael

Publication date:
2013

Document Version
Publisher's PDF, also known as Version of record

The Next Generation BioPhotonics Workstation

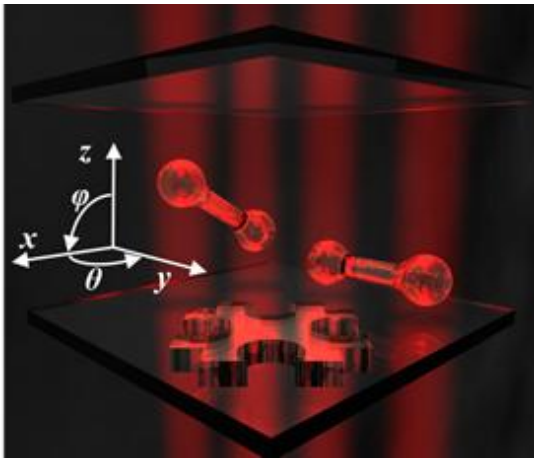

Andrew Rafael M. Bañas
April 15 2013

Department of Phtonics Engineering
Terahertz Technologies and Biophotonics
Technical University of Denmark
DK-2800, Kgs. Lyngby, Denmark
www.ppo.dk

Preface

This thesis presents the work done as part of the requirements of the doctor of philosophy (PhD). The work is done through the period of April 14 2010 to April 14 2013 and have been carried out with the Programmable Phase Optics group (PPO) under the supervision of Jesper Glückstad, Darwin Palima and Peter Uhd Jepsen as co-supervisors, and also in collaboration with the Biological Research Centre of the University of Szeged, and Department of Food Science at Copenhagen University Life Sciences.

Acknowledgements

I would like to thank the people who have contributed to this thesis. The PPO group; Jesper Glückstad, Darwin Palima, Mark Villangca, Thomas Aabo and Lars Rindorf, as well as its former, "transient" and tentative members, Sandeep Tauro, Finn Pedersen, Tomoyo Matsuoka, Marge Maallo. Also other PPO alumni, Peter John Rodrigo, Vincent Daria, Ivan, Jeppe, Carlo Alonzo, whose contributions remain relevant to our present work. The BRC group that hosted my external stay and fabricated the microtools that we trap, Lóránd Kelemen, Pál Ormos, Gaszton Vizsnyiczai, Badri Aekbote, András Búzás. Collaborators at Aarhus University and Copenhagen University as well as the people at the business development side for helping me appreciate the things I build in the laboratory. Rune Christiansen and the rest of DTU Danchip for fabricating our matched filters. And the Danish Research Council (FTP) for funding.

I would also like to express my thanks to my examiners, Tomáš Čižmár and Simon Hanna whose comments have helped improved this thesis. Kirstine Berg-Sørensen, also for the helpful comments and for facilitating practical matters regarding the thesis.

For the less technical aspects that nonetheless contribute to the grand scheme of things, as well as my mental health, I also thank my family for understanding my extended absence, my officemates and neighbours for standing in as co-PhDs, my very kind landlady, Birgit, for not minding all those scattered computers, cables and musical instruments, and the very nice or strange people I meet everyday at work.

Abstract

With its importance in health, medicine and our understanding of how the human body works, biophotonics is recently emerging as an important interdisciplinary field, taking advantage of recent developments in optics and photonics research. In addition to microscopic imaging, methods for shaping light has allowed far more interactive applications such as delivering tailored and localized optical landscapes for stimulating, photo-activating or performing micro-surgery on cells or tissues. In addition to applications possible with light's interaction on biological samples, lights ability to manipulate matter, i.e. optical trapping, brings in a wider tool set in microbiological experiments. Fabricated microscopic tools, such as those constructed using two photon polymerization and other recent nano and microfabrication processes, in turn, allows more complex interactions at the cellular level. It is therefore important to study efficient beam shaping methods, their use in optical trapping and manipulation, and the design of "microtools". Such studies are performed in our BioPhotonics Workstation (BWS). Hence the further development of the BWS is also crucial in supporting these biological studies. We study the use of a novel and robust beam shaping technique, i.e. the matched filtering Generalized Phase Contrast method, and other ways of improving the trapping stability in the BWS, such as using machine vision based feedback. We also present our work on microtools that can deliver highly focused light into cells, i.e. *wave-guided optical waveguides*. Such microtool can be used for triggering local nonlinear processes, performing microscopic laser based surgery. It can also work in reverse for sensing applications. Towards the end, we also present other improvements and applications of the BWS such as using Generalized Phase Contrast to increase its efficiency, imaging cells while external stressors, such as heat are introduced, and adapting the BWS to replace existing bulky and expensive cell sorting systems.

Resumé (Danish abstract)

Med sin betydning inden for sundhed, medicin og vores forståelse af hvordan den menneskelige krop fungerer, fremstår biofotonik-forskningsområdet som et meget vigtigt tværfagligt felt, der udnytter de seneste landvindinger inden for optik, fotonik og biologi. Udover mikroskopisk billeddannelse, har metoder til at forme lys tilladt nye interaktive applikationer såsom levering af skræddersyede og lokaliserede 'optiske landskaber' til stimulering, foto-aktivering eller udførelse af mikro-kirurgi på levende celler og væv. Udover disse applikationer hvor lyset interagerer med biologiske prøver, bringer lys også spændende aktive muligheder for direkte at manipulere stof på mikroskala, dvs optisk trapping og mikro-manipulation i en bredere værktøjskasse til aktive mikrobiologiske forsøg. Fabrikerede mikroskopiske værktøjer vha. 3D printede to-foton polymerisering samt andre nyligt fremkomne nano- og microfabrikations-processer, tilladermulighed for mere komplekse interaktioner på det biologisk cellulære niveau. Det er derfor vigtigt at undersøge de mest effektive metoder til rumlig kodning af lysets bølgefronter og efterflg. anvendelse af disse teknikker til optisk indfangning og manipulation samt i udformningen af såkaldte "microtools" for specifikke mikrobiologiske anvendelser. Sådanne undersøgelser kan udføres på den Biofotoniske Arbejdsstation (BWS). Videreudviklingen af BWS'en er derfor afgørende for at understøtte disse nye mikrobiologiske undersøgelser. I afhandlingen studeres primært brugen af den robuste stråleformningsteknik der kendes som matched filtrering Generalized Phase Contrast (mGPC). Yderligere metoder til at forbedre 'trapping'-stabiliteten på BWSen, såsom brugen af maskin-baseret vision-feedback undersøges også med helt nye eksperimentelle resultater. Afhandlingen præsenterer også forsknings-arbejde med microtools, der kan levere ultraskarpt fokuseret lys direkte ind i levende celler vha. helt nye lys-styrede optiske bølgeledere. Sådanne microtools kan f.eks. anvendes til at eksitere lokale ikke-lineære processer, såsom udførelse af fremtidens mikroskopisk laserbaseret kirurgi og/eller til nano-biofotonisk sensing der ikke tidligere har været muligt. I slutningen af afhandlingen præsenteres yderligere forbedringer og anvendelser af BWS'en såsom brugen af Generalised Phase Contrast til at øge lys-effektiviteten, aktiv billedbehandling af levende celler, mens eksterne stressfaktorer såsom

opvarmning introduceres, samt ikke mindst tilpasningen af BWS-platformen til at erstatte eksisterende klodsede og dyre celle-sorteringssystemer.

Publications

1. S. Tauro, A. Bañas, D. Palima, and J. Glückstad, "Dynamic axial stabilization of counter-propagating beam-traps with feedback control," Optics Express **18**, 18217–22 (2010).
2. A. Bañas, D. Palima, S. Tauro, and J. Glückstad, "Optimizing Light-Matter Interaction on the BioPhotonics Workstation," Opt. Photon. News **4**, 39 (2010).
3. S. Tauro, A. Bañas, D. Palima, and J. Glückstad, "Experimental demonstration of Generalized Phase Contrast based Gaussian beam-shaper.," Optics Express **19**, 7106–11 (2011).
4. T. Aabo, A. R. Bañas, J. Glückstad, H. Siegumfeldt, and N. Arneborg, "BioPhotonics workstation: a versatile setup for simultaneous optical manipulation, heat stress, and intracellular pH measurements of a live yeast cell," The Review of scientific instruments **82**, 083707 (2011).
5. A. R. Bañas, D. Palima, S. Tauro, F. Pedersen, and J. Glückstad, "Bio-optofluidics and biophotonics at the cellular level," DOPS-NYT **26**, 4–9 (2012).
6. D. Palima, A. R. Bañas, G. Vizsnyiczai, L. Kelemen, P. Ormos, and J. Glückstad, "Wave-guided optical waveguides," Optics Express **20**, 2004–14 (2012).
7. A. Bañas, D. Palima, and J. Glückstad, "Matched-filtering generalized phase contrast using LCoS pico-projectors for beam-forming," Optics Express **20**, 9705–12 (2012).
8. D. Palima, A. Bañas, J. Glückstad, G. Vizsnyiczai, L. Kelemen, and P. Ormos, "Mobile Waveguides: Freestanding Waveguides Steered by Light," Opt. Photon. News **23**, 27 (2012).
9. A. R. Bañas, D. Palima, and J. Glückstad, "Robust and Low-Cost Light Shaping," Opt. Photon. News **23**, 50 (2012).
10. D. Palima, A. R. Bañas, G. Vizsnyiczai, L. Kelemen, T. Aabo, P. Ormos, and J. Glückstad, "Optical forces through guided light deflections," Optics Express **21**, 6578–6583 (2013).
11. A. Bañas, T. Aabo, D. Palima, and J. Glückstad, "Matched filtering Generalized Phase Contrast using binary phase for dynamic spot- and line patterns in biophotonics and structured lighting," Optics Express **21**, 388–394 (2013).

Contents

1 Introduction

When the words biology and optics are used in the same context what normally comes to mind are microscopes. Perhaps since microscopes are used in studying microorganisms, cells or tissue structures that are normally invisible to the naked eye, as early as 300 years ago [1]. This capability considerably supplements biological research and also applied sciences such as medicine. In such application light's function, illumination, is rather simple. Although other properties of light such as diffraction were understood at about the same time as microscopy have been used [2], it is not until the introduction of lasers, beam scanners or spatial light modulators that the deliberate shaping of light has been used at micro-biological scales. Thus eventually, scientists learned that there are a lot of other things that can be done *to* light and that can be done *with* light. And with greater control, light's role in biological research is no longer confined to imaging.

1.1 Experiments in the microscopic scale

With micro or nano-fabrication technologies now more developed, there is a trend in technology for things to get smaller. Over the past few years, many of us have seen computing and communication consumer products either become smaller or denser. Miniaturization has also become a trend in fields such as biology and medicine. So called lab-on-a-chip devices [3,4], for example, integrate experimental measurement, sample handling and other functionalities on a chip that can be mounted on a microscope. Aside from taking up less space, smaller setups require less power to operate, less raw materials, and tend to be more efficient in transporting electrons, photons or even cells, as shorter distances are traversed unlike in typical wires, fibers or tubes.

Compared to the observation of clinical symptoms, micro-scale experiments directly observe the cells involved. As basic building blocks, the conditions of cells affect the overall emergent behavior of living organisms. Diagnoses at the cellular level would even provide new insights. For example, diagnosticians can tell what particular "outsiders" are in a blood sample or whether cells look deformed. Such information is far more specific than taking readings of body temperature or heart rate thus leading to more specific treatment which, in turn, is more efficient and

avoids the side effects of broad spectrum medicine. Drugs or other forms of therapy can also be delivered directly to the cells that need it, bypassing the need to circulate all over the body. This specificity, in turn, allows a large array of clinical trials, without requiring populations of people for testing different medication.

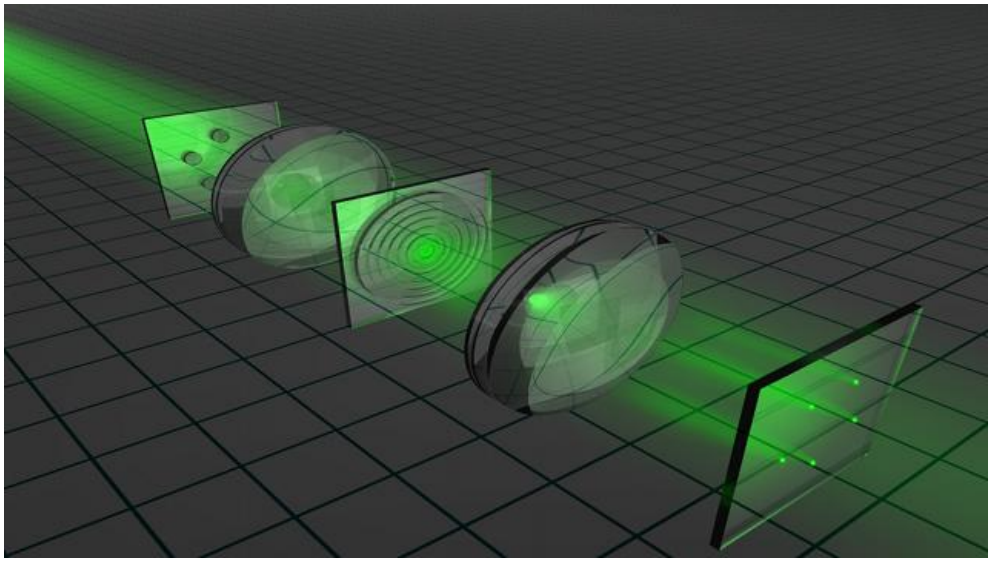

Figure 1.1. The matched filtering Generalized Phase Contrast is a beam shaping technique that is capable of operating on low cost devices such as consumer display projectors due to its tolerance to imperfections such as phase aberrations. Phase patterns at the input are mapped into intensity spikes at the output via phase-only filtering at the Fourier plane.

1.2 Active microscopy through beam shaping

Although, microscopic phenomena can be altered through macroscopic ways, like injecting chemicals into sample chambers, or controlling temperature, there are many instances wherein it is preferable to have localized interactions, i.e. interactions that are isolated from its surroundings. Instead of flooding the whole viewable sample with light, sometimes it is desirable to selectively illuminate just part of the sample. Extraneous light may lead to photobleaching of fluorescent samples or unnecessarily speed up the sample's increase in temperature leading to unwanted effects such as evaporation or even death of living samples. Another example is confocal microscopy wherein image quality is improved by removing light coming from unfocused regions.

Beyond imaging, more complex interactions of light with matter have far more to offer. It is possible for example to ramp up the power, or switch from a continuous to a pulsed laser source to perform laser ablation on cells [5]. Specific organelles within a cell or regions in neurons can be specifically stimulated with pre-shaped light distributions [6,7]. Beam shaping thus supports such biological research. Examples of beam shaping that efficiently shape light via phase-only modulation include diffractive or digital holography and Generalized Phase Contrast (GPC). In addition to Generalized Phase Contrast (GPC) [8] which have been applied in studying neurons and yeast cells [6,9], we have also been studying its variant, matched filtering GPC (mGPC) (Fig. 1.1) due to its robustness to device imperfections that allow it to operate even in low cost consumer projectors [10,11]. Our studies and experiments with mGPC are presented in Chapter 4 of this thesis.

1.3 Optical manipulation

Light has also been used for exerting forces on microscopic particles. At microscopic scales wherein other forces are less dominating, radiation forces resulting from light scattering can be enough to cause motion in microscopic particles. Using real time programmable spatial light modulators (SLM), dynamic beam shaping can therefore be used to control the motion of such particles [12]. Optical manipulation, in turn, offers more experimental possibilities and interaction with the specimens being observed. For example, yeast cells (~5-10μm) can be spatially arranged in a way that modifies their behavior [9]. Manipulation of larger microorganisms (~50-100μm) could be used for taxonomic studies [13]. With microfabrication processes such as two photon polymerization (2PP), optical trapping can also be done on more complex user designed microstructures. For example optical trapping can be used to assemble microscopic puzzle pieces that can serve as biological micro-environments (Fig. 1.2) [14].

Traditionally, mechanical micromanipulators are used together with micropipettes or microscopic extensions of tools in order to physically interact with samples seen under a microscope. These devices consist of precision hydraulic or stepper motor actuators which are costly to build and have limited degrees of operational freedom. Also, unlike light, such devices cannot penetrate through the glass walls of sample slides or chambers. Hence, the idea of using light for mechanical

actuation [15], combined with the versatility of dynamic spatial light modulators [16] for beam shaping, presents both an interesting and flexible means of micromanipulation. Such capabilities bring forth the idea of an active microscope.

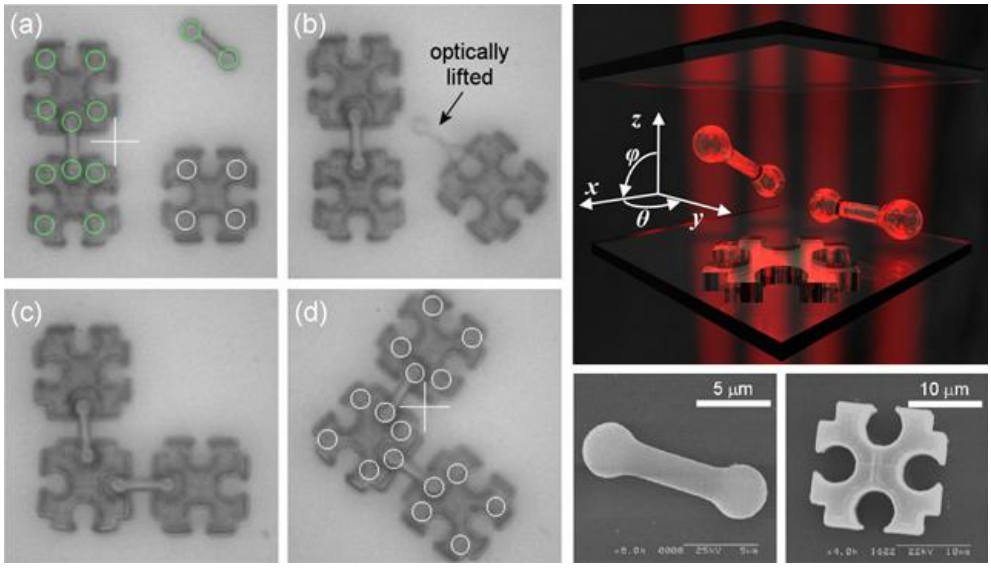

Figure 1.2. Optical manipulation of microscopic puzzle pieces for use in reconfigurable biological microenvironments. The use of a low NA counter-propagating beam geometry allows greater manipulation freedom along the axial direction, leading to 3 dimensional optical trapping. (Figure adapted from [17]).

1.3.1 Counter-propagating beam traps

Many optical manipulation implementations use high numerical aperture (NA) optical tweezers due to the 3D localized gradient forces they provide [18]. Although ideal for stable tweezing, strong localized intensities provided by high NA focusing and limited manipulation ranges go hand in hand. A smaller microbiological "playground" would prevent the manipulation of larger tools or organisms as it leaves less room for moving around. To be free from high NA constraints, we use lower NA optics in conjunction with fast 4*f* mapping based beam shaping methods, such as GPC [19]. Chapter 3 presents the use of counter propagating (CP) beams that enable setting positions over larger axial ranges and suggests novel workarounds for the tradeoffs of having this greater axial control.

Combined with gradient traps also available in HOTs, CP beam traps allow a more pronounced 3D optical manipulation.

1.4 Microtools

Microfabrication via two photon photopolymerization or direct laser writing [20] and other recent techniques, have long been used to create complex microscopic structures [14,21,22]. Instead of just using readily available microspheres, more specific functionalities and biological applications can be implemented if the trapped structures have parts tailored to such applications. The microscopic puzzle pieces used for biological microenvironments (Fig. 1.2) [14] is an early example of this beam shaping and matter shaping synergy. Another example is the use nano-tips with optical handles for performing microscopic optical tomography or force measurements [23,24] akin to atomic force microscopy cantilevers. In addition to precise mechanical probing, highly focused light can also be delivered by integrating free standing waveguides into such microstructure tips (Fig. 1.3) [25]. With beam shaping and optical trapping acting as microscopic "hands", these micorabricated structures serve as light driven tools. Our simulations and experiments with optically manipulated waveguide "microtools", i.e. *wave-guided optical waveguides* [25], are presented in Chapter 5. By enabling targeted and localized complex light-matter interactions, microtools could therefore further advance biophotonics research.

Figure 1.3. Free standing wave-guide microtools that could potentially deliver highly focused light into specific regions within a cell. (Figure adapted from [25]).

1.5 Putting it all together: The BioPhotonics workstation

The BioPhotonics workstation (BWS) [26] combines microscopy, optical micromanipulation and novel beam shaping techniques into an expandable hardware platform for a variety of biological applications. Over the years, the BWS has undergone several iterations, allowing a variety of applications such as micro-spectroscopy, fluorescence imaging and cell sorting. The use of low NA counter-propagating traps, as opposed to tightly focused optical tweezers, has given the BWS more room for wide range interactions. A variety of beam shaping techniques and illumination sources are also being explored to facilitate different requirements such as compactness, cost [10], operating wavelengths, or coupling to microfabricated waveguides [25]. Static beam shaping techniques such as GPC for Gaussian light would also allow efficient light utilization in the BWS's SLM [27]. Some of the BWS's improvements and research applications are presented in the concluding Chapter 6 where planned future work are also presented.

2 A review of beam shaping methods

2.1 Introduction

In one way or another, optical beam shaping lends itself to many applications in biophotonics whether in optical micro-manipulation [28], cell sorting [29], microfabrication [20,21], controlled photo stimulation [6,7], cell surgery [5], or advanced microscopy [30]. Similarly, many light shaping methods are also being developed as the technology of light sources and light modulators progresses. Given such a variety in applications and methods, deciding which beam shaping technique works best for which particular application becomes an important task. For example, depending on the experiment, optical manipulation may either require strong gradient forces for position stability or beams that can manipulate over extended regions as in our BiPhotonics Workstation. Microfabrication, on the other hand, may operate with static beams but would require intense and highly localized light to trigger nonlinear process with high fidelity. In applications like photo-stimulation or neurophotonics, the tolerance of the beam profile to the perturbing biological media can be more important than either reconfiguration speed or power. Other applications that have an effective threshold to the light intensity, like trapping and two photon processes may tolerate a noisy background, provided the foreground intensity is high enough. In addition to the application's sole requirements, practical constraints such as efficiency, budget or setup size are also important decision making factors, especially when developing systems for commercial use or tools for less trained end users who are more concerned with the applications' end results.

This chapter compares some of the techniques for beam shaping, in particular, the ones commonly used in biophotonics applications or optical trapping and manipulation research. Most of the beam shaping techniques discussed here use a form of spatial phase modulation. The exception would be image projection using amplitude modulation which is included for comparison. Phase-only correlation, which uses both amplitude and phase modulation, would also be covered due to its relation to mGPC which is further explored in the Chapter 4.

2.2 Direct imaging of amplitude modulated light

Consumer display devices like LCD screens and projectors are common examples of amplitude modulators of light. Using a simple lens system, direct imaging can be used to project amplitude modulated light on walls as commonly done with LCD projectors. Switching from the widescreen to microscopic experiments, in turn, is just a matter of changing the lenses so that we get a scaled down version of the amplitude pattern instead (under paraxial conditions). For example, commercial display projectors have been used as programmable sample illumination sources, enabling different microscopy modes in the same setup [31]. Despite the relative simplicity, amplitude modulation is generally not preferred for beam shaping, when photon efficiency matters. In amplitude modulation, light is thrown away to create the background needed to define the foreground optical patterns, hence light is wasted. Nevertheless, with sensitivity of eyesight, enough light is left for display or microscopic illumination.

Due to its speed and simplicity of encoding images, amplitude modulation is widely used in consumer products. Video refresh rates, typically 60Hz, are thus achievable, while the lack of strict phase requirements allows the use of cheaper (incoherent) light sources such as mercury or halogen lamps and LEDs. Widely used amplitude modulation techniques include the use of liquid crystals that selectively alter light's polarization for subsequent blocking through a polarizer [32] or the use of micro-mirrors that either deflect or direct incoming light to form an output image [33].

2.3 Digital Holography

Digital or computer generated holography is often used in optical trapping or optical tweezers and has been a favorite application of phase-only SLMs. This technique borrows ideas from holographic recording. But instead of using static holographic films for recording purposes, programmable spatial light modulators are used to dynamically emulate phase distributions that would synthesize the desired optical fields through interference and diffraction. The diffraction patterns formed at the output and the hologram drawn on the SLM are typically related via Fourier transform, allowing instrumentation to use of fast Fourier transforms (FFT).

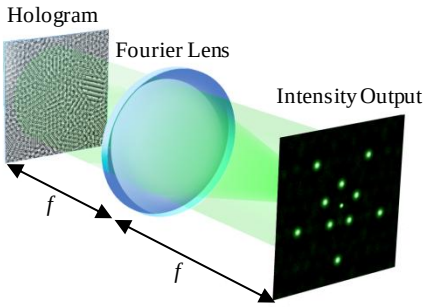

Figure 2.1. Holographic beam shaping based on a 2*f* geometry. Light whose phase is defined by the CGH is Fourier transformed to form target intensity patterns.

The focusing geometry in digital holography effectively gathers a significant amount of light into individual spots, imparting a substantial power in the generated foci. In the simplest case, for example, all light falling on the SLM can be gathered into a single spot. Using high NA objectives, such intense spots are useful for optical tweezing. Holographic patterns can be actuated laterally by adding a linear phase ramp and axially by adding a quadratic lens-like phase to the CGH [34]. The addressing range of a holographic geometry would then be determined by the lens aberrations and the intensity envelope which depends on the SLM's pixel dimensions [35].

One concern that needs to be dealt with when using holographic beam shaping is the occurrence of a strong zero order which is primarily due to limited fill factor and imperfections in SLMs [36]. Light falling into the non-addressable area, i.e. the dead space, would not be modulated, hence ending up in the zero order. The zero order not only uses up light energy, it can also be disturbing to the sample, thus it needs to be dealt with. Besides simply utilizing a region away from the zero order, which would be inefficient, other ways of dealing with it includes blocking at a conjugate plane (e.g. [37]), adding a quadratic phase to the CGH to shift the output plane away from the focal plane [38], using a blazed grating to selectively deflect the higher orders, or destructive interference [36]

In order to fit the boundary conditions imposed by the fixed light source and the desired arbitrary output patterns, numerical calculations of non-trivial CGH distributions [39,40] would be required. In the past, calculation speed of CGHs

used to be a bottleneck for real time interactive output light re-configuration. However, the recent availability of parallel computing via graphical processing unit (GPU) [41] allows a single desktop/latop computer to replace network linked parallel computers making it convenient for small laboratories. Instead of a brute force optimization algorithms such as the Gerchberg-Saxton or direct search algorithms [40], semi-analytic algorithms optimized for spot addressing can incorporate known effects of lens and prism phase distributions [34]. With the current technology, digital holograms now can be calculated as fast as around 2 milliseconds [42] with the experimental bottle neck being the SLM refresh rate.

Although some beams such as Airy, Bessel or Laguerre-Gaussian beams can be conveniently formed via digital holography [43], the creation of contiguous extended arbitrary areas of light would be a challenge in a 2*f* diffractive system given a fixed intensity input. Such contiguous patterns whose amplitude and phase are both well defined would be imposing an input amplitude that may not match the typical laser source profile. Hence, when trying to recreate extended areas, output from CGH would tend to have spurious amplitude and phase discontinuities or speckle noise artifacts. These discontinuous patterns quickly degrade upon propagation preventing its use for applications like extended beam propagation.

2.4 Generalized Phase Contrast

Generalized Phase Contrast (GPC) is an extension to Zernike's phase contrast microscopy designed for beam shaping [8]. With the additional investment of a static phase element, i.e. a phase contrast filter (PCF) and another Fourier lens, the GPC beam shaping method offers advantageous features not available in digital holography. In the GPC method, an input phase pattern is directly mapped into an intensity pattern through a 4*f* filtering configuration. This simpler one-to-one pixel mapping lessens the computational requirements, enabling real-time reconfigurability even with less powerful computers (e.g. a 1.66GHz netbook with 1GB of memory in some of our experiments). With the use of a 4*f* imaging configuration, potentially disturbing light that would have otherwise been spent on the zero-order in a 2*f* CGH setup is utilized as a synthetic reference wave for forming patterns at the output via self interference. Furthermore, since the output has a flat phase profile, GPC becomes convenient for certain volume oriented

applications such as counter propagating optical traps mainly used in the BWS [26,28].

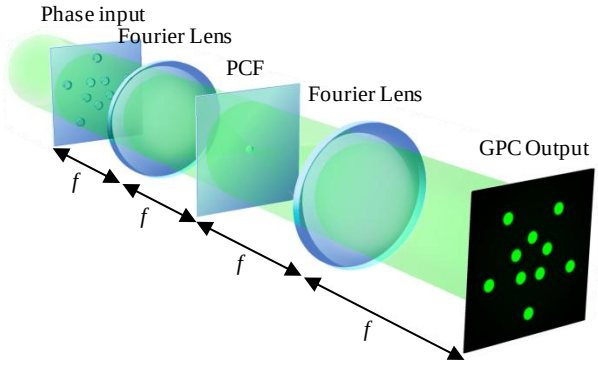

Figure 2.2. A Generalized Phase Contrast setup. Phase input patterns are mapped into output intensity patterns via common path interferometry.

Besides disk shaped beam profiles, more complex patterns such the shape of a neuron's dendrites can be addressed contiguously while propagating through less uniform biological media [6]. The flat phase of GPC shaped light also makes it easy to combine with more complex beam shaping techniques like temporal focusing [6]. It can also act as a shapeable light source relayed to another diffractive holographic setup, thus allowing more freedom in defining the output's amplitude and phase [44]. Although similar in operation to Bartelt's tandem setup [45], GPC's flat phase output would be easier to align to the secondary phase element. GPC's 4*f* mapping scheme also allows binary[2] SLMs to be used without dealing with mirrored "ghost" copies of the pattern. This would be a problem with holography where the mirrored "twins" at higher orders will take up as much energy as the utilized off-axis patterns.

Although GPC allows fast SLM addressing, its one-to-one pixel mapping sets an upper limit to how intense the output beam could be. GPC output would typically be around 4 times more intense than the input level, corresponding to constructive interference of the foreground pattern with the synthetic reference wave [8].

[2] A binary modulator is one wherein only 2 levels can be encoded, typically zero and π for a phase SLM.

Unlike in digital holography, light from neighboring SLM pixels do not contribute into an integrated spot and there is no averaging effect that minimizes the effect of SLM imperfections. Higher intensities would be desirable for applications like active particle sorting or spot addressing which is holography's stronghold. This motivates the use of mGPC which effectively relays GPC output to a phase-only correlator.

2.5 Phase-only correlation of amplitude modulated input

Phase filtering can also be performed in amplitude-only modulated input light [46]. By using a 4*f* filtering setup, phase-only correlation, transforms input amplitude patterns into intense output spikes. A process similar to autocorrelation is used, but due to the phase-only constraints, instead of squaring, the absolute value of the Fourier diffraction pattern is obtained. This is done through a matched filter that applies a π phase shift ($e^{i\pi} = -1$) where the unfiltered Fourier distribution changes sign. For example, with disk shaped amplitude patterns, the Fourier transform follows an Airy distribution, hence the occurrence of near periodic concentric rings in the design of matched filters. Similar to image detection, the resulting output intensity spikes indicate locations of the correlation target patterns from the input scene. Hence, like GPC, there is also no need for heavy computations and it is only required to translate a copy of the correlation target pattern to similarly translate the output intensity. Despite the inefficiency of amplitude modulation in utilizing input light, the gathered light in the intensity spikes can be strong enough for applications such as optical sorting [47].

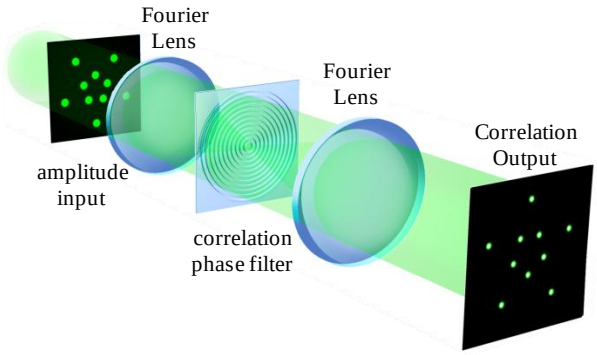

Figure 2.3. Setup for phase only optical correlation. The circular intensity patterns in the input are mapped into intense and narrow spikes using a phase only filtering process akin to optical autocorrelation.

2.6 Matched Filtering Generalized Phase Contrast

By borrowing features from phase-only correlation, matched filtering Generalized Phase Contrast (mGPC) combines the respective strongholds and advantages of GPC and holography. Similar to GPC, mGPC does not suffer from a strong un-diffracted zero-order light, ghost orders and spurious phase variations. Likewise, it is also straightforward to encode SLM phase patterns, only requiring translated copies of the same basis shape. Hence, due to their similar geometries, mGPC shares GPC's advantages over Fourier holography [16]. However, with the additional correlation part, mGPC also gathers light into strongly focused spikes. This focusing, of course, comes at the price of losing GPC's ability of forming contiguous extended areas of light. As in image detection, the correlation part also makes mGPC tolerant to input noise such as mild phase aberrations, hence, being able to work even with two consumer grade pico projectors used as phase SLMs [10]. Due to GPC's intensity gain which is roughly four times compared to a similar amplitude imaging setup [8], the output intensities from an mGPC setup are also higher when compared to a similar amplitude-input phase-only correlation setup. But since it effectively squeezes GPC's intensity output, the spikes would not be as high as what can be achieved via digital holography which can utilize more of an SLM's area for focusing into spots.

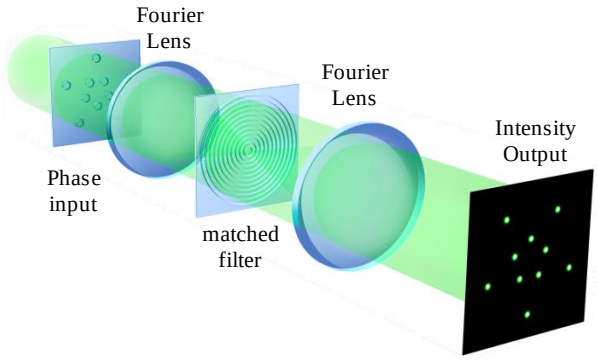

Figure 2.4. Setup for mGPC. Input circular phase patterns are mapped into intense output spikes by combining the operating principles of GPC and phase only correlation.

2.7 Numerical simulations

We compare the output intensities using the following parameters, peak intensity, integrated intensity within the full width half maximum (FWHM) and integrated intensity within the circle defining the input phase or amplitude pattern. Since the input intensity is unity, the output peak intensity is also a measure of the gain.

Due to their 4*f* geometries, the filter and output planes can be conveniently described with Fourier optics [48] and calculated with FFTs. A tophat illumination with a radius of 300 samples is zero padded to form an 8192x8192 array and get as much data points in the Fourier filter's central phase dot as memory would allow. The scaled first zero of the generated Airy function would be located at 0.61*8192/300 = 16.7 (see Appendix 2). The discretized central phase dot used has a radius of 7 data points which corresponds to a PCF central phase dot radius to Airy central lobe radius ratio of η = 0.42 while the surface reference wave has a central value of K = 0.5357 [8]. For all cases, a disk diameter of 50 data points was used.

The intensity profiles obtained for GPC, mGPC and phase-only correlation (abbreviated POC for brevity) are shown in Figures 2.5 and 2.6. The tophat input which also simulates direct imaging is also shown for reference.

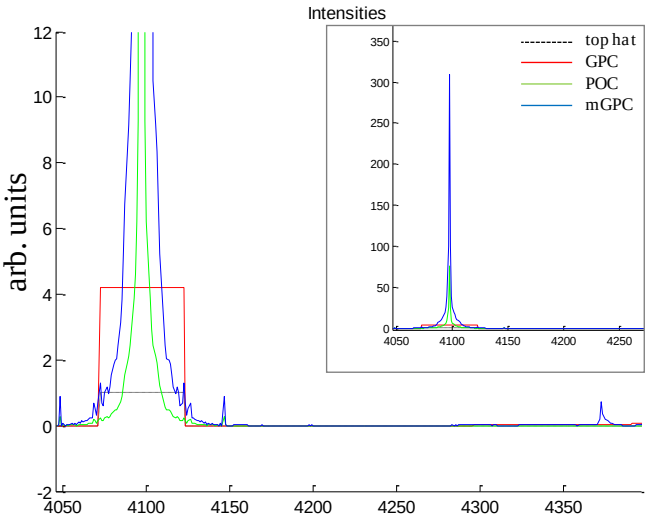

Figure 2.5. Intensity profiles for the input tophat, GPC, phase only correlatin and mGPC. Inset shows the same plot zoomed out to show the peak mGPC level.

Table 1. Comparison of output intensities

Beam shaping method	Center Intensity	Integrated intensity within:	
		FWHM	Encoded circle
GPC	4.2191	8.2650×10^3	8.2650×10^3
mGPC	309.19	0.3092×10^3	7.3786×10^3
POC	76.053	0.0761×10^3	1.7236×10^3

2.7.1 Practical considerations: finite apertures

In experiments, the finite extent of lenses or apertures effectively truncates the optical Fourier transform. Such truncation has a low pass effect that will blur sharp features (albeit with a usually high spatial frequency cutoff). Intensity wise, GPC, mGPC and phase only correlation are very similar at the Fourier plane. For phase only correlation, the only significant difference is on the DC region which is a result from its different input background. Hence, it would be the same high

frequencies that would be truncated for these beam shaping methods. Nonetheless, it is not apparent how these high frequencies contribute to the shape of the output. For example, high frequencies form the spike in mGPC while they define the imaged circle's edges in GPC. To assess tolerance to experimental shortcomings, we simulate the case of this experimental low pass. We use parameters similar to our experiments, i.e. a wavelength of 532nm going through an objective lens with NA of 0.4, and focal lengths of 300mm and 8.55mm for the first Fourier lens and objective lens respectively.

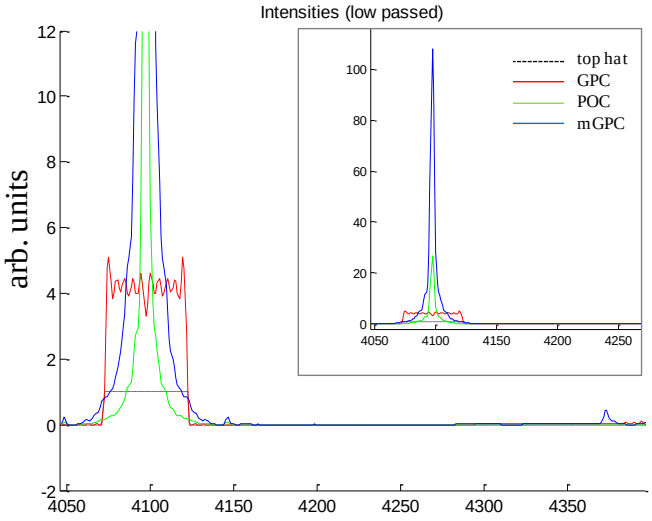

Figure 2.6. Intensity profiles for the input tophat, GPC, phase only correlatin and mGPC. An NA of 0.4 was considered by low pass filtering. Inset shows the same plot zoomed out to show the peak mGPC level.

Table 2. Comparison of output intensities with simulated low NA effect

Beam shaping method	Center Intensity	Integrated intensity within:	
		FWHM	Encoded circle
GPC	3.3209	7.9707×10^3	8.0342×10^3
mGPC	108.15	0.9992×10^3	7.2763×10^3
POC	26.617	0.2432×10^3	1.6994×10^3

The increase in the integrated intensity in the FWHM is due to the increase of integrated area as the peak intensity decreases. In the case of GPC, the peak intensity is no longer on the center due to ringing effects at the edge of the low passed circle. The maximum occurs at the edge of the circle with an intensity of 5.09.

2.7.2 Discussion

Although we have simplified experimental effects for the sake of generality, results show how mGPC and phase-only correlation would give higher peak intensities, albeit more localized compared to GPC's output. For cases with or without the NA truncation effect, mGPC's peak output is two orders of magnitude more intense compared to the input, while that of POC is one order of magnitude more intense. GPC, although having a lower peak, succeeds in delivering the most uniform amount of energy for a given area, giving a gain of around 4 compared to the input level resulting from its common path interferometry operation.

2.7.3 Comparing with focusing

A definitive comparison with a 2*f* holographic system cannot be done since its efficiency strongly depends on the device, i.e. how the zero, twin or ghost orders are dealt with and how the hologram calculation is optimized. Scaling of the output produced with 2*f* also depends on what experimental parameters are used, e.g. wavelength, focal length and SLM pixel dimensions when relating to FFT parameters. In any case, it is expected that, diffractive beam shaping approach would utilize much of the whole aperture, giving much higher integrated peaks. It is possible, however to compare some quantities by assuming a simple best case

scenario. Since only one on-axis trap is defined, there is no need to calculate the CGH and we just have a simple case of focusing the whole SLM area. Assuming a unit amplitude in each pixel then neglecting pixilation and experimental losses, the focused zero order, would have an amplitude of $\pi 300^2 = 2.83 \times 10^5$ or intensity of 7.99×10^{10}. This is many orders of magnitude much higher than what can be achieved via mGPC or phase correlation. The demagnified output from the simulated 4*f* setups would have 6.77μm radius. To get an Airy function whose first zero is located at 6.77μm, the SLM's circular region has to be focused with a lens of $f = 59.5$mm.

2.8 Summary

This chapter has presented an overview of several beam shaping techniques useful for biophotonics applications and compared their advantages. Holographic beam shaping can deliver intense 3D controllable focused spots but would be less ideal for patterns with extended area due with the introduction of spurious phase and amplitude. GPC, on the other hand, offers more freedom in addressing contiguous optical landscapes, making it useful for area addressing and for counter-propagating traps (Chapter 3), but lacks holography's focusing advantage. mGPC offers an interesting compromise by emulating a focusing effect on top of GPC hence being able to generate more intense output spikes like holography while maintaining GPC's advantages. Experimental work on mGPC would be studied in Chapter 4.

3 Counter-propagating optical traps

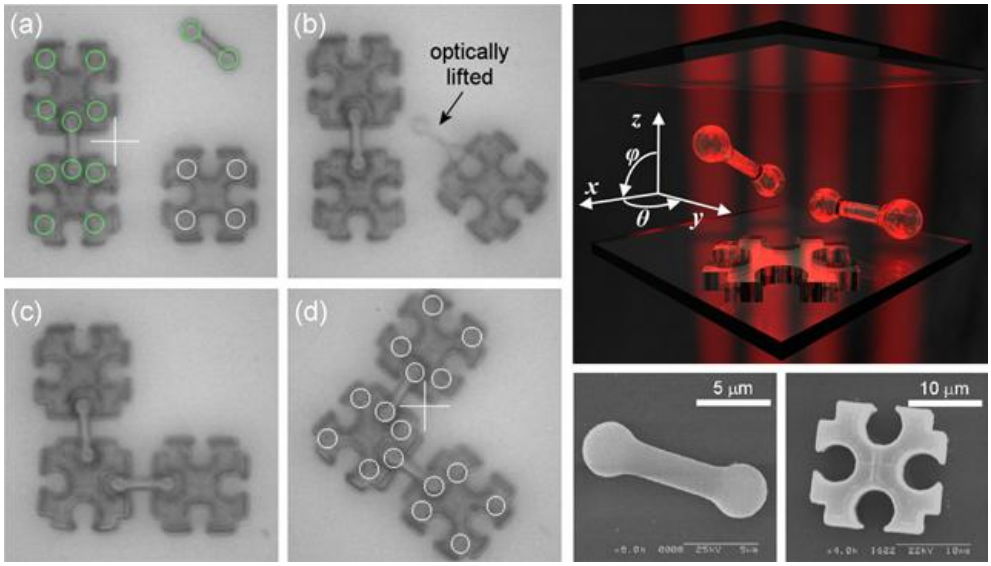

Figure 3.1. Counter propagating traps allow micromanipulation with a greater axial range. The greater volume of control, in turn, allows 3D 6-degree of freedom manipulation of complex micro structures. This allows novel experiments such as the micro assembly of interlocking puzzle pieces. (Figure adapted from [17]).

Light's ability to manipulate microscopic structures in three dimensions gives rise to new biological research applications. For example, microscopic scaffoldings that can be reassembled with multiple traps can simulate biological microenvironments (Fig. 3.1) [14]. With microfabrication processes such as two-photon polymerization, specially designed microscopic tools can be driven around biological samples for probing or sending stimulus. Similar to freely movable hand tools, 3D controllable micro-tools can be used to trigger biological, chemical or mechanical reactions in a localized and controlled manner. Given these diverse applications, extended three-dimensional optical manipulation becomes an important enabling tool. For an overview and for comparison, both optical trapping based on optical tweezers and counter-propagating beam traps would be discussed

in this chapter. Optical tweezers use high numerical apertures to form maneuverable gradient traps along the axial direction. Counter-propagating traps, on the other hand, use the scattering forces of opposing low NA beams for the particle's axial manipulation. Besides high NA optical tweezers and counter-propagating traps, alternative schemes of optical manipulation such as the use of Airy or Bessel beams [49], exploiting the particle's geometry [50,51] are also being explored.

3.1 Optical tweezers

As light refracts through a particle whose refractive index is higher than its surroundings, say a dielectric bead in aqueous medium, its momentum is changed, leading to forces that move the bead towards high intensity regions [52]. This is depicted in Fig. 3.2, wherein, two rays are shown, deflected as they go through a bead. The force resulting from the more intense ray (drawn thicker) would dominate and, due to momentum conservation, move it towards the more intense part of the beam. Optical tweezers, thus rely on the 3D localized light intensity gradients resulting from high NA focusing (typically NA > 1). The focusing geometry also integrates a large amount of light into a small area which consequently scales up the gradient forces. The advent of real time computer programmable spatial light modulators enables a plurality of reconfigurable holographic traps that allow the user to choreograph complex trajectories of micro particles [53,54]. Particle motion is achieved by directly moving the high intensity region.

Optical tweezers can be implemented dynamically with simple scanning mirrors that could be time sharing a single trap over multiple particles [55,56], acousto optic modulators [57], or, as an application of digital holography, with SLMs via (HOTs) [18,53,54]. SLM based beam shaping could offer more versatility for trapping by shaping beams having different properties and even correcting aberrations in the optical setup [58]. Actuation used to be relatively slow due to CGH calculation (~10Hz), however, readily available low cost parallel computing using GPUs together with optimized algorithms [59] now allow real time control of holography based optical tweezers.

Due to the use of high NAs, however, there are limitations or disadvantages when using optical tweezers. The range of motion would be limited by lens aberrations [35] and the beam's general divergence. As the sample has to be close to the (immersion) objective, there would be little room for additional equipment. Moreover, when using higher powers for applications demanding fast response, the tight foci within the trapped object could initiate unwanted radiation overdose on live organisms. With the advent of micro/nanostructure fabrication facilities, such as two-photon photopolymerization, a less constrained optical trapping system is desirable for maneuvering micro/nanostructures [23–25] and advancing their use in fields of micro-robotics, micro-assembly, nano-surgery etc. Hence, there is a need to explore different beam shaping geometries and micromanipulation schemes.

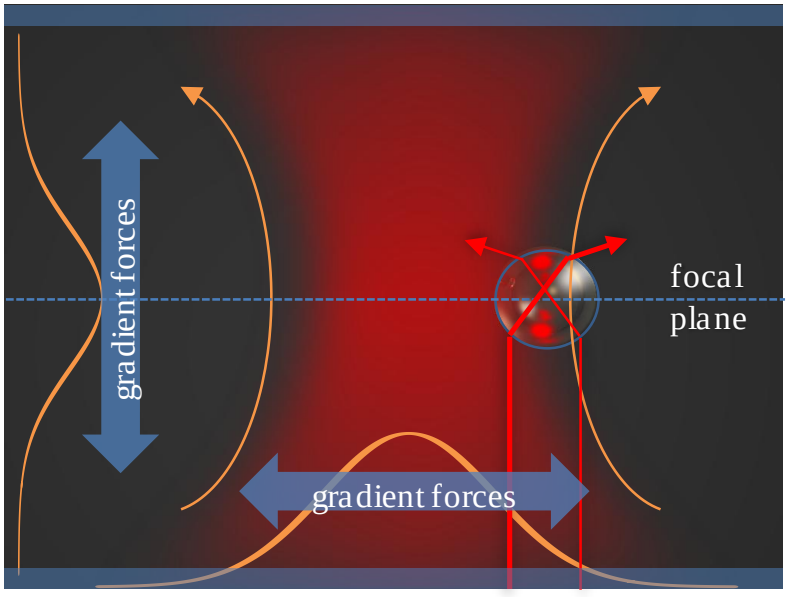

Figure 3.2. Operating principle of optical tweezers. Gradient forces result from the refraction of light that effectively attracts the particle towards the region of highest intensity, i.e. towards the focus.

3.2 Extended optical manipulation with Counter-propagating taps

Although optical tweezers are commonly used for optical trapping, there are many applications wherein larger fields of view, manipulation area, as well as trapped objects, would be desirable but prevented by the use of high NA geometries. While optical tweezers can displace objects up to 50μm laterally and 40μm axially [35], larger objects such as motile organisms [13] or microtools [25] which are around ~20-50μm would appear to be constrained within such manipulation volume. To benefit from optical trapping at these larger ranges, it is therefore needed break free from high NA geometries. Unfortunately, using lower NAs also means losing axially confined light distributions, and thus losing strong axial gradient forces. At low NAs, scattering forces dominate and tend to push objects along the direction of light propagation. Hence, to control the axial positioning of such objects, instead of pushing them indefinitely towards a single direction, beams from opposing directions are directed towards the object. Such arrangement is thus known as a counter-propagating (CP) beam geometry. Using the CP geometry, trapping volumes of 2x1x2mm^3 have been reported at NA=0.25 [13]. In our workstation (NA=0.55), this volume is bounded by the 250μm sample cuvette along the axial direction and the 4*f* scaled SLM input profile which is roughly ~100x100μm^2.

3.2.1 Implementing counter-propagating optical traps

The operation of CP traps is illustrated in Fig. 3.3. Two beams are directed towards the top and the bottom of a particle. The particle's height is then controlled by the relative intensities of these beams. Scattering forces whose action is to push the particle along the beam direction enable extended axial manipulation. Like optical tweezers CP traps also use gradient forces to translate particles along transverse directions. Although, not as strong as the ones delivered through high NA objectives, demonstrations on horizontally oriented setups have shown that gradient forces are strong enough to support 10μm polystyrene beads against gravity using 11.6mW of trapping laser power [15,60].

Besides the use of a 4*f* geometry as in the BWS, other means of implementing CP traps include using optical fibers [61], using the diverging region in a laser focusing setup [15], low NA holography [62–64] and even optical phase

conjugation [65]. To give a general overview and a rough comparison with our implementation, we will also discuss examples of these alternatives.

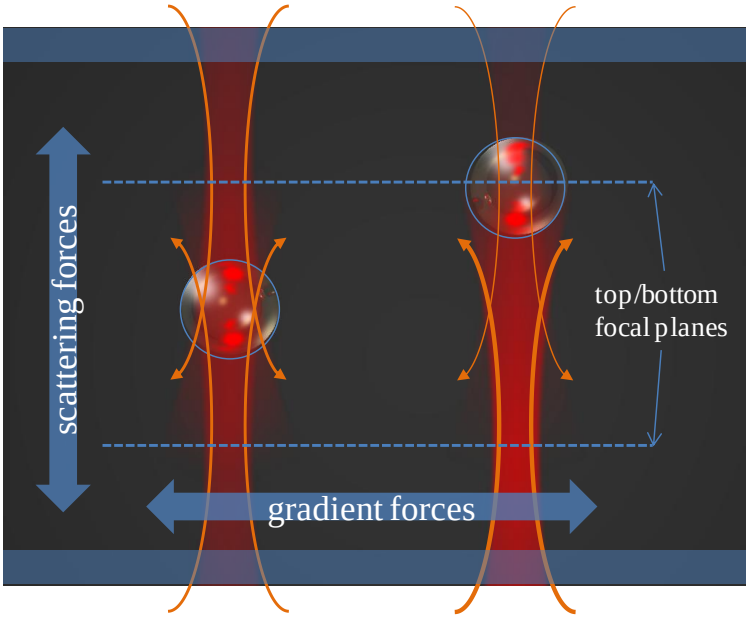

Figure 3.3. Operating principle of CP traps. Beams from opposite directions (e.g. top and bottom) push the particle via scattering forces. The balancing of the intensities of these beams determine the particles axial position. Similar to optical tweezers, gradient forces are used to control the particle's transverse position.

3.2.1.1 **Ashkin's potential wells**

With many trapping experiments in the past based on optical tweezers, it may be interesting to note that a low NA CP trapping geometry is also demonstrated by Ashkin in the 1970s [15]. Ashkin suggested constructing an optical potential well or "optical bottle" using two opposing weakly focused Gaussian beams with the waists (focal planes) separated (Fig. 3.4). A dielectric sphere will be in stable equilibrium at the point of symmetry of such system, as also shown through optical force calculations [66]. When one beam is off, 2.68μm spheres in water can move upto ~220μm/sec when pushed by a 128mW beam as shown in [15].

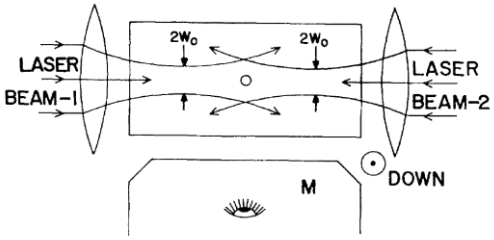

Figure 3.4. An illustration of the counter propagating trapping setup used by Ashkin [15]. Opposing laser beams are focused with low numerical aperture lenses. The trapped object is located at the middle of the separated focal planes. (Figure adapted from [15]).

3.2.1.2 **Fiber and waveguide delivered CP traps**

Optical fibers have also been used to deliver CP traps due to their flexibility and the already microscopic scale of their cores [61]. They have been used for rotating cells while they are being observed through a microscope, thus obtaining a 360° view (Fig. 3.5) [60]. Similarly, waveguides integrated to the sample chamber via custom fabricated microfluidic chips have been done [67]. The integrated optics approach has the advantage of being alignment free, and was used for trapping or stretching red blood cells. The direct use of fibers or waveguides, however, removes maneuverability in the transverse directions, hence their use in rather specialized applications.

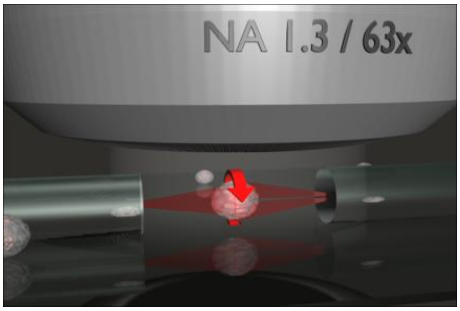

Figure 3.5. CP traps can be delivered directly from optical fibers. Optical fiber and waveguide optics can be convenient for special applications not requiring transverse control such as cell rotation or stretching. (Figure adapted from [68]).

3.2.1.3 **Holographic twin traps using a mirror**

The clever use of reflection to generate an opposing beam has been also explored [62–64]. A low NA holographic setup is used to simulate a pair of two axially

displaced beams (Fig. 3.6). This displacement is achieved by using a lens-like phase distribution. Upon reflection from a mirror, the simulated advanced beam acts as an opposing beam with respect to the delayed beam. As with holography based approaches, the required phase distributions gets more complex when multiple traps and different axial displacements are required. These lens like phase requirement also prevent the alternative use of low cost binary SLMs.

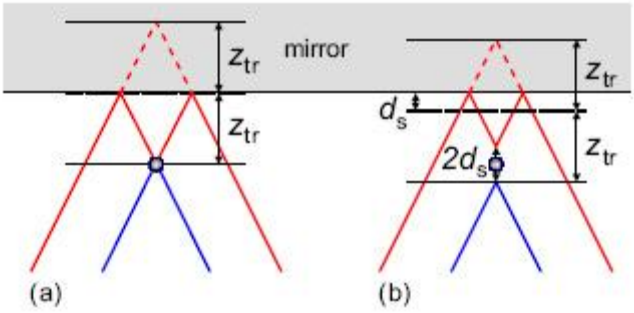

Figure 3.6. Instead of using separate beam sources, holographic twin traps simulate axially displaced beams. The advanced beam (red) act as the opposing beam upon reflection from a mirror.(Figure adapted from [62]).

3.3 CP traps in the Biophotonics workstation

We use a counter-propagating beam geometry to manipulate over larger volumes through our BioPhotonics Workstation (BWS) [26]. Since the BWS constructs CP beams through low-NA objectives it affords a large working distance, sets less stringent constraints on the sample chamber, and can trap particles without sharp focusing. Furthermore, the use of a 4*f* imaging or filtering configuration in the BWS lessens the computing requirements, which in turn, simplifies the implementation of real time interactive control.

In our BWS the traps are delivered through two opposing objectives that relay an image of the trap onto the sample chamber. The BWS uses an imaging setup to take advantage of fast beam shaping techniques based on a 4*f* geometry such as GPC. The weakly focusing lasers in Ashkin's setup can be compared with the BWS's use of the weak Fresnel-like focusing from a disk or tophat distribution. Treating the circle as a single zone Fresnel-zone plate, the propagated light would

be most intense at a distance of nR^2/λ away from the disk, where n is the refractive index of the surrounding medium, R is the disk radius and λ is the wavelength. A simulation of such propagation which also shows the relative locations of the imaged disks and trapped bead is shown in Fig 3.7. The CP setup oconsists of disks with 3μm radii located at two image planes (IP1 and IP2), separated by a distance of S = 30μm. A vacuum wavelength of 830nm and an aqueous medium with a refractive index of 1.33 is used in the simulation.

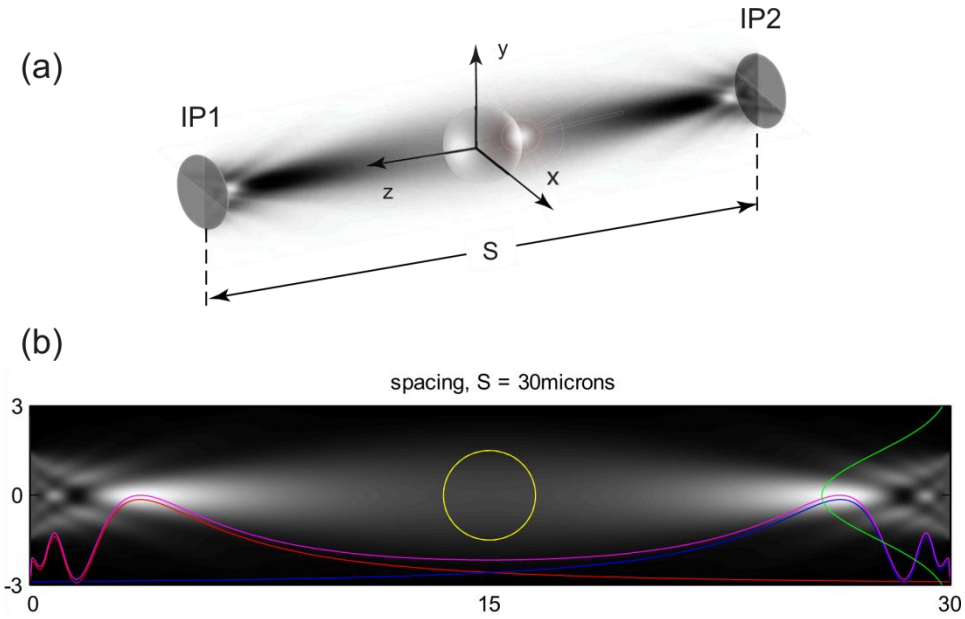

Figure 3.7. Optical trapping with counter-propagating shaped beams. (a) 3D view of counter-propagating disk-shaped beams projected through opposite microscope objectives onto image planes, IP1 and IP2, separated by distance, S, to create a stable optical trap between the image planes. (b) Axial slice through the simulated volume intensity between two 3micron diameter light discs; overlays show the expected stable trapping position for a microsphere, together with plots of intensity linescans (red: axial intensity of right-directed beam; blue: axial intensity of the left-directed beam; magenta: total axial intensity; green: transverse intensity linescan halfway between the discs). (Figure adapted from [69])

3.3.1 Tradeoffs of the BWS

Compared to high NA optical tweezers the axially extended counter-propagating optical traps delivered through the BWS allow 3D repositioning of particles over a larger working volume. Software is much easier to implement since trap patterns are drawn directly into the SLM instead of holograms that have to be solved. These

trap patterns, in turn, are directly mapped as output intensity within an addressable light shaping module. The added axial degree of freedom has allowed experiments like flipping of planar microstructures and lifting puzzle pieces of reconfigurable microenvironments [14]. Furthermore, the use of low NA objectives which also have long working distances allows more freedom on the sample containers (Fig. 3.8(b)). This allows room for a variety of auxiliary applications such as advanced micro-spectroscopic [26] or multi-photon characterization methods or pH mapping of heat stressed cells through fluorescence ratio imaging [70]. This has also allowed direct side view imaging, making three dimensional experiments more intuitive (Fig. 3.8(a)) or allowing CARS (coherent anti-Stokes Raman) and fluorescence spectroscopy independent from the trapping optics [26].

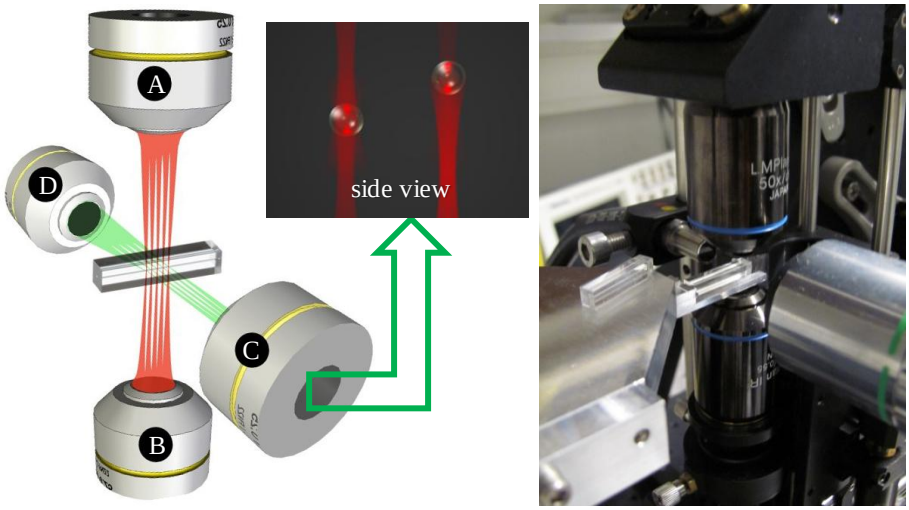

Figure 3.8. Opposing objective lenses for delivering CP traps (A and B) and for side view imaging and characterization (C and D) and an actual photographs of the BWS (one objective is replaced by a fiber light source).

Because of the use of two opposing objectives, the BWS requires a stricter alignment protocol for the two opposing beam to coincide along their paths. Studies on how to systematically align the BWS with the aid of software and image processing have been presented [71,72]. Furthermore, our CP setup would require an extra beam channel, therefore, an extra objective lens also. The typically higher cost of high NA objectives, however, sets a tradeoff in a single high NA objective tweezer setup and eliminates the need for a mirror in the sample chamber as in the

twin trap approach. With a system of adjustable mirrors to facilitate CP beam alignment, two imaging channels and a side view accessories, the BWS setup can be relatively complex.

3.4 Instability of CP geometries

The advantage of having a larger manipulation volume comes at a price of having less intense light, which is less stable in holding particles in place. Due to weaker focusing there are relatively lower transverse gradient forces as compared to optical tweezers which can also cause particles to drift away. Moreover, excess light that goes beyond the particle's area wastes energy and can even interfere with neighboring traps. This waste is minimized when the foci overlap as in Fig. 3.9(b). This improves transverse stiffness and creates a very strong trap, even for highly scattering objects, using high-NA [73], but can become unstable when minimizing intensity hotspots using lower NA. It also needs axial focal shifting for axial manipulation. The converging beams in Fig. 3.9(c) also create unstable traps [74], although it can be stabilized by alternating it with Fig. 3.9(a) [75]. The tube-like beams in Fig. 3.9(d) maintains optimal transverse gradients over very long operating distances but is generally unstable since the axial forces cancel, though subwavelength particles may be trapped and transported over hundreds of microns using standing wave gradients [49].

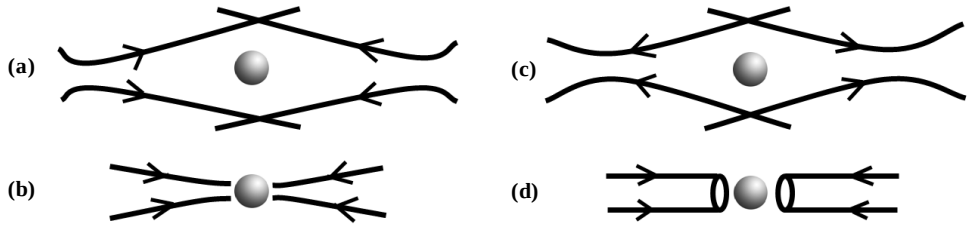

Figure 3.9. (a) Conventional stable CP-trapping in the far-field of diverging beams. (b) Overlapping foci. (c) Converging beams with foci oppositely positioned compared to (a). (d) CP-trapping with tube-like beams. (Figure adapted from [76]).

3.5 Improving stability of CP traps

Given the strengths of a counter-propagating geometry, how can one work around some of its weaknesses? For example, the stability and stiffness of the CP geometry is sensitive to the foci separation [66,74] since it needs a proper axial

variation of the opposing axial forces that, in turn, depends largely on the wave propagation. Since low NA CP beams lack the strong advantages of optical tweezers like strong gradient forces, we propose several solutions for improving the stability of CP trapping:

1. Identify alternative geometries where trapping can be stable while maintaining the same beam shaping approach
2. Use a software based dynamic position stabilization through a feedback loop in the experiment
3. Explore optical distributions that can deliver higher intensity gradients by using alternate beam shaping methods.

The first approach has been pursued in theoretical works involving force calculations for trapping with the CP geometry [66,69]. Experimental force characterizations are also presented in [77]. The trapping stiffness on the particle on different positions is mapped out. From the numerical results, alternate regions of stable trapping were subsequently identified. This strategy, however, would require reworking the existing BWS setup, and would therefore take time to implement experimentally.

Without modifying existing BWS setups, a software based approach that implements dynamic axial stabilization [76] offers a quick fix. Computer vision tracks axial positions of multiple particles for use in a feedback algorithm that correctively adjusts the respective counter-propagating beam pair intensities as needed. The particles can then be moved-to or held in user defined axial positions, without constant user intervention.

The third approach requires synthesizing light fields that have desirable propagation properties as done in [78]. We have also explored the use of mGPC which demonstrates stronger focusing. It also presents an attractive alternative due to its similarity to GPC used in existing BWS setups. The mGPC method provides high intensity spikes with fast beam shaping and can even work with consumer grade projectors. Our work on mGPC is still being actively pursued and optimized for other applications such as cell sorting. Nevertheless, initial progress with mGPC will be covered in Chapter 4.

3.6 Stabilizing CP traps using machine vision based feedback in the BWS

In order to axially extend the active trapping region, we implemented a dynamic axial stabilization of the trapped particles by tracking and correcting their positions using machine vision. The counter-propagating beam traps are adjusted to correct the trajectory of particles after analyzing the video stream from the side view imaging system [26].

3.6.1 Experiments in the BWS

Experiments were done in our BioPhotonics Workstation. A schematic showing the different modules of the BWS as well as an actual photograph is shown in Fig. 3.10. The BWS uses two independently addressable regions of a spatial beam modulating module that are optically mapped and relayed as a plurality of reconfigurable counter-propagating beams in the sample. The scaling between the spatially light modulating pixels and the sample plane are defined by the focal lengths of the relaying lenses. The user can independently control the number, size, shape, intensity and spatial position of each CP-beam trap through a LabVIEW interface.

3.6.1.1 **Sample preparation**

The wide working space between the barrels of two objective lenses (Olympus LMPL 50×IR (WD = 6.0 mm, NA = 0.55) easily accommodates a 4.2 mm thick sample chamber (Hellma, 250μm × 250μm inner cross-section, 1.6μL volume). Polystyrene beads (5 μm and 10 μm diameters) are loaded into the Hellma cells. These cytometry cells have optically flat surfaces that are suitable for trapping and imaging.

3.6.1.2 **Side view imaging**

A side-view microscope monitors the axial positions of the trapped particles. This unique observation mode, usually unavailable in optical tweezing, is used to provide real-time position feedback for active stabilization. Images from the side-view video microscope are streamed to a computer for particle tracking and analysis. The feedback software and multi-particle tracking algorithms are developed in LabVIEW using NI Vision image and video processing libraries.

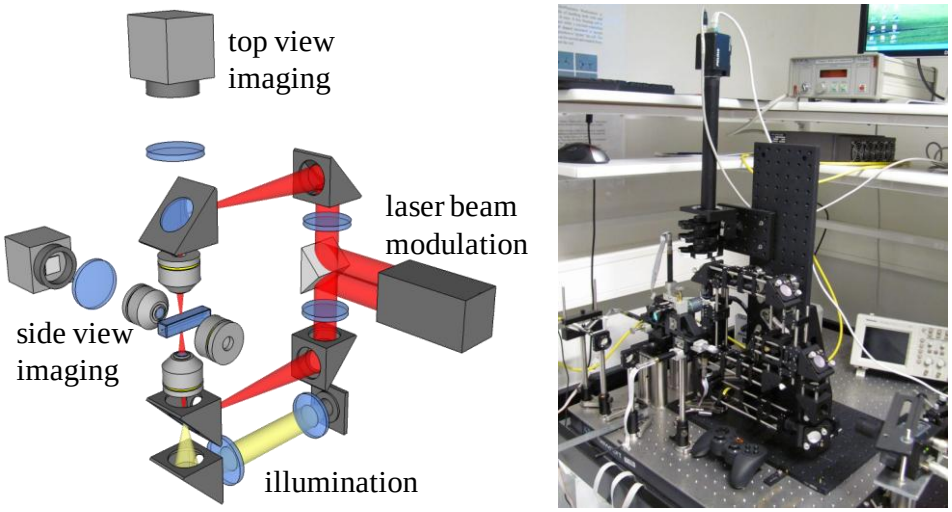

Figure 3.10. Simplified schematic of the BWS showing its different modules and an actual BWS setup used for our experiments.

3.6.2 Stabilization feedback loop

The software-hardware feedback loop for stabilizing particle positions is depicted in Fig. 3.11. The following procedure describes the real-time feedback approach for stabilizing a counter-propagating trap confined along a user-defined transverse position (X,Y):

1. The user specifies the desired axial position, Z_d, for a particle.

2. From the side-view, computer-vision determines the actual particle position, Z_m, and its error, $\varepsilon = Z_m - Z_d$.

3. The software compares the error, ε, with two thresholds, ε_{max} and ε_{min}, and sets the respective intensity control signals, $I_{\uparrow}$ and $I_{\downarrow}$, for the upward and downward beams:

    a. $|\varepsilon| > \varepsilon_{max}$: Set the beam pushing toward Z_d to maximum, I_{max}, and turn off the opposing beam for laser-catapulting the particle towards the desired position.

b. $\varepsilon_{min} < |\varepsilon| < \varepsilon_{max}$: Set the correct beam at I_{max} and the opposite beam to $I_{max} - \Delta I$.

c. $|\varepsilon| < \varepsilon_{min}$: Maintain the beam intensities.

Thus, we have a simple tri-state controller where the intensity control signal can be either zero, $I_{max} - \Delta I$, or I_{max}. These steps are looped for active stabilization and error suppression. For multiple particles, a tracking system ensures correct addressing of respective axial positions while the feedback loop is simultaneously executed for each particle. A tracking algorithm assigns an ID to link the same particle identified though successive video frames.

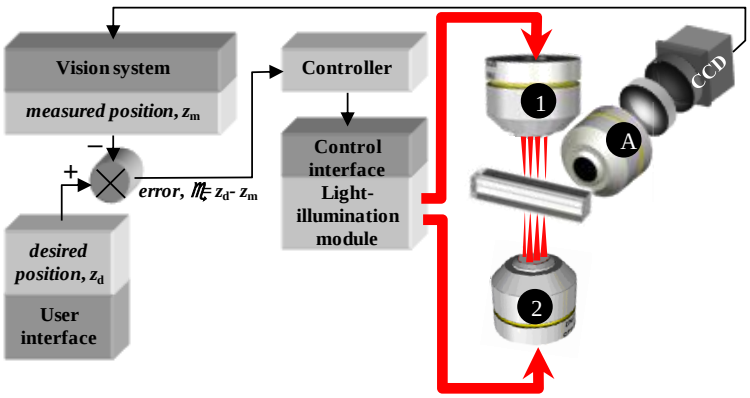

Figure 3.11. Active trap stabilization on the BioPhotonics Workstation using vision feedback. An array of actively regulated traps are relayed through well-separated objectives (1 and 2) that provides ample space for side-view microscopy (objective lens A, zoom lens and CCD camera). Computer vision provides real-time position feedback for regulating the traps. (Figure adapted from [76]).

3.6.3 Results

We perform trapping experiments wherein 10μm beads are set into user defined positions. The simplest case shows a single bead initially lying at the bottom of the chamber far from the user specified position (blue rectangle in Fig. 3.12(a)). The bead was eventually moved-to and held in the desired place via feedback algorithm (Fig. 3.12(b)).

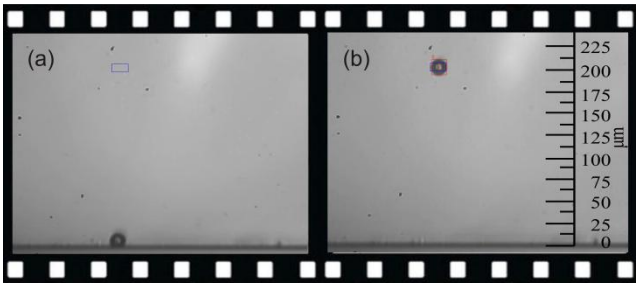

Figure 3.12. Snapshots from side-view microscopy of optical manipulation and trapping of a 10µm diameter particle using an actively stabilized counterpropagating-beam trap. The blue rectangle overlay is centered on the desired position. A red square circumscribes the auto-detected particle.

Multiple stable traps are also demonstrated using 10µm beads, initially forming a "W" pattern (Fig. 3.13(a)), then an inverted "V" pattern (Fig. 3.13(b)). This ability to set independent particle heights can be used to rotate complex structures such as microtools.

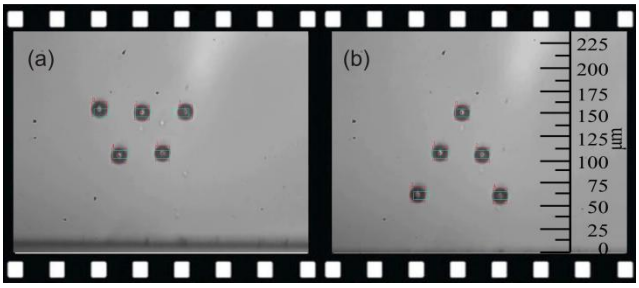

Figure 3.13. Side-view microscopy showing simultaneous optical trapping and manipulation of multiple 10 µm diameter particles into various configurations using actively stabilized counter-propagating traps.

The stabilization is not limited to particles with the same size since the feedback system will constantly correct position deviations even for suboptimal trapping geometries. A combination of 5µm and 10µm for example can be set to independent stable positions (Fig. 3.14).

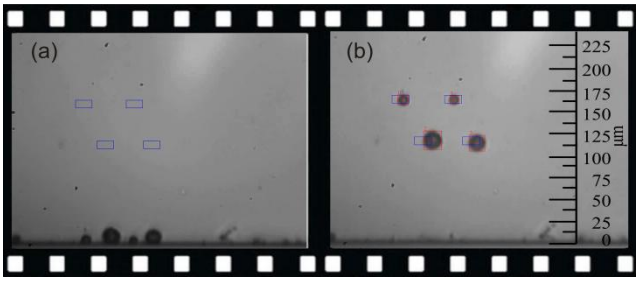

Figure 3.14. Snapshots from side-view video microscopy of simultaneous optical manipulation and trapping of differently sized particles (5µm and 10µm diameter). Particles are rapidly trapped and stabilized via side-view feedback with static foci separations

3.7 Advantages of software based dynamic stabilization

Applying software based dynamic stabilization to otherwise unstable CP-geometries, allow them to be used in a highly controlled way. This gives freedom in choosing CP-trap geometries (Fig. 3.9) based on experimental constraints or requirements. For example, to minimize hotspots on living cells using geometries in Figs. 3.9(a), (c) may be used. To optimize transverse forces, geometries in Figs. 3.9(b), (d) can also be used. As shown Fig. 3.14, this also avoids having to adjust the focal separation between the opposing beams for different particle sizes, as required in static CP-beams [66]. Since our approach is purely software-based it can be easily adapted for a variety of trapping configurations. A software approach also easily benefits in improvements in computing hardware and image processing algorithms. For example, more recent works based in digital holography by other groups have achieved feedback loops of ~10ms for position clamping [64], or ~4ms [42] by using GPUs, high speed cameras and advanced SLM addressing.

3.8 Conclusion

We have presented the counter-propagating beam trapping scheme which inherits advantages of 4*f* beam shaping methods like GPC or mGPC over digital holography commonly used for optical tweezers. Furthermore, the CP geometry offers advantages specific to micromanipulation such as extended axial manipulation and fast beam reconfiguration useful for position stabilization. Hence, to overcome the tradeoffs of having less light in far field trapping regions, software based position stabilization of trapped particles was implemented. A robust 3D optical micromanipulation system such as the BWS therefore allows

novel experiments and simultaneous characterizations through side view extensions made possible by the extended working distance in low NA geometries.

4 Matched filtering Generalized Phase Contrast

In Chapter 2, we briefly introduced and compared several beam shaping methods that can be used for biophotonics applications. Chapter 3 discussed the use of counter-propagating traps in the BWS and offered suggestions for improvements, including software based stabilization and using alternate beam shaping methods. This chapter would now focus on an alternate beam shaping method, the matched filtering Generalized Phase Contrast method (mGPC) (Fig. 4.1). The theory behind mGPC and its experimental demonstration on low cost pocket projectors would also be presented.

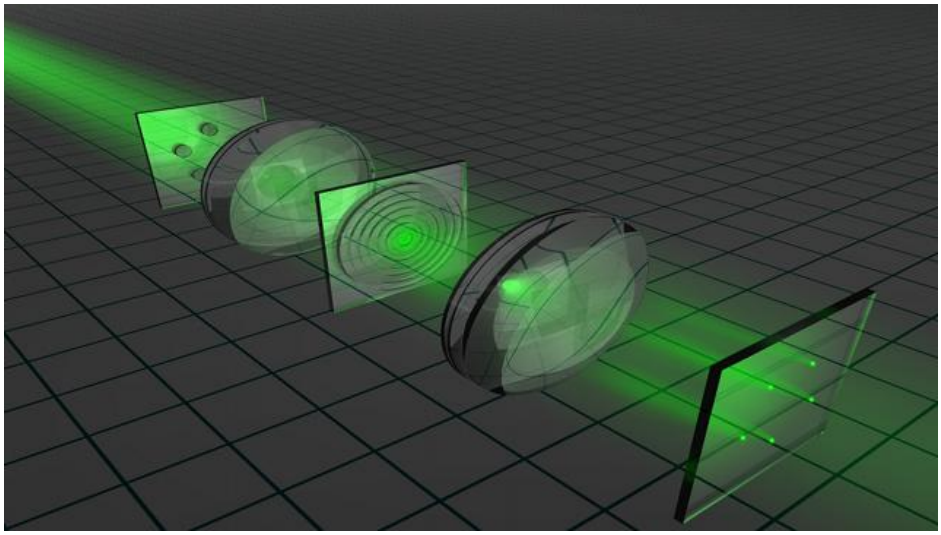

Figure 4.1. Artist rendition of mGPC in action. Circular phase profiles at the input are mapped into intensity spikes at the output by using a matched filter at the Fourier plane.

4.1 Combining GPC and phase-only optical correlation

The mGPC method can be thought of as a hybrid of GPC and optical phase-only correlation, which, in turn, can be treated as a special case of digital holography. Both advantages of GPC and holography, are therefore available in mGPC. Similar to GPC, mGPC does not suffer from speckles or a strong zero order, and mGPC

also requires minimal computational resources. On the other hand, mGPC's light integrating feature which is similar to focusing in holography allows it to operate on much cheaper spatial light modulators, i.e. consumer projectors based on liquid crystal on silicon (LCoS). Non uniformities in the phase of such low cost devices are "averaged out" when large regions of light are integrated into smaller spikes. With its fast implementation, well defined propagation behavior and ability to operate with low end hardware, mGPC offers a robust and low cost beam shaping [79] that can be used for biophotonics as well as other applications.

To illustrate how mGPC works it is helpful to treat the GPC and the phase correlation parts separately. Starting with a direct representation of a desired correlation target pattern, such as a disk, drawn on a phase SLM, GPC efficiently performs a direct phase-to-intensity mapping via common path interferometry [8]. This is implemented through a 4*f* Fourier filtering setup, as shown in Fig. 4.2(a), wherein the lower frequency components at the Fourier plane are phase-shifted to form a synthetic reference wave (SRW) that interferes destructively with the pattern's background and constructively with the foreground. The size of the GPC central phase shifting dot in the Fourier domain can be optimized for contrast based on the size and shape of the SLM aperture, the input beam, or whether uniform or Gaussian illumination is used [8,80].

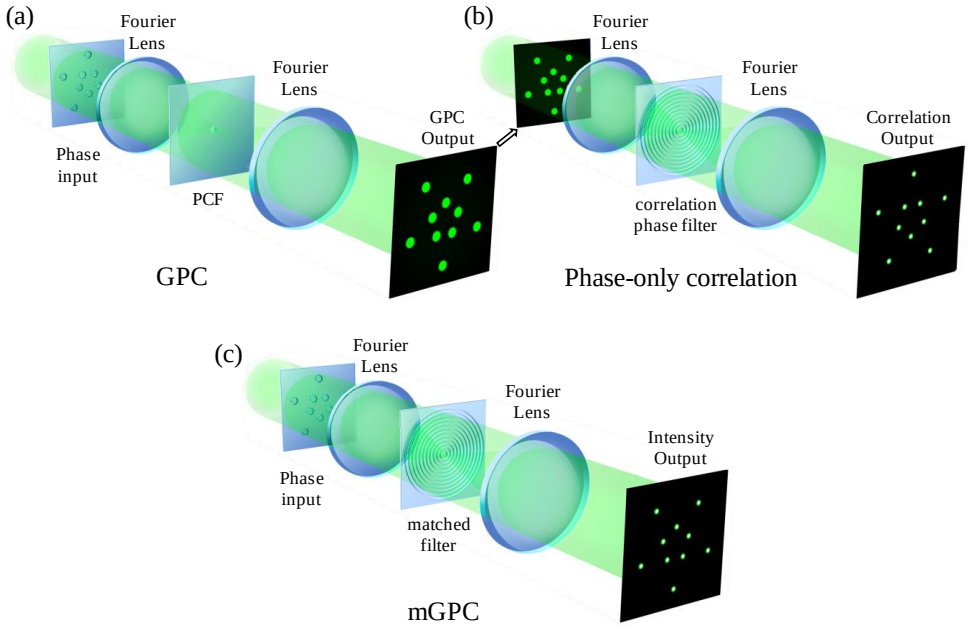

Figure 4.2. GPC (a) and phase-only correlation (b) setups, which, when combined in tandem, form an mGPC setup, (c). Since the phase contrast filter of GPC is effectively 4*f* imaged onto the phase correlation filter, they can be combined into a single phase filter. The resulting mGPC setup, (c), maps phase disks at the input into narrow intensity spots at the output. (Figure based on [11]).

4.1.1 GPC Optimization

In proof of principle experiments, it is convenient to use a tophat illumination for the SLM since it can be tuned with an adjustable aperture or iris which is much simpler than changing the magnification of a Gaussian beam that otherwise requires swapping and repositioning lenses. Output from most lasers, typically having a Gaussian profile, can be expanded large enough to have a near uniform central region which then goes through an adjustable circular iris. This adjustable source, which illuminates the 4*f* setup, then serves as the starting point for GPC optimization.

GPC's image formation is based on the interference of a low passed and high passed input light wherein the "hard" cutoff is determined by the PCF radius. Light going through the PCF central phase dot forms the low passed reference wave, i.e. the synthetic reference wave, synthesized from the same signal carrying input light.

For optimal contrast this SRW should be at about the same amplitude with the light contribution that defines the phase patterns to be imaged. If tophat illumination on an SLM produces an Airy with central lobe radius (first zero) R_{Airy} at the Fourier plane, an optimal radius of the PCF, R_{PCF}, can be obtained through the dimensionless parameter, η, which governs the resulting SRW [8]. The optimal choice of η, in turn, depends on the input phase distribution, i.e. the fill factor of the phase shifted patterns at the input to be mapped as foreground intensities at the output. In typical optical manipulation setups, the fill factor of these phase patterns would be around 25%, for which η = 0.627 gives an optimal contrast at the output [8].

$$\eta = \frac{R_{PCF}}{R_{Airy}} = 0.627 \tag{4.1}$$

To compensate for experimental deviations, darkness should be observed when no phase patterns are encoded, while adjusting the radius of the light going to the SLM. Although this optimization is for GPC, this darkness condition is still applicable to mGPC as the Fourier transformed input will be concentrated on the center away from the concentric rings of mGPC's matched filter. With the background removed via GPC, the next step in mGPC is to perform optical phase correlation using a phase-only filter to process the GPC-generated light distributions (Fig. 4.2(b)).

4.1.2 Phase-only optical correlation

Correlation is a known technique for looking for patterns in an input scene. Common digital image processing applications include simple implementations[3] of optical character recognition or face detection. In the correlation process a target pattern is convolved with an input image to detect regions that are similar to the target. In the Fourier domain this is equivalent to point-wise multiplying the Fourier transforms of the target pattern and input image. If the target and input are identical, the process becomes autocorrelation, and point-wise multiplication effectively becomes squaring.

[3] Software or firmware would commonly use image processing algorithms other than correlation nonetheless.

Although the squaring of the Fourier transform cannot be done with phase only optics, taking its absolute value has a similar effect. Since both squaring and taking the absolute changes the distribution to have all values positive, the flattening effect in the phase would be similar. Since the phase has a dominant effect in the resulting Fourier or inverse transform, as commonly exploited in holography, a phase only correlation would still work to detect similarities in the input image.

As an illustrative example, if an input disk is cross-sectioned and represented as a tophat distribution, i.e. Fig. 4.3(a), its corresponding Airy function distribution, i.e. Fig. 4.3(b), is rectified to emulate the superposed "squaring" at the Fourier plane, i.e. Fig. 4.3(c), which is required for the phase-only correlation process [8]. This can also be seen as enforcing a planar phase to the Airy function, a process akin to simpler cases in digital holography. Thus, for an input light pattern consisting of an array of top-hats, the final result consists of intense spikes corresponding to the location of each of the phase-only correlated tophats.

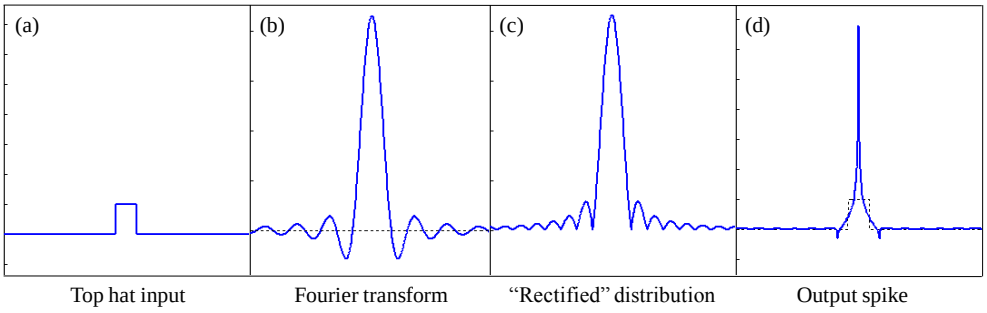

Figure. 4.3. The correlation part of mGPC works by applying phase shifts that will rectify the Fourier transform (b) of an input tophat amplitude (a). As the rectified Fourier transform (c) possesses a plane wave-like phase, a Fourier lens will focus it into a strong spike (d). (Figure adapted from [11]).

Although the GPC and the matched filtering steps are theoretically perceived as a relay of two 4*f* filtering setups, in practice this 8*f* setup can be conveniently squashed into a compact 4*f* setup (Fig. 4.2(c)) as the GPC filter plane is imaged onto the matched filter plane. Therefore, the resulting phase filter will consist of the GPC central phase dot superimposed on the rectifying concentric phase rings that follow the Airy function's zero-crossings as seen in Fig. 4.3(b) or Fig 4.4.

4.1.3 Binary matched filters

By restricting the correlation target pattern's (cTP) symmetry to being either even or odd, as in circular phase patterns, the Fourier transform can be purely real or purely imaginary. This then means that the function only has two relative phase values, 0 or π. This corresponds to changes in sign, i.e.

$$e^{i0} = 1, \qquad e^{i\pi} = -1. \tag{4.2}$$

Adopting a simple Fourier optics approach, a matched phase-only filter transfer function having the phase, $\phi(x, y)$, can be immediately obtained by

$$e^{i\phi(x,y)} = \operatorname{sgn}\left(F\{u_{ctp}(x, y)\}\right) \tag{4.3}$$

Where u_{ctp} defines the input field with the correlation target pattern at the optical axis, F is the Fourier transform operator and sgn is the sign function. This filter phase distribution effectively "rectifies" the Fourier distribution, giving it a planar phase and hence focusing to a sharp spike at the output. The superposition and shift properties of the Fourier transform extend this principle to the case of multiple cTPs, enabling dynamic control of a plurality of simultaneous high intensity spots.

4.1.4 Matched filter for circular correlation target patterns

Circular phase patterns are convenient to program and have a well known Fourier transform. Light having uniform amplitude with a binary tophat phase distribution produces a focus that is similar to an Airy function in addition to the zero-order resulting from the input background. Hence, a matched phase filter should contain concentric circles with binary phase alternating between 0 and π and a central π-phase disk corresponding to the zero-order. Setting aside the GPC part, Figure 4.4 shows how the Airy function is used to design matched filters. If the matched filter is drawn on a pixilated SLM, as we have implemented through GUI programs, the zeroes of the Airy function can be approximated[4] by a shifted sine, function. The shift is equivalent central lobe's radius. An SLM's pixilation would typically introduce a greater error than this approximation, but we still obtain good experimental results nonetheless.

[4] This approximation gave results that deviate to less than 1% as we later found out by numerically searching the zeroes of the Airy function using a simple adaptive-resolution bisection method (precision of ~10^{-12}).

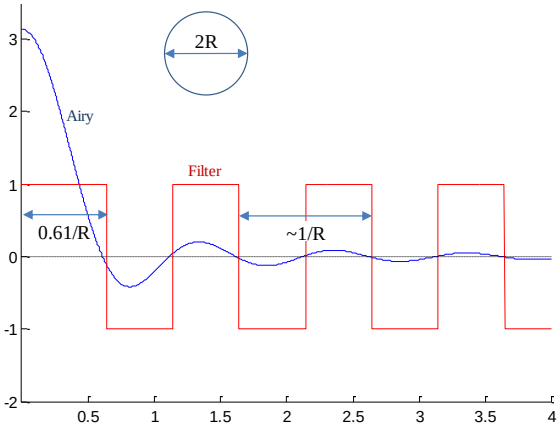

Figure 4.4. For a circular cTP with radius *R*, the matched filter changes between zero and π phase shifts as the Airy function changes sign (GPC central phase dot not shown). The central phase shifting region has a scaled radius of 0.61/*R* corresponding to the central Airy lobe, while the succeeding phase rings have a scaled periodicity of ~1/*R*.

4.1.5 Increasing peak intensities using the Gerchberg-Saxton algorithm

To emulate plane-wave focusing as much as possible, the cTP should be designed such that the amplitude distribution at the focal plane is close to uniform. This ensures that higher frequency components necessary to define sharp features optimally contribute in the formation of the output spikes. The Airy like diffraction resulting from an input with a tophat phase has most of its energy centered around the zero-order and the surrounding central lobe. Knowing how the amplitude distributions should ideally look like at both the input and Fourier planes, a phase retrieval algorithm such as the Gerchberg-Saxton (GS) algorithm [39,40] can be used as design tool. The GS algorithm iterates between the object and Fourier plane, keeping the phase at each transform while applying the desired amplitude constraints. When circular patterns are used, the 2D Fourier transforms involved in the iterations are reduced to 1D Hankel transforms [81]. Once the optimal cTP and Fourier filters are computed, they can be re-used for different cTP configurations.

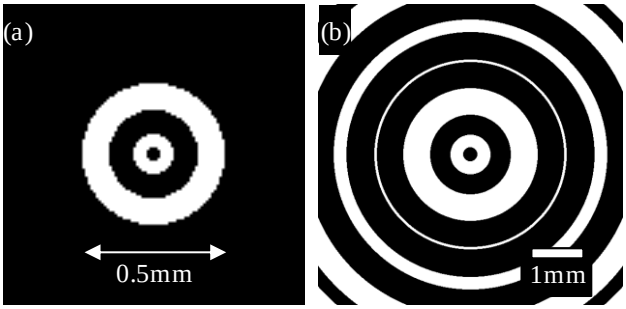

Figure 4.5. Gerchberg-Saxton optimized cTP with a 53 pixel diameter (a) and corresponding Fourier filter (b) (600x600 pixels). Amplitude constraints were based on tophats with a 26 and 300 pixel radius at the input and Fourier plane, respectively. Black and white regions have a π phase difference. (Figure adapted from [10]).

4.1.6 An alternate picture of the mGPC beam-forming principle

With some simplifications, it is also possible to explain mGPC using a geometric optics approach. Looking at the spatial Fourier plane, a matched filter acts by changing the phase of the diffracted input into a planar phase. Using several copies of the correlation target patterns at the input creates an array of output spots that resemble focused plane waves. Hence, we can, to some extent, picture the role of the correlation target pattern and corresponding matched filter as effectively creating dynamic "Fresnel" lenses, as depicted in Fig. 4.6 together with the actual Fourier lenses. In effect, an incoming collimated light can be transformed into reconfigurable spots at the output, which mimic the focusing achieved by a reconfigurable array of microlenses.

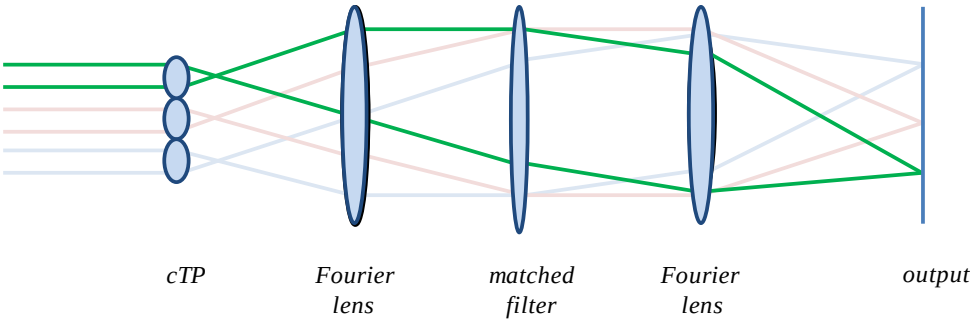

Figure 4.6. A lens system acting as an mGPC optical setup. A lenslet array takes the role of the correlation target patterns and a lens that flattens the phase takes the role of the matched filter. (Figure based on [10]).

4.1.7 Tolerance to phase aberrations

The mGPC beam shaping method also features strengths of correlation which is known for locating specific patterns within an input scene [46]. This is useful in working around unwanted background disturbances, such as those caused by SLM phase aberrations. This is also the reason why mGPC can work well with low-cost consumer devices such as LCoS pico projectors. Such phase distortions can be caused e.g., by tolerated deformations of the cover glass during manufacture, especially since the devices are not intended to be used as phase modulators of coherent light. Being inherently binary modulators, these distortions cannot be dealt with by aberration self-corrections implemented on the device itself (e.g. [58,82]).

The tolerance of mGPC to aberrations has been tested numerically by adding arbitrary phase distortions on top of the binary phase encoded input patterns. Although these disturbances will show up in standard phase contrast imaging, the matched filtering part will work to highlight the encoded patterns by integration. Hence, output spikes are still generated, even for exaggerated phase aberrations, as shown by the numerical simulations in Fig. 4.7. Moderate changes in the achievable peak intensities will also be observed as the input phase deviates from that required for optimal visibility (Fig. 4.7(c)).

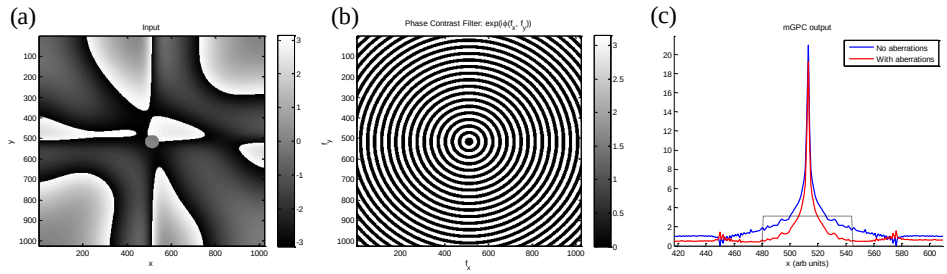

Figure 4.7. A tophat phase with simulated phase aberrations in the background (a) and its corresponding phase-only matched filter (b). Corresponding mGPC output with and without input phase aberrations (c). The dashed line indicate the applied tophat input phase. (Figure adapted from [11]).

4.1.8 Propagation behavior of mGPC generated beams

How an mGPC beam evolves as it propagates plays an important role in particle catapulting for optical sorting applications. Using the angular spectrum method, we

simulated the propagation of mGPC-generated light spikes and compared it with a tophat beam having the same power, which was used in an earlier cell sorter [7] and is commonly used in the Biophotonics WorkStation [12] having a counterpropagating geometry [13,14]. An angular spectrum simulation for 1.5μm radius tophat (Fig. 4.8(a)) and its mGPC correlated counterpart (Fig. 4.8(b)) was done for λ = 532nm in water (refractive index, n = 1.33).

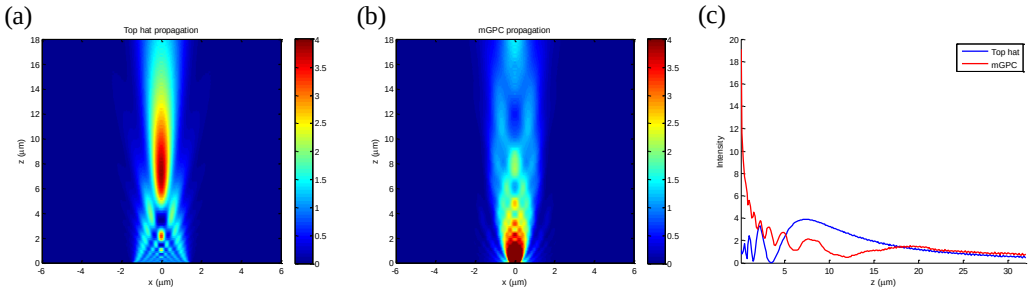

Figure 4.8. Axial section (x-z plane) of the intensity distribution for a tophat (a) and mGPC (b) beam profile, and their respective intensity profiles. (Figure adapted from [11]).

The tophat undergoes Fresnel focusing as it propagates being most intense at around nR^2/λ [8]. On the other hand, light is most intense just at the output plane for the case of mGPC, suggesting a different location for optimal catapulting. It is worth noting that mGPC's most intense region is ~3.5 times more intense than that of the Fresnel propagated tophat, suggesting an improved response in sorting or trapping applications. Another interesting feature for mGPC is that it creates a donut-like region (at z ~ 12μm for this simulation). This may be utilized well for illuminating the sides of a spherical particle wherein light is refracted more. At z ~ 20μm tail of the mGPC distribution becomes slightly more intense than that of a tophat. This suggests that it would be more effective at longer ranges which could be useful for extended applications such as cell sorting, for example.

4.2 mGPC experiments with pocket projectors

Another motivation for choosing mGPC for beam shaping is its tolerance to aberrations makes it a suitable in utilizing low end, consumer grade display projectors. By modifying the illumination of liquid crystal on silicon (LCoS) based

projectors, such devices normally used for amplitude modulation can be converted into binary phase modulators.

4.2.1 LCoS Projector anatomy

Our experiments utilized an 800×600 pixel LCoS device manufactured by Syndiant (SYL2043) that comes with the Aiptek T25 PocketCinema projector. Under normal use LCoS projectors perform amplitude modulation by selectively rotating the polarization of incoming light by ±90°. Light from LEDs is polarized horizontally as it passes through a wire grid polarizing beams splitter (PBS) on its way to the LCoS. Upon reflection the polarization state will change depending on whether it reflects from an LCoS "white" region. If the polarization changed, this light will gets deflected on its second pass to the PBS and then get redirected towards the image projection optics. On the other hand light that falls on the LCoS black region, will keep its polarization and just pass through the PBS upon reflection. This operation principle is shown in Fig. 4.9, where a photograph of a disassembled pico projector is also shown.

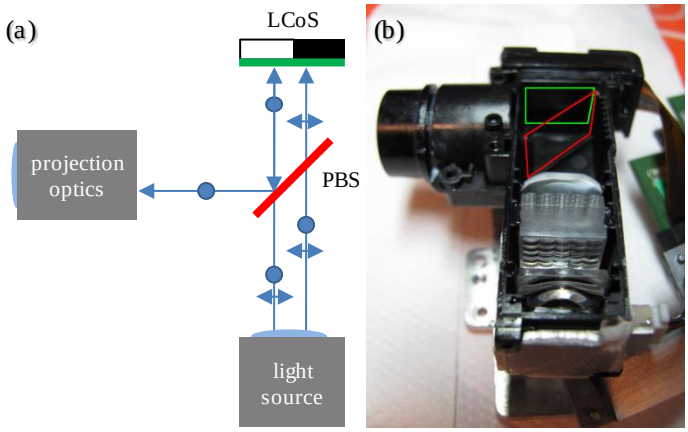

Figure 4.9. Operating principle of a commercial LCoS based display projector (a) and a disassembled pocket pico-projector with the LCoS and PBS highlighted in green and red respectively.

4.2.2 Experimentally finding out the LCoS's phase modulation mode

We performed experiments to identify the necessary polarizations for both amplitude and phase modulation. A method based on analyzing the LCoS's output over a range of input polarization states was suggested in [83]. However, we devised a method based on what equipment was already available in our lab. Hence we used an interferometric approach, which was also visually more intuitive. The schematic of the setup is shown in Fig. 4.10. A λ/2 waveplate turns the linear polarization of a collimated and expanded laser beam (532nm Excel, Laser Quantum), which is incident on the LCoS device through a beam splitter. The beam splitter redirects light coming from the LCoS through an analyzer (P) and a 4f setup consisting of two f = 300mm lenses that images the LCoS device plane onto a CCD camera.

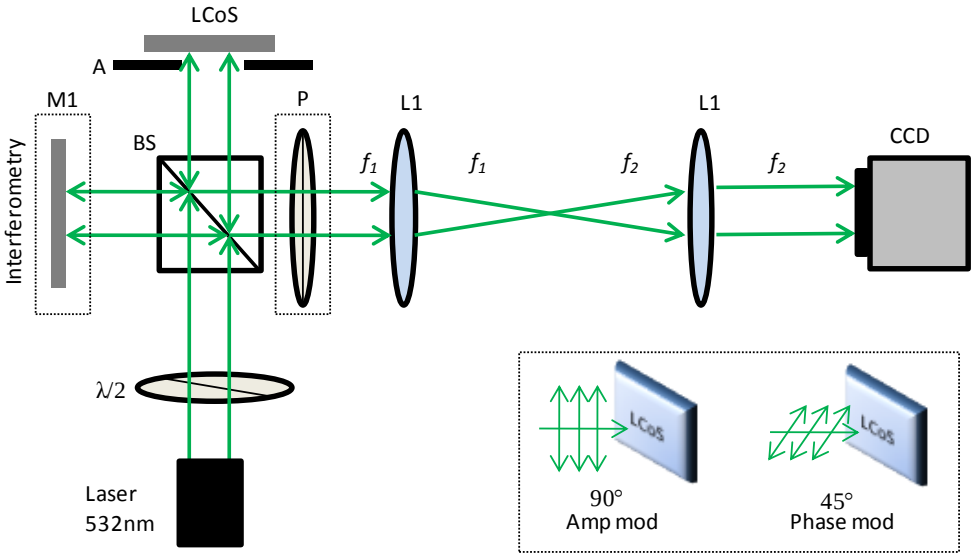

Figure 4.10. The setup used for analyzing amplitude and phase modulation modes of the applied LCoS device. The analyzer, P, is used to visualize amplitude modulation while the mirror, M1, is used to visualize phase modulation. The inset in the lower right shows example polarization states for amplitude and phase modulation modes. (Figure based on [10]).

The LCoS projector's amplitude modulation scheme is replicated when the incident polarization is either at 90°(vertical) or 0°(horizontal), and the analyzer is perpendicular to it (0° or 90° respectively). This suggests that the LCoS device can act as a phase modulator when the incident polarization is at -45° [84].

To verify the achieved phase modulation, the setup can be converted to a phase imaging Michelson-like interferometer by removing the analyzer and adding a mirror, labeled M1 in Fig. 4.10, to direct a collimated reference beam to the camera through the 4*f* setup. With the LCoS plane sharply imaged at the camera, the resulting interference fringes enable visualization of any resulting spatial phase modulation. For comparison, we start with an amplitude-modulation configuration and record the striped pattern as shown in Fig. 4.11(a). While maintaining the same pattern on the LCoS device, we shift to an interferometric geometry and observe that rotating the incident polarization to -45° achieves the desired spatial phase modulation behavior as exemplified by the shifted fringes between the regions creating the black and white amplitude stripes originally (Fig. 4.11(b)). Line scans taken from the interferogram show a π phase difference between stripes encoded with black and white as indicated by how their minima and maxima align.

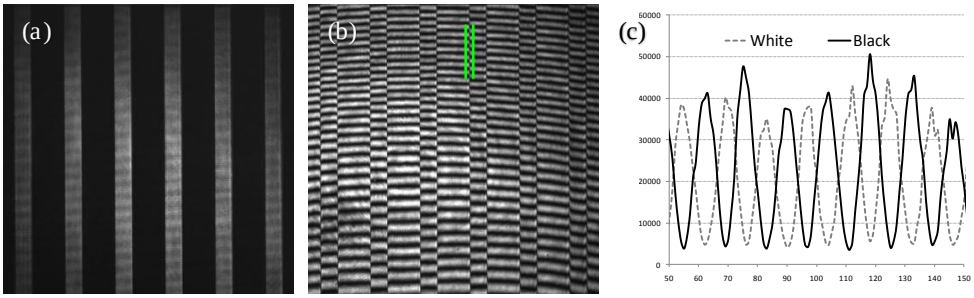

Figure 4.11. Vertical stripes displayed via normal LCoS-projector operation showing amplitude modulation (a). Corresponding fringes in phase modulation mode obtained using a mirror for the reference wave (b). Line scans taken from the green highlights in (b) show the π phase difference between stripes encoded with black and white (c). (Figure adapted from [10]).

4.2.3 Pixel pitch of the LCoS

Knowledge about the LCoS pixel pitch allows conversion of pixel units in the desktop to real world length units. Although Syndiant's website claims that the pitch of their LCoS devices can be as small as 5.4 microns this turns to be not the

case for all their LCoS models [85]. The pitch could have been derived through diffraction experiments, but we chose to measure it more directly by obtaining microscope images and comparing with a 1951 USAF resolution target (Fig. 4.12). Post analysis reveals that the pitch[5] for this SYL2043 model is around 9.5μm.

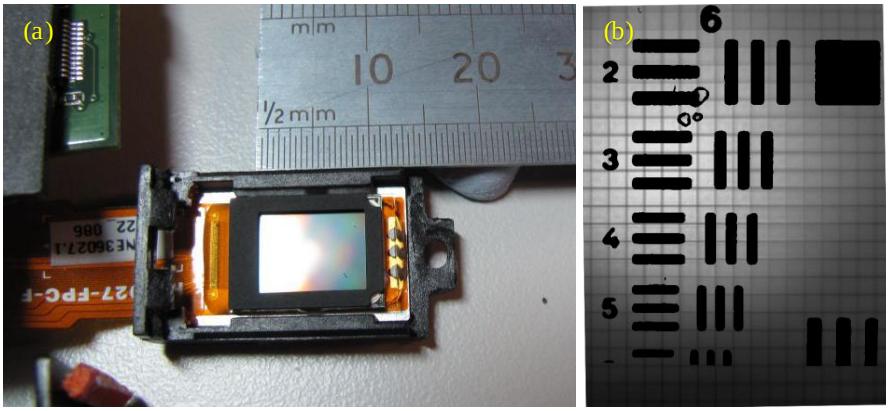

Figure 4.12. The LCoS chip which measures about a centimeter across (a). The aligned, enhanced and superposed images show that the LCoS pixels are slightly smaller than element 5 of group 6 of the USAF target, corresponding to 102 line pairs per mm or 9.8μm per line pair (b).

4.3 Beam-forming experiments

With the LCoS device operated as input binary-phase spatial light modulator, the next step is to insert a phase-only spatial correlation filter at the Fourier plane in order to implement a functional mGPC setup (Fig. 4.13). In our first demonstration, instead of using a pre-fabricated phase filter optimized for a given cTP, a second device, LCoS2, has been applied, making it easy to tune matched filter for initial optimization. Light from LCoS1 is thus focused to LCoS2 with a f_1 = 300mm lens. A second non-polarizing beam splitter is used to sample light that have gone through LCoS2. Figures 4.14(e-f) show the resulting optical spikes when encoding the binary Fourier phase filter (insets in Fig. 4.14(b) and 4.14(c)) on LCoS2. The resulting output for a cTP based on an input phase disk with a 53 pixel diameter is shown with and without a binary Fourier phase filter encoded (Fig. 4.14(d-e)). For

[5] As of 2013 though, Syndiant has released documentation on their LCoS's on their website. The documented pixel size of the SYL2043 model is 9.4μm [132]. It is not clear whether the 0.1 difference constitutes the dead space or whether our measurement deviates.

the same disk diameter an increase in the peak intensity and a narrower spike is observed when using a GS-optimized cTP and matched phase filter as shown in the superposed line scans in Fig. 4.15. The disk based and GS optimized mGPC output show peak intensity gains of 7.2 and 11.9 respectively when compared to the average 4*f* imaging flat output.

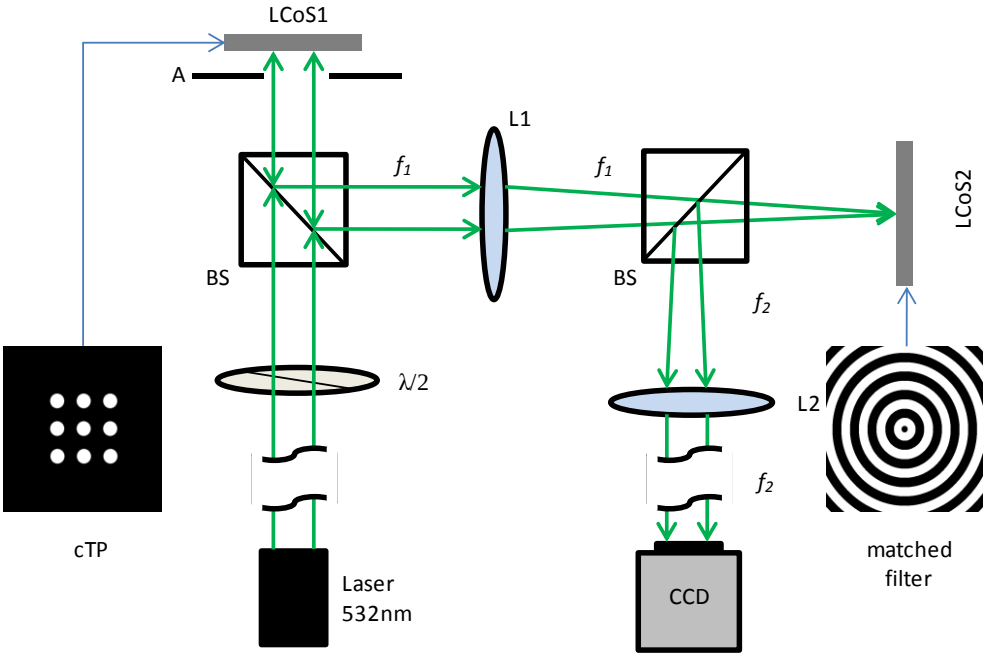

Figure 4.13. The mGPC setup utilizing two pico-projector LCoS-devices for creating the desired dynamic correlation target patterns and matched binary Fourier phase filters required for beam-forming. (Figure based on [10]).

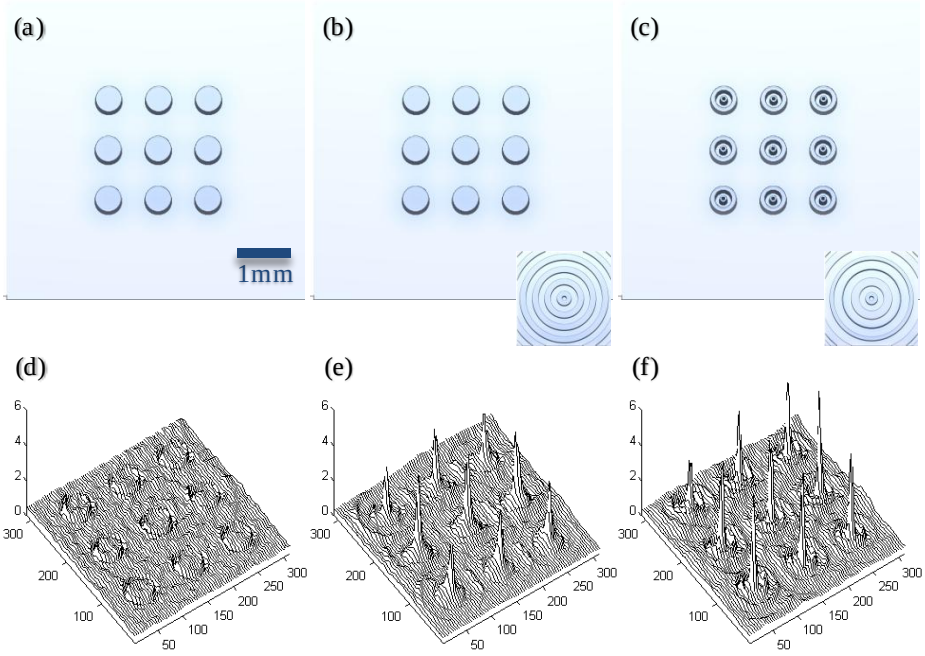

Figure 4.14. Example mGPC input phase patterns consisting of 53 pixel diameter disks and the resulting output without Fourier filtering (a & d). Output with applied matched Fourier phase filtering (c & e). Output using a GS-optimized cTP with the same input diameter pattern (d & f). Insets in (b) and (c) show the binary-phase matched filters used. (Figure based on [10]).

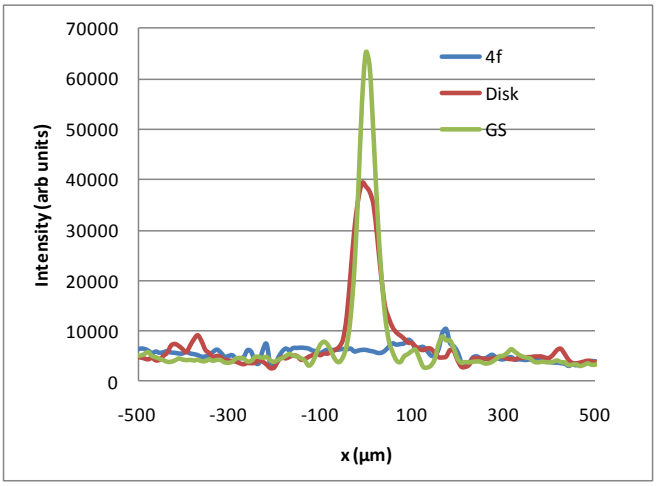

Figure 4.15. Line scans comparing the intensities of generated spot profiles. (Figure based on [10]). The disk based and GS optimized mGPC output have peak intensity gains 7.2 and 11.9 with respect to the average 4*f* imaging output.

Figure 4.16 shows snapshots from a video recording demonstrating the potential use for optical manipulation. The GS optimized patterns were programmed to trace a star. Although the encoded sequence used is pre-calculated, it is only necessary to translate the cTPs to move the spots around.

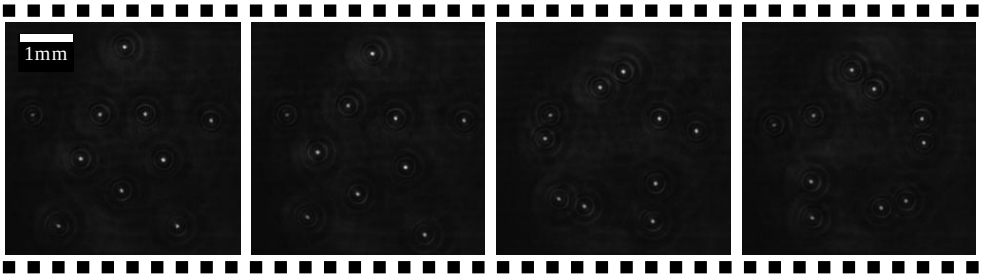

Figure 4.16. Experimental snapshots from a movie sequence showing the potential for real time optical manipulation. 10 mGPC spots move along the perimeter of a star figure.). (Figure adapted from [10]).

4.3.1 Spike intensity encoding through time integration

As the projector only has black and white states, it uses pulse width modulation to define states between black and white which are perceived as appear as gray via time integration. Although we were not able to directly see the pulses due to

unknown equipment responses in the experiment, we were able to verify that the LCoS switches at 180 Hz. This can also be deduced from how it switches between red, green and blue imaging channels while having a typical 60Hz color image frame rate. Oscilloscope readings from a photodetector are shown in Fig 4.17.

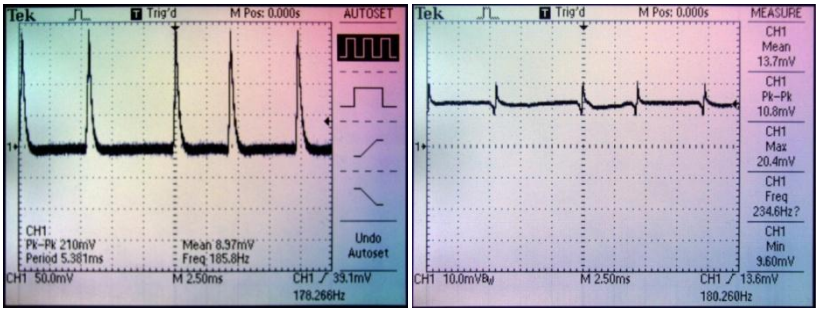

Figure 4.17. Oscilloscope screen readings showing the LCoS's ~180Hz switching rate.

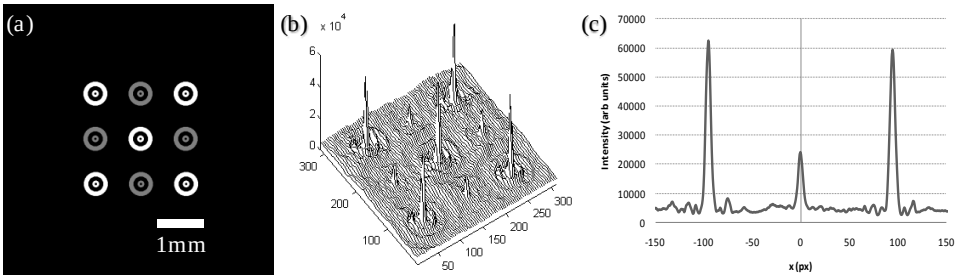

Figure 4.18. Correlation target patterns optimized via the Gerchberg-Saxton algorithm wherein some of the patterns have 50% gray levels encoded (a). The resulting optical output with intensity variations corresponding to the gray-levels encoded (b and c).). (Figure adapted from [10]).

Since video frame switching rates are typically far above required refresh rates for stable optical trapping and manipulation (~5-20Hz) [56], it can be expected that this time integrated intensity modulation would not be an issue for applications that don't require very high position stabilities like potential microtools for simple mechanical cell handling (Chapter 5) or cell sorting. Hence, even if continuous phase levels cannot be mapped to intensity levels, this time integration based output intensity modulation scheme may still effectively be used for 3D manipulation based on counter-propagating beam traps [66]. Figure 4.18(a) shows

changes in encoded gray levels corresponding to changes in output intensity levels (Fig 4.18(b) and 4.18(c)).

4.4 Experiments with a fabricated matched filter

Having done the initial matched filter optimizations, we built a more compact setup by getting rid of the second projector from the previous experiment. A filter array for different cTP radii was fabricated (photolithography mask drawing shown in Fig. 4.19(a)), but we settled in using a 50 pixel (475μm) diameter filter in the mGPC experiments.

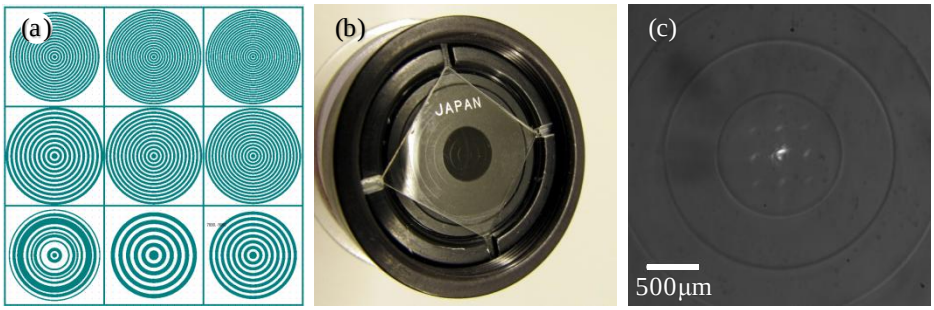

Figure 4.19. Mask layout (2"x2") (a) used for fabricating an array of mGPC filters in Pyrex glass. One of the filters mounted at the back of a microscope objective (b). Brightfield microscope image of the fabricated matched phase filter with an easily recognizable Fourier transform pattern diffracted from a binary input grating (c).

4.4.1 Matched filter fabrication

The matched phase filter is fabricated by etching out photolithography-transferred patterns on Pyrex (n = 1.474). The etched regions have a depth of ~561nm to give a $\lambda/2$ optical path difference. Etching with hydrofluoric acid took ~7 minutes at the estimated etch rate of 80nm per minute (experimentally determined). The patterns in the matched filter are scaled for λ = 532 nm, and an f = 300 mm Fourier lens. To exploit the improved fidelity over a pixilated LCoS filter, we numerically calculated the zeroes of the Airy function and use it to set the radii of the filter's concentric rings (see Appendix 2). The GPC central phase dot has a radius of 21.46μm chosen to give optimal contrast when the 5.7 × 5.7 mm^2 area (600 × 600 px^2) of the LCoS is illuminated with a tophat beam. The filter is then clamped near the back focal plane of the objective lens (f_2 = 8.55 mm, NA = 0.4) which in turn performs an inverse Fourier transform of the filter plane. A microscope photograph

of the matched filter with a coinciding Fourier diffraction pattern is shown in Fig. 4.19(c). Unlike a dynamic LCoS, the fabricated filter has less alignment constraints, being polarization independent, and is much more compact. Lateral features in the fabricated filter do not suffer from pixilation and can be as small as ~1.5μm in wet etched Pyrex.

4.4.2 Generation of high intensity high contrast mGPC spikes

The optical setup which now uses the fabricated matched filter is shown in Fig. 4.20. For this experiment we used a Philips Picopix 1430 which can be conveniently operated as an extended desktop while user control is done through the primary desktop. Just like the Aiptek projectors, the Picopix also uses a Syndiant SYL2043 LCoS chipset. The LCoS is illuminated obliquely to avoid using a beam splitter that would otherwise remove 75% of the incident power. The slight skew introduced to the projected patterns is ignored to avoid complicating the corresponding matched filter design. This can, however, be dealt with when fabricating the filter if further optimization is desired for a particular geometry. For prototyping simplicity, imaging is done through a 4*f* microscope setup on top of the sample plane. This also simplifies alignment as the matched filter and Fourier plane can be imaged simultaneously by adjusting the top objective. For sample illumination, light from an LED can be introduced through a dichroic mirror.

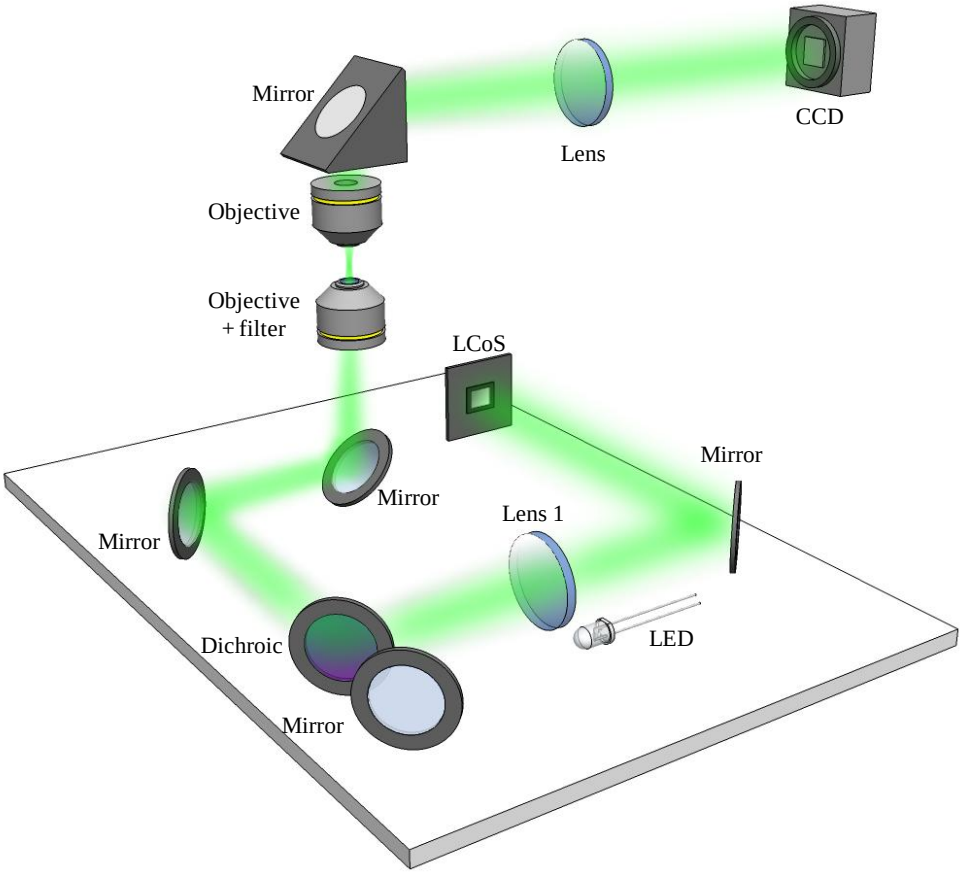

Figure 4.20. Experimental setup. The LCoS is illuminated with a 45° polarized green laser to effectively operate as a binary phase-only SLM. Lens 1 focuses light into the matched phase filter near the back focal plane of the objective which in turn forms the mGPC output spots. A 4*f* microscope images the results on the CCD. For optional sample illumination, an LED provides light which enters the system via the dichroic mirror. (Figure adapted from [11]).

4.5 Results

To generate spot patterns, binary phase disks with 50 pixel diameter were drawn to the pico-projector LCoS. The corresponding Fourier plane Airy disk has a central lobe diameter of 821 μm and concentric rings located at ~337 μm radius intervals. Figures 4.21(a) and 4.21(b) illustrate experimental results showing high contrast

mGPC spike arrays forming arbitrary patterns. By programming a scanning motion such spot arrays can be used for e.g. microscopy applications [30].

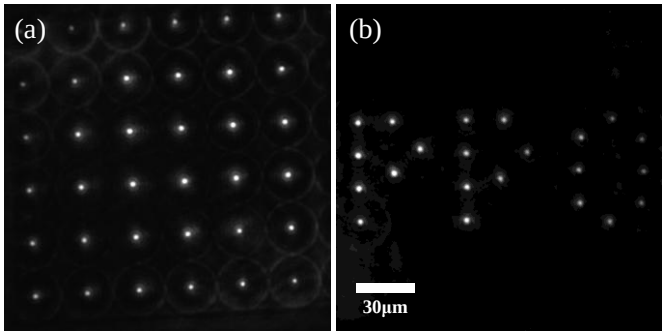

Figure 4.21. Spot arrays generated via mGPC showing a periodic lattice also useful for programmable array microscopy (a), dotted letters forming “PPO” (b). . (Figure adapted from [11]).

4.5.1 Line pattern generation

In addition to "focused" spots, mGPC can also generate continuous line patterns that are useful in certain applications, e.g. for photo-excitation of extended segments of neurons [6,7], faster 2PP microfabrication or structured illumination microscopy. Instead of distinct circles, line patterns with a thickness matching the diameter of the disks are encoded at the SLM input phase (Fig. 4.22).

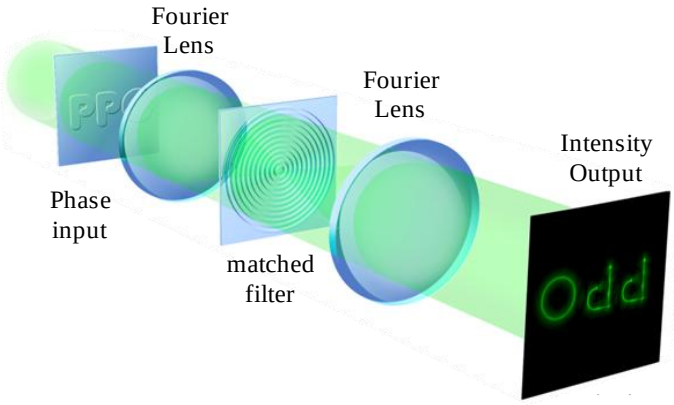

Figure 4.22. A 4*f* mGPC setup wherein extended line patterns are encoded in the input phase. Instead of discrete spots, sharp line intensity patterns are formed at the output.

An example of a pattern being drawn is shown in Figure 4.23. Since a line can be considered as a collection of closely packed disks, the intensity becomes weaker as each disk takes away energy from its neighboring disks. Figure 4.24 shows sample phase input containing line patterns of letters forming "DTU" and "PPO", and the resulting intensity patterns that are generated when these phase patterns are used with mGPC. Points where the lines end or intersect need to be dealt with as the correlation with a disk respectively gives a stronger or weaker peak in these regions. For example, the line ends may be drawn less circular to suppress the correlation peak. If a multi-level phase SLM is used, the variations in intensity may be compensated for by encoding different phase levels, such that the GPC part of the optical processing can form different intensity levels.

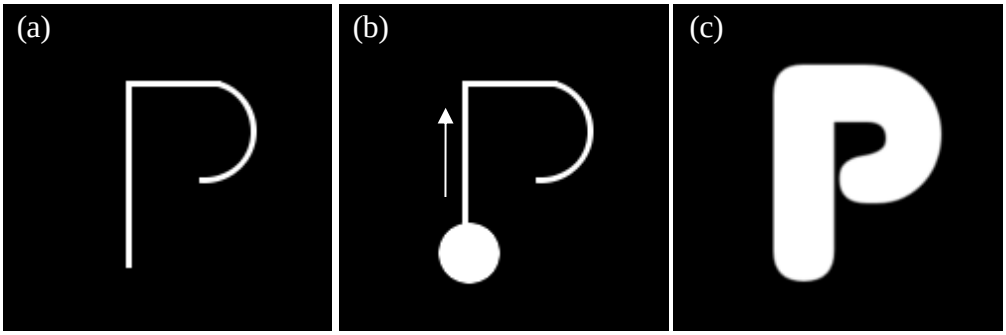

Figure 4.23. Example method for creating phase distributions for an arbitrary line pattern. The desired line intensity pattern (a) is traced by the circular target pattern designed for the matched filter (b). Hence, the resulting binary phase input pattern (c) is a thickened version of the desired output intensity pattern. Although this example depicts a manual way of drawing phase patterns, more convenient methods would be a matter of programming and image analysis. . (Figure adapted from [11]).

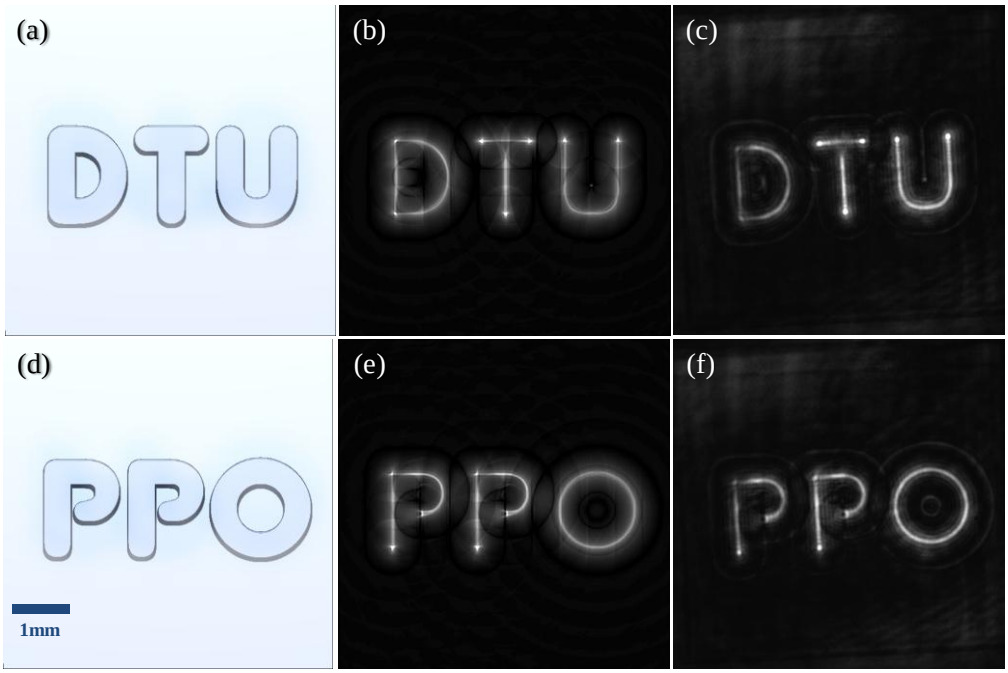

Figure 4.24. Generation of line patterns from letters forming "DTU" and "PPO". Binary phase patterns encoded at the pico projector LCoS SLM, (a) and (d), are shown with corresponding numerically calculated output intensities, (b) and (e), and experimentally reconstructed intensity patterns (c) and (f). . (Figure adapted from [11]).

4.6 Conclusion and outlook

This chapter presented mGPC and its use with low cost projectors. The similarities of mGPC with phase-only correlation makes it robust against device imperfections [79]. Such robustness thus offers a cheaper alternative for beam shaping applications like programmable microscopy and optical trapping. With improvements mGPC can be further adapted to applications such as optical cell sorting [29,86], real time line pattern formation, programmable microscopy, or even two photon polymerization used for fabricating microtools [25].

5 Light driven microtools

Beam shaping techniques like the ones discussed in previous chapters have been important in biophotonics research through applications such as imaging, targeted light delivery or optical trapping and micromanipulation. However, much more can be studied if research tools are not limited to beam shaping alone, especially since light can be used to move things around. Although it is common and convenient to optically manipulate readily available samples such as cells or microspheres, researchers can now manipulate specifically designed objects, thanks to the development in microfabrication. Hence, in order to extend the applications of optical manipulation recent research has lead towards the use of so called "microtools."

A technological milestone that leads to the development of such microtools, is the ability to fabricate intricate structures in the microscopic scale. In recent news and popular media, 3D printing have been gaining appeal amongst hobbyists and entrepreneurs, igniting creativity and challenging traditional concepts about production. Microscale 3D printing, however, have been in the laboratories for more than a decade [20]. In fact, a recently claimed smallest "3D printer" was made by people who initially worked on 3D printing microscopic structures [87]. This microscopic 3D printing works by directly scanning a laser to solidify liquid polymer. This process, known as direct laser writing (DLW), achieves high resolutions by utilizing nonlinear two photon photopolymerization (2PP). Hence, tiny objects with features below 100nm are produced by scanning focused pulsed light along programmed paths.

We therefore optically manipulate DLW custom fabricated structures to provide functionalities that cannot be achieved with typical microspheres. Complex microstructures, in turn, would provide more application specific optical manipulation experiments. For optimization, designs obtained from theoretical or numerical models can be used prior to the fabrication of such light driven microtools.

5.1 Microscopic 3D printing

About a decade after Kawata's iconic microbull sculpture (Fig. 5.1(b)), the 2PP process of fabricating microscopic objects have been widely used in many laboratories and is now even being commercialized (Nanoscribe, Fig. 5.1(c)). Although there have been many improvements over the decade such as using techniques from STED microscopy or developing photoresists with higher energy thresholds [88], the basic principle of 2PP (Fig. 1(a)) is still applied in current microfabrication facilities.

When exposed to photons with a given wavelength (energy), liquid photoresists such as SU8 solidify. Controlling and localizing this solidification process is the key to creating intricate microstructures. 2PP exploits the very low probability of two photons to meet elsewhere except where light is most intense. Photoresists used for 2PP are those that do not respond to single photon radiation but solidify with the combined energy of two photons. Hence, typical 2PP facilities consist of a high NA objective, a nanometer-precision scanning stage and a femtosecond laser. Focusing from a high NA immersion objective ensures that the focal volume is as small as possible typically around a hundred nanometers [20,25,88], but features can go below 25nm [89]. The precision stage serves to scan this focal volume through the photopolymer. The compressed light pulses from a femtosecond ensures high energies at the right moment when two photon absorption takes place while maintaining a moderate overall average energy, thus avoiding effects like heating and over-exposeure.

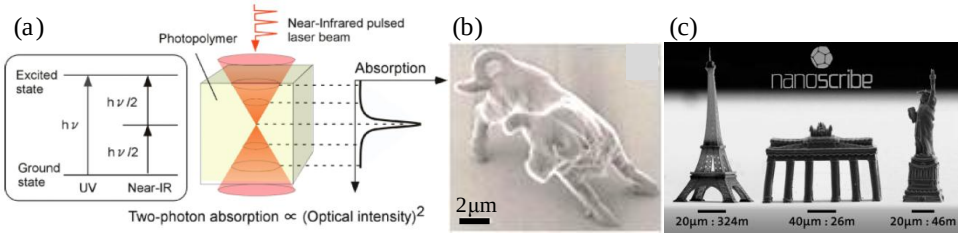

Figure 5.1. DLW process (adapted from [90])(a), Kawata's microbull (scalebar 2um) (adapted from [20])(b), and miniature versions of iconic landmarks (c) produced with a commercial 2PP system (adapted from [88]).

5.2 Combining micromanipulation and microfabrication

Functional microdevices have been envisioned as early as Kawata's pioneering works in 2PP [20]. To date, microscopic light driven versions of propellers [21], wings [22], sailboats [91], and other machines inspired by fluid- and aerodynamics have been successful demonstrations of light and matter interaction. However, microstructures designed for more specific applications are relatively new. With optical micromanipulation providing a controlled means of actuation, a step towards the development of microtools is the structural isolation of the optical trapping features from the tool's end purpose such as sensing, probing or delivering stimulus. This isolation is achieved through optical handles that allow maneuverability around the object or specimen where the tasks are to be performed. An earlier work that utilizes such optical handles was demonstrated in [28] wherein planar structures are "cut-out" to have circular ends (Fig. 5.2(a)), allowing manipulation with 6 degrees of freedom (Fig. 5.2(b)). This was later improved by using 3D designs, wherein spheres which are more optimal for trapping at any orientation serve as the tool's handles [25].

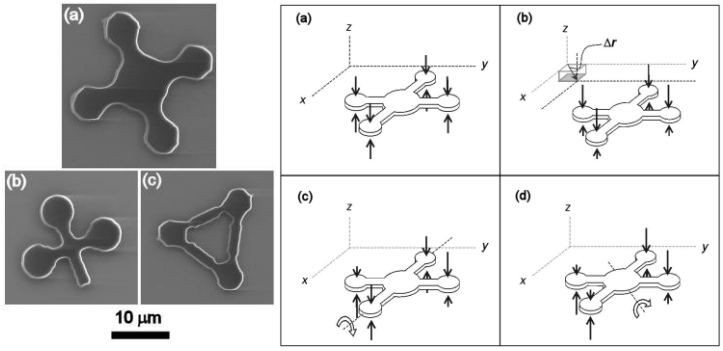

Figure 5.2. Planar microstructures that can be manipulated with 6 degrees of freedom using multiple counter-propagating traps. (Figure adapted from [28]).

Using this tool-handle paradigm together with interactive 3d multi-trap articulation, microtools for probing force microscopy [24] or surface tomography [23], targeted super focused light delivery [25], or even just brute force mechanical probes for poking around (Fig. 5.3) have been demonstrated. Furthermore, several microtools can be simultaneously controlled with a joystick to probe a cell from opposite directions, thus keeping the cell in place (Fig. 5.4).

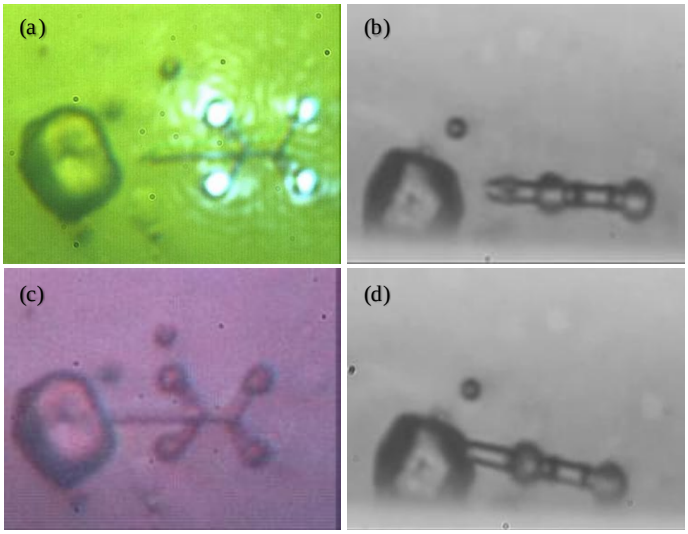

Figure 5.3. Snapshots from concurrent top-view (left column) and side-view (right column) microscope images of light-driven microtools mounted on four-lobed handles. The photograph without the NIR filter (a) shows the location of the trapping light. In (c) and (d) the tool is optically driven to poke a plastic "rock".

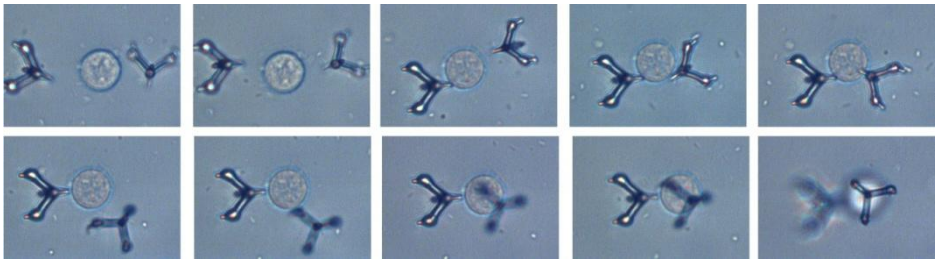

Figure 5.4. Steering nanotips around a Jurkat T-cell. Two nanotip tools steered around the cell. One nanotip is held fixed against the cell membrane while a second tool is steered above the cell.

While primary control is done through handles accessible to diffraction limited beam shaping, targeted applications can get as small as fabrication allows. More advanced fabrication can be used to assemble composite microtools from different materials which can include nanorods, nanotubes and other nanoparticles [92–94] attached to easily trapped microspheres. Microtools thus enable *structure mediated*

micro-nano coupling [95]. In the work presented here, green light going through a 1 micron facet is eventually enhanced as it is guided and confined through a tapered tip (~100nm). With position steering done through optical handles, such coupling may be used for delivering light into localized and otherwise hard to reach targets.

5.3 Wave-guided optical waveguides

Waveguides are useful for delivering light through arbitrary directions. They have been important in communications as fiber optics for routing information in ways that are much more efficient than free space data transmission. This feature can be scaled down to deliver targeted and localized light into cells [96]. Thus waveguiding offers a greater flexibility compared to light freely propagating in homogeneous media. It had been shown that tapered waveguides can cause adiabatic or super focusing of either surface plasmons [97,98] or light [99]. Although the results are promising in terms of focusing power, the use of tapered fiber optic presents some positioning limitations. On the other hand, steering free standing waveguides offers more directional flexibility when used with an interactive optical micromanipulation platform such as our BioPhotonics workstation. Working in reverse, light can also be coupled through tapered tips for sensing applications similar to near field scanning optical microscopy [100] .

5.3.1 Waveguide properties

As a free standing waveguide can have varying orientations, the input beam can enter the waveguide from different angles. To be able to operate the waveguide microtool at varying angles, it is therefore necessary to have some tolerance with respect to the coupling of light. For a microtool made of SU8 ($n_{waveguide}$ = 1.6), with a input facet diameter of D = 1μm, surrounded water ($n_{background}$ = 1.33), the numerical aperture is given by

$$\mathrm{NA} = \sqrt{n_{waveguide}^2 - n_{background}^2} \sim 0.89 \tag{5.1}$$

This NA corresponds to an acceptance cone of 42°. Such waveguides would also be strongly guiding (weakly guiding condition: $\mathrm{NA}^2 << 2n_{background}$). This is important since, owing to their microscopic dimensions, the waveguide would have a rather

small bending radius, which could cause losses in the guided modes. Furthermore, the *V* parameter [48], used with fiber optics, is above 2.405 indicating multi-mode operation for the wavelength, λ = 532nm.

$$V = \frac{D\pi}{\lambda} NA = 5.26 > 2.405 \tag{5.2}$$

Light coming at a range of incident angles, corresponding to different modes, would therefore still be able to propagate through the waveguide. The single mode condition would be satisfied if the coupled light's wavelength exceeds 1130nm (near infrared). This also suggests multimode behavior if the trapping laser, λ = 1070nm, is used for coupling.

5.4 Modeling of light matter interaction in microtools

Because of its scale and inhomogeneity, the micro-to-nano coupling of light in microtools can no longer be suitably described by geometric or Fourier optics typically used for designing setups or beam shaping. The incident trapping or coupling of light can behave in new ways depending on the microtool's geometry. It then becomes necessary to analyze light's behavior within these microtools with a more general model. The freedom in design offered by DLW makes it important to use models that can handle complexities and take in little assumptions about the system. Hence, we use the finite difference time domain (FDTD) method which is a direct discretization of the fundamental Maxwell's equations [102]. Using the FDTD, we investigate light propagation through microstructures as well as the field enhancement as light comes out of our tapered waveguide designs. Such calculations save time as it helps optimize the structures prior to fabrication and experiments.

In addition to field distributions, optical forces can also be obtained using the Maxwell stress tensor formulation. By calculating the forces on bent waveguides subjected to tailored static light distributions, we demonstrate novel methods of optical micromanipulation which primarily results from the particle's geometry as opposed to the light's direct motion as in conventional trapping.

5.4.1 The finite difference time domain method

The finite difference time domain method is based on discretizing Maxwell's curl equations, which for current and charge free media, as is often the case in optics, reduce to

$$\nabla \times \vec{E} = -\mu \frac{\partial \vec{H}}{\partial t}$$
$$\nabla \times \vec{H} = \varepsilon \frac{\partial \vec{E}}{\partial t}. \tag{5.3}$$

Space is discretized with sampling intervals Δx, Δy, Δz along x, y, and z respectively. Similarly, time is discretized with a sampling of Δt. After expanding Maxwell's equations and replacing the differentiation with finite differences, the future state of the electric (magnetic) fields at time $t + \Delta t/2$ are solved from its past state at time $t - \Delta t/2$ and the spatial derivatives of the magnetic (electric) field at time t.

In our 2D, z-invariant simulations wherein the electromagnetic field only contains E_z H_x and H_y components, Maxwell's equations are reduced to the following discretized equations

$$\begin{aligned} E_z\left(x, y, t + \frac{\Delta t}{2}\right) &= E_z\left(x, y, t - \frac{\Delta t}{2}\right) \\ &+ \frac{\Delta t}{\varepsilon(x, y)}\left\{\frac{\left[H_y\left(x + \frac{\Delta x}{2}, y, t\right) - H_y\left(x - \frac{\Delta x}{2}, y, t\right)\right]}{\Delta x}\right. \\ &\left. - \frac{\left[H_x\left(x, y + \frac{\Delta y}{2}, t\right) - H_y\left(x, y - \frac{\Delta y}{2}, t\right)\right]}{\Delta y}\right\} \end{aligned} \tag{5.4}$$

$$H_X\left(x,y,t+\frac{\Delta t}{2}\right) = H_x\left(x,y,t-\frac{\Delta t}{2}\right) - \frac{\Delta t}{\mu(x,y)}\frac{\left[E_z\left(x,y+\frac{\Delta y}{2},t\right)-E_z\left(x,y-\frac{\Delta y}{2},t\right)\right]}{\Delta y} \quad (5.5)$$

$$H_y\left(x,y,t+\frac{\Delta t}{2}\right) = H_y\left(x,y,t-\frac{\Delta t}{2}\right) + \frac{\Delta t}{\mu(x,y)}\frac{\left[E_z\left(x+\frac{\Delta x}{2},y,t\right)-E_z\left(x-\frac{\Delta x}{2},y,t\right)\right]}{\Delta x} \quad (5.6)$$

New field values overwrite the memory of past field values since they are no longer needed in subsequent calculations. In our 2D simulations, the structures and fields are assumed invariant along the *z* direction ("transverse to the array"), hence the E_z, H_x and H_y can be calculated independent of the other three components. For these waveguide simulations, the *x* and *y* directions where chosen to coincide with the column index and row index respectively.

We thus first simulated waveguiding, and field enhancement on a bent and tapered waveguide. For force calculations, we first obtained the steady state fields via FDTD, and then proceeded on calculating forces on bent waveguides by applying Maxwell's stress tensor formulation.

5.4.2 FDTD simulations of optical propagation through the waveguide microtools

Due to the run time and memory constraints, set by the discretization requirements and size of the microtools, we only use 2D simulations to obtain the general behavior of light propagation. Alternatively finite element methods (FEM), or FDTD based software that use adaptive discretization can be used run a full 3D simulation. For future optimizations, it is also possible to isolate the body and tip of the microtool to exploit existing FDTD algorithms optimized for cylindrical geometries [103]. Our 2D calculations are performed along the microtools' plane of symmetry, where the relevant optical phenomena take place. Thus, without loss

of generality, we assumed that calculations with fields that are invariant along the *z* direction (perpendicular to the 2D array's chosen axes) and that these can hint us about the actual behavior in 3D. In addition to memory constraints, expected variations in 2PP microfabrication also prevented us from making rigorous analyses.

The typical wavelength used in our optical micromanipulation setup is 1070nm for trapping and 532nm for coupling. We choose the space discretization such that 1μm is sampled with 50 data points ($\Delta x = \Delta y = \Delta z = 20$nm). We use a 2048x1024 array which has an equivalent field of view (side view) of about 40x20μm^2. To further save on memory we use second order Mur absorbing boundary conditions [104] which are based on alternatively solving the wave equation instead of perfectly matched layers that attenuate the fields towards the boundaries. Simulations were done with MATLAB and each took roughly 30 minutes on a 2GHz i7 laptop with 4GB of memory.

With the settings and assumptions stated earlier we simulated fields that are transverse magnetic to *z* (transverse electric to *z* simulations show similar behavior). We started with a simulated light source having a vacuum wavelength of 532nm and examined its propagation through a bent, step-index dielectric waveguide assumed to be polymerized SU8 (n = 1.6) immersed in water (n=1.33). Figure 5.5 shows the time-averaged intensities of the light propagation through the waveguide obtained after 6144 time steps.

A Gaussian source with a flat phase is chosen such that its beam waist (FWHM) matches the waveguide's input facet, $D = 1$ μm (see the incoming beam intensity linescan in Fig. 5.6). This source was introduced using a total field/scattered field approach [105]. Given a normalized waveguide parameter of 5.26, a straight waveguide would support multimode operation. However, this would not necessarily mean a multimode output from the bent waveguide considered here due to its small bending radius (R = 5.8 μm) and tapering towards the end (~14°).

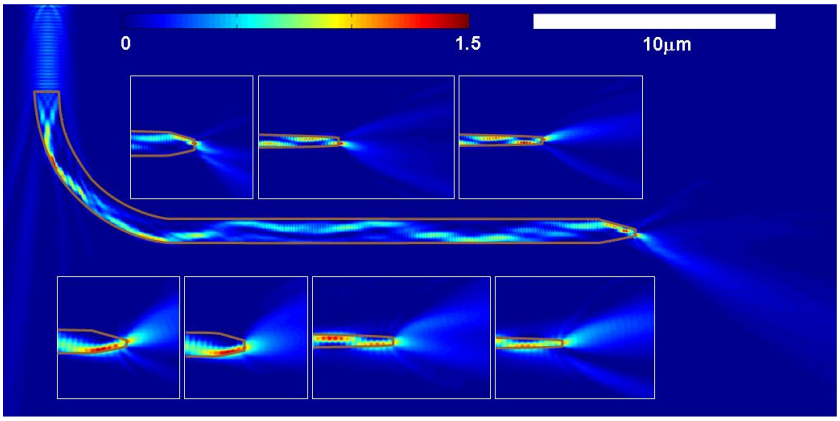

Figure 5.5. FDTD model of propagation (λ = 532nm) through a bent polymer waveguide (SU8, n=1.6; bend radius R, = 5.8μm) that is immersed in water (n=1.33). Insets show the field near the tip for different tapers and illumination wavelengths (top: λ = 532nm; bottom: λ = 1064nm). Figure adapted from [25].

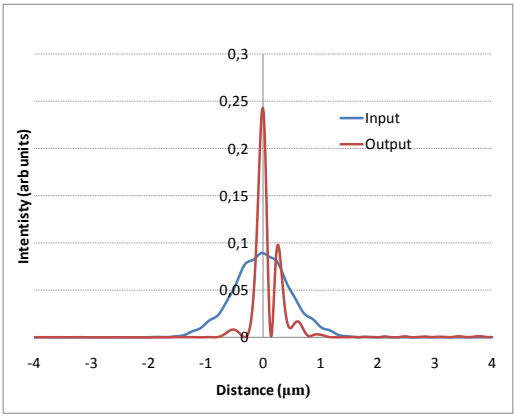

Figure 5.6. Intensity linescans taken along the input and output of Fig. 5.5 show that light exiting the tip (red) is narrower and has higher peak intensity than the incoming light (blue).

The simulation results in Fig. 5.5 show that the beam develops a narrow intense peak once the beam enters the waveguide. The beam encounters some leakage loss at the bend, but most of it is guided further, albeit with reduced peak intensity as the beam propagates through the horizontal section. However, the peak intensity rises again when the beam enters the tapered end. This allows a narrow intense peak to be coupled out of the tip, which then quickly spreads as diffraction effects set in. Hence, the light coupling out of the tip exhibits higher peak intensity and

tighter light confinement compared to the incoming light (see the comparison of the line scans in Fig. 5.6). While the incoming beam width can be produced by NA ~ 0.5 air-immersed objective, reproducing the same FWHM as the outgoing light will require using an immersion objective having NA ~ 1.25. The peak intensity levels at the input and output are 0.089 to 0.24, respectively (arbitrary unit) from which we obtain a gain of ~2.7. Such an intensity gain can be used to trigger localized nonlinear processes such as two photon absorption, for example.

The two functions – redirecting incident vertical light sideways and producing a more intense and tightly confined light at the tip – are also observed when using other tip tapering profiles for green beam, λ=532nm (see lower insets, Fig. 5.5). The upper insets of Fig. 5.5(a), which depict time-averaged fields near the tip when using λ = 1064 nm, show that the same waveguide can be reused for light having longer wavelengths. Hence, it is also possible to use the optical trapping light for high NA focusing.

5.5 Novel means of optical manipulation

A waveguide's ability to change light's direction has another useful effect. Since changes in direction correspond to changes in momentum, waveguiding can play a role on the particle's resulting motion. Again, with the design freedom offered by DLW or other microfabrication processes, novel ways of micromanipulation can result from specifically tailored light deflectors. Since the 70s [15] demonstrations of optical micromanipulation are predated with the tweezing of dielectric microspheres. Since the customization of microscopic objects is a relatively new paradigm, the development in optical micromanipulation usually focused on the light shaping part, which was in turn catalyzed by improvements in SLM technology. The easier accessibility and relative ease of analysis of microspheres also made themselves good candidates for such experiments.

Nonetheless, interesting dynamics have been observed with light's interaction with more complex or asymmetric structures. For example, birefringent material can be spinned by certain optical modes [106,107]. The direct sculpting of micro structures, however, offers far more control leading to microscopic engineering analogues of machines designed for aero or fluid dynamics. Examples include microfabricated optically driven propellers, wings and sailboats [21,51,91]. A

recent review of microscopic light matter interactions that describes the possibilities of optimizing beam properties and microstructure geometries is given in [108].

Unlike fluids, however, light can be shaped directly, offering far more flexibility by allowing arbitrary energy distributions that do not have to spread or level out within a container. Other distinguishing properties of light such as phase and polarization also have effects when in interacting with matter. Examples include the transfer of spin and orbital angular momentum from light with helical phase or circular polarization respectively [107,109,110].

Here we demonstrate that a translating force can be exerted on a bent waveguide, even when using only a static optical distribution. Although the free standing waveguides were originally designed for active optical manipulation via dynamic beam shaping techniques, we switch to "unmanned" manipulation by allowing them to move along pre-defined static optical distributions. An awareness of such forces also allows the user to counterbalance this "recoil" by adjusting the traps on the microtool's handles.

5.5.1 Calculating fields and forces on bent waveguides

In a similar manner as the previous waveguide calculations, the fields are first obtained via FDTD. After obtaining steady state fields, the time-averaged optical force on the bent waveguide is obtained by integrating the time-averaged Maxwell's stress tensor over a closed surface surrounding the waveguide [111,112]:

$$F = \int_S \langle \tilde{T}(r,t) \rangle \cdot dS \tag{5.7}$$

where the differential area element d**S** is directed along the outward normal and $\tilde{T}$ is the Maxwell stress tensor given by

$$\tilde{T}_{ij}(r,t) = \varepsilon\varepsilon_0 E_i(r,t)E_j(r,t) + \mu\mu_0 H_i(r,t)H_j(r,t) - \frac{1}{2}[\varepsilon\varepsilon_0 |E(r,t)|^2 + \mu\mu_0 |H(r,t)|^2]\delta_{ij} \tag{5.8}$$

In a similar way that Gauss's law detects charges within a volume the stress tensor integral "detects" a scattering object by measuring field distortions in the enclosed volume. For verification, we also checked that there are no forces when the integration surrounds a region wherein there is no particle.

Again, for computational convenience and with the expected geometry of the resulting motion, we perform 2D simulations. We rotated the coordinate axis to correspond with our experiments, i.e. incident light propagates along z and x is the horizontal of the side view camera. Thus we used the components E_y, H_x and H_z. The structure and fields are then assumed to be invariant along y in the simulation. Since we are only interested in the region where light bends, and since the calculation requires additional quantities, i.e. the stress tensors, the FDTD simulations were performed on 512 × 512 grids which correspond to about 20x20μm^2 given a discretization of Δ = 40nm. The incident beam (vacuum wavelength λ_0 = 1070 nm) exhibits a Gaussian transverse profile (beam waist w_0 = 2.0 μm) along the x-axis and propagates through water (n = 1.33) towards the +z-axis with linear polarization along the y-axis (which can subsequently create TE–polarized modes in the waveguide). In this case, only E_y, H_x, and H_z are nonzero. Hence the components of the stress tensor reduce to:

$$\tilde{T}_{xx} = -\varepsilon\varepsilon_0 \frac{1}{2} E_y^2 + \mu\mu_0 \frac{1}{2}(H_x^2 - H_z^2)$$

$$\tilde{T}_{zz} = -\varepsilon\varepsilon_0 \frac{1}{2} E_y^2 + \mu\mu_0 \frac{1}{2}(H_z^2 - H_x^2) \tag{5.9}$$

$$\tilde{T}_{xz} = \tilde{T}_{zx} = \mu\mu_0 H_x H_z$$

The surface integral for the force, $\boldsymbol{F}$, is then calculated along normals of a 2D path along a box that bounds the whole microstructure (dashed lines in Figures 5.7-9). We also obtained comparable force results when using an alternative approach comparable to the divergence form of the integral for $\boldsymbol{F}$. The force on each unit cell of the simulation grid is calculated, and then summed within a defined mask that is closely covers the object's area.

The simulation results for the case of light coupling through a bent, step-index dielectric waveguide (n = 1.6, input diameter 1 μm) are shown in Fig. 5.7. Figures 5.7(a), (c), and (d) show snapshots of the electric and magnetic field components,

while Fig. 5.7(b) shows the time-averaged intensity of the light propagation after 1200 time steps. Evaluating the force using the stress tensor along the box illustrated in Fig. 5.7(b) yields a net force, $\boldsymbol{F} = -36.14\hat{x} + 37.87\hat{z}$ for the TE-polarized case presented here (we obtained similar results from TM-polarized simulations). Since absolute quantities such as mass and optical power are not considered, the dimensionless forces from our calculations are understood to be taken on an arbitrary scale, which is used consistently throughout the simulations. Comparisons with calculations on other typical geometries were thus performed to get relative force measurements.

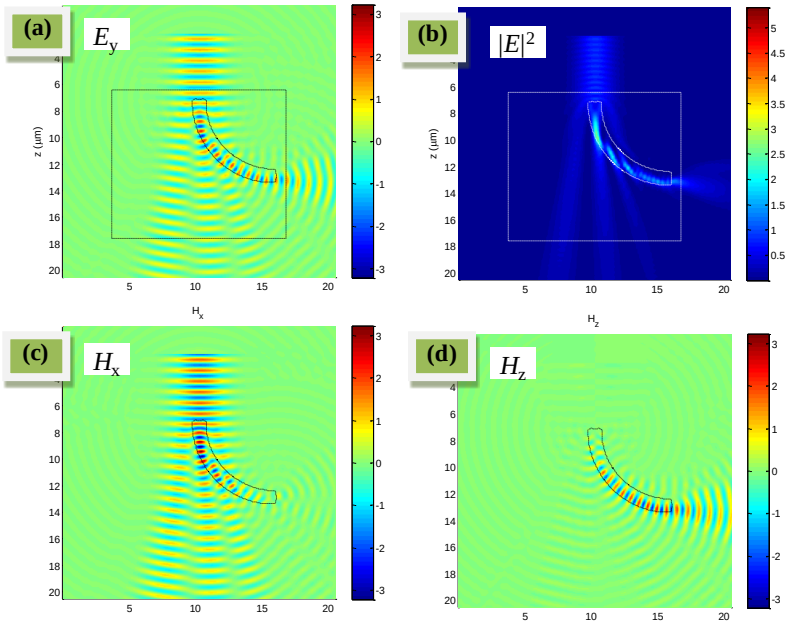

Figure 5.7. Simulated propagation of light through a bent waveguide for calculating the Maxwell stress tensor and the optical force: (a) snapshot of the E-field's *y*-component, E_y; (b) time-averaged intensity, $|E|^2$; (c) snapshot of the *H*-field's *x*-component, H_y; (d) snapshot of the *H*-field's *z*-component, H_z. (λ_0 = 1070 nm, n_{bead} = 1.6, $n_{surrounding}$ = 1.33). (Figure adapted from [50]).

5.5.2 Comparing with reference structures

When relating to optical trapping, a particular quantity used for benchmarks is the efficiency factor Q. For a ray of light with power, P, in a medium with index n_m and with c being the speed of light, Q denotes the fraction of momentum transferred by the ray to the particle.

$$F = Q\frac{n_m P}{c} \tag{5.10}$$

Looking at the other quantities, we see that Q encapsulates the geometric contributions in the resulting force. Unfortunately, except for the resulting force, our FDTD approach does not directly use these ray-optics quantities. Hence, we quantify improvements by comparing with FDTD simulations of typical scattering geometries -- a dielectric bead and an angled mirror. By setting the same incident power and source in the simulations we can obtain a dimensionless relative efficiency factor:

$$Q_{rel} = \frac{Q_{WG}}{Q_{ref}} = \frac{F_{WG}}{|F_{ref}|} \tag{5.11}$$

Here, Q_{WG} and Q_{ref} are the Q factors for the bent waveguide and dielectric bead respectively, which are both unknown. F_{WG} and F_{ref} are the respective forces on the waveguide and bead that are obtained with our calculations. Thus, the relative value obtained gives an indication of the how much the efficiency factor improves compared to the circular dielectric microsphere.

5.5.2.1 **Dielectric bead**

Since the simulations are only 2D, the dielectric bead is represented by a cylinder is used instead of sphere. In any case, we expect that the forces along y would cancel due to symmetry. Having established a means for comparisons, we performed similar 2D simulations using a circular dielectric microbead (n = 1.6 matching SU8) as a reference object, whose diameter (d_{ref} = 1 μm) matches the input diameter of the waveguide to intercept an equal portion of the incident light. The simulation results for the reference bead are presented in Fig. 5.8, which shows the time-averaged intensity pattern and a snapshot of the transverse electric field component. The reference force obtained is practically a downward force $|F_{\text{ref}}|$ =

3.96. The quiver plot overlay shows forces evaluated within 15×15 grid units ($0.6\times0.6\mu m^2$).

Comparing the bead and bent waveguide results, we get a relative efficiency factors $Q_{rel,X}$ = 9.12 and $Q_{rel,Z}$ = 9.56 along the transverse and longitudinal directions, respectively, where the axial and transverse directions are described with respect to the incident illumination. Using the net force, we get a net efficiency factor $Q_{rel,net}$ = 13.21, which represents an order-of-magnitude efficiency improvement when compared to the circular dielectric microbead.

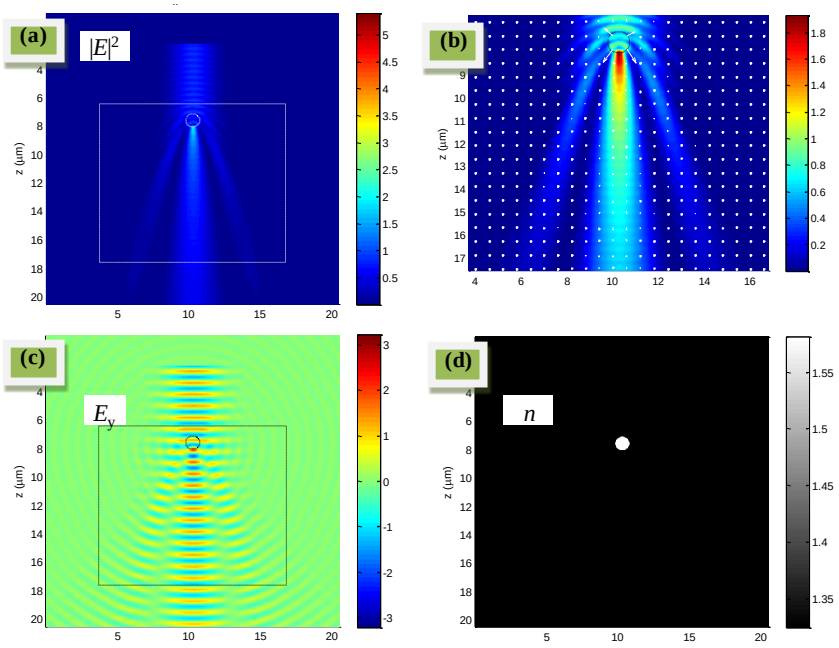

Figure 5.8. Simulated scattering off a circular dielectric microbead for calculating the Maxwell stress tensor and the optical force: (a) time-averaged intensity, $|E|^2$; (b) zoom-in on the bounding box with quiver plot overlay depicting the calculated force sampled from 15×15 unit cells (c) snapshot of the E-field's *y*-component, E_y ; (d) refractive index distribution. (λ_0 = 1070 nm, n_{bead} = 1.6, $n_{surrounding}$ = 1.33). (Figure adapted from [50]).

These results show that controlling light deflection by engineering the microstructure achieves an optical force exceeding that achieved when using simple partial reflective/refractive light deflection in a microbead.

5.5.2.2 **Angled mirror (best case scenario)**

To gauge how much more we would get with a more optimized structure for orthogonal light deflection, we also simulated the optical force that acts on a perfectly reflecting mirror angled at 45º to deflect light orthogonally. A perfect electric conductor (PEC) was simulated by setting the electric field to zero at the mirror's location. The simulation results, presented in Fig. 5.9, yield a net force, $\boldsymbol{F} = -86.98\hat{x} + 85.62\hat{z}$. The corresponding transverse, axial, and net relative efficiency factors are $Q_{\mathrm{rel},x}$ = 21.95, $Q_{\mathrm{rel},Z}$ = 21.61, $Q_{\mathrm{rel},net}$ = 30.8, respectively. The same order of magnitude efficiency improvement, relative to a circular microbead, achieved for both the waveguide and the perfect mirror indicates that, indeed, the waveguide serves as a good example of optimizing the optical force using structures designed with specifications for light deflections. Moreover, the about twice higher efficiency achieved for the perfect mirror shows that there is still some room for optimizing the deflecting structure (e.g., minimizing the coupling losses evident in the simulated propagation in Fig. 5.7).

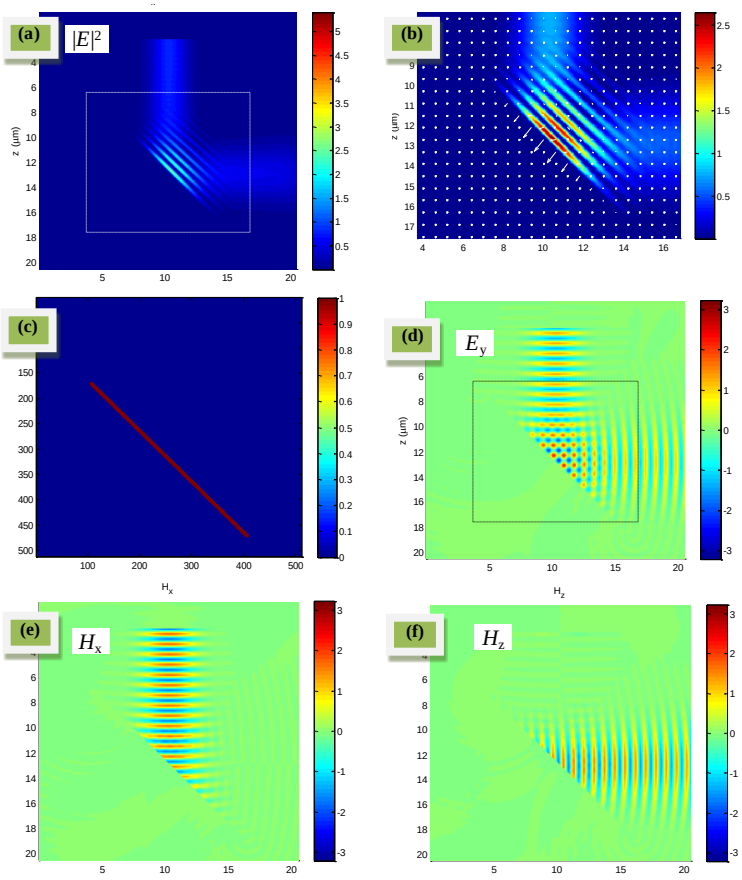

Figure 5.9. Simulated reflection off a perfect mirror for calculating the Maxwell stress tensor and the optical force. (a) time-averaged intensity, $|E|^2$; (b) zoom-in on the bounding box with quiver plot overlay depicting the calculated force on each unit cell of the simulation grid (c) location of mirror (λ_0 = 1070 nm, $n_{surrounding}$ = 1.33) (d)–(f) snapshots of the fields E_y, H_x, and H_z. (Figure adapted from [50]).

5.6 Experiments

The following sections will describe our proof-of-principle experiments to supplement our numerical findings. Microstructures fabricated with built-in waveguides are manipulated in the BWS. The first experiment demonstrates waveguiding through optically manipulated microtools. The second experiment demonstrates how guided light deflections in the waveguide generate optical forces that are enough to drive them along pre-defined light paths. For an experimental

demonstration of manipulation via reflection from angled mirrors which was also simulated, the reader is referred to the work of Búzás et al [91].

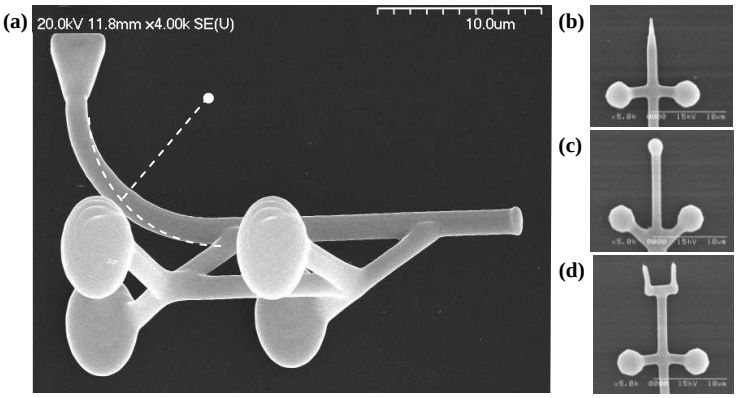

Figure 5.10. SEM images of representative two-photon polymerized structures: (a) A bent waveguide (bending radius R~8 μm; width ~ 1.5 μm) sitting atop a supporting structure having spheroidal handles for optical trapping; the waveguide is connected via reverse-angled rods for minimal light-coupling loss the support structure; (b) – (d) Some tip structures that can be fabricated. (Figure adapted from [25]).

5.6.1 2PP fabrication of microtools

The microtools were fabricated using the two-photon microfabrication system described in [113]. The procedure includes a two-minute soft bake of spin-coated photoresist layer (SU8 2007, Microchem) at 95°C on a hot plate, followed by scanning focused laser illumination and 10 minute post-illumination bake (also at 95°C). Microstructures were formed by scanning tightly focused ultrashort pulses from a Ti:sapphire laser (λ=796μm, 100 fs pulses, 80 MHz repetition rate, 3 mW average power) in the photoresist. The laser pulses were focused by an oil-immersion microscope objective (100× Zeiss Achroplan, 1.25NA objective; DF-type immersion oil Cargille Laboratories, formula code 1261, n=1.515). The focal spot was scanned relative to the resin at speeds of 10μm/s for the spheres and 5μm/s for the connecting rods and tip to solidify voxels with minimum transverse and axial feature sizes of 0.4 ± 0.1μm in transverse and 1 ± 0.1μm in longitudinal directions, respectively.

Representative SEM images of the fabricated structures are shown in Fig. 5.10. Figs. 5.10(b-d) illustrate the variety of tip profiles that can be fabricated using the

2PP system. We have iterated through several design/fabrication cycles, where we used optical trapping/waveguiding test results to improve later designs. The SEM image shown in Fig. 5.10(a) shows one of the later designs, where a bent waveguide sits atop a supporting structure that contains spheroidal optical trapping handles. Here, the use of two connecting rods to the waveguide (as opposed to 4 rods for the structures in Fig. 5.10(b)) minimizes the deformations along the waveguide that can lead to leakage. The reversed angled connecting rods also minimize light coupling out through the rods as opposed to forward-angled connecting rods (Fig. 5.10(c)).

5.6.2 Sample preparation

After developing and harvesting, the microstructures were stored in solvent containing water mixed with 0.5% surfactant (Tween 20) and 0.05% azide. The surfactant prevents the microstructures from sticking to other structures and to the sample chamber while the azide prevents microbial growth during storage. Before using the microstructures, the sample is centrifuged to let the structures settle to the bottom and then briefly sonicated to dislodge any sticking structures for easier collection. The collected structures are first mixed with a fluorescent calcium indicator (10μm calcium orange diluted in ethanol) to enable the visualization of the light propagation. In some cases, the structures are mixed with a dilute solution of dyed microspheres. Upon loading the samples into a cytometry cell (Hellma 131.050, 250μm × 250μm inner cross-sections, 1.6 μL volume), the cells were sealed to reduce evaporation, allowing repeated experiments over several days.

5.6.3 Optical micromanipulation

The experiments were carried out in the Biophotonics Worksation described in Chapter 3. Figure 5.11 shows a microtool optically manipulated to poke a relatively large bubble (~80μm). This demonstrates the potential for pin-point targeting specific areas in cells that would not have been accessible without affecting other areas. Figure 5.12 shows the simultaneous optical trapping and manipulation of two microstructures. This is useful for applying opposing mechanical forces on a cell to keep it stable while doing micro experiments.

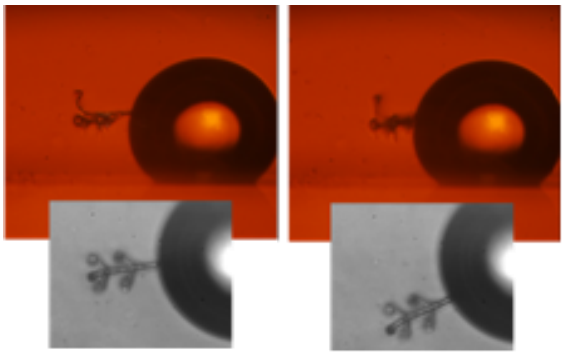

Figure 5.11. Experimental snapshots showing a microtool being optically manipulated around a relatively large bubble (~80μm). The top row shows the images recorded from the side view and the bottom row shows images recorded through the top view. (Figure adapted from [25]).

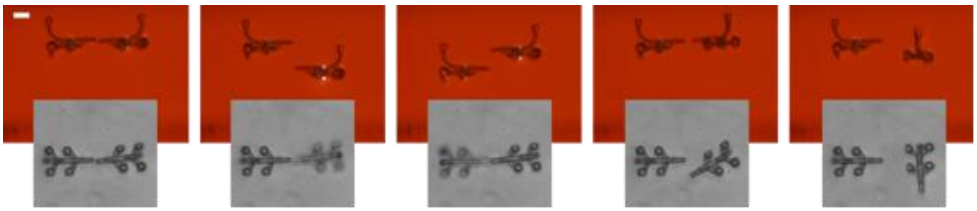

Figure 5.12, Snapshots of simultaneous optical manipulation of two microstructure. The top row shows the images recorded from the side view and the bottom row shows images recorded through the top view. (Figure adapted from [25]).

5.6.4 Guiding and focusing light through tapered tips

To test whether the fabricated structures can act as waveguides, we trapped them with CP beams through their spherical handles, rotated them to point towards the side view microscope, and then held them in place while an external vertical beam was directed towards the input end of the waveguide (Fig. 5.13). Figure 5.13(a) shows images from the side view microscope, which show light of different wavelengths (532nm and 1064nm) emerging from the subwavelength tip. Filtering the green light reveals that the coupled light emerges from the tip with sufficient intensity to excite fluorescence in the treated surrounding medium (Fig. 5.13(c)).

To experimentally verify the numerically simulated results, we rotated the trapped structures so the tip points sideways. The surrounding fluorescent medium enabled us to visualize the light propagation, as shown by the side-view image in Fig.

5.13(b). The propagation qualitatively agrees with the features observed in the simulations. For example, the light emerging from the subwavelength tip would, expectedly, have a narrower width than rather broad incoming beam. We can also see the losses near the bend. Figure 5.13(e) illustrates the possibility for on-the-fly modification of the emerging light by positioning other optically trapped microscopic optical elements at the tip. Here we trapped a microsphere and used it as a microlens to focus the divergent light emerging from the tip.

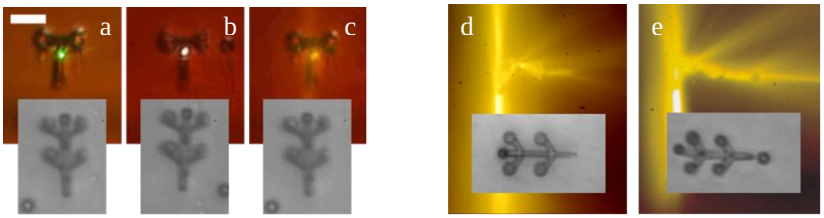

Figure 5.13. Guiding light through waveguides held by stationary optical traps. Snapshots from side-view microscopy during light coupling experiments through an optically trapped structure showing (a) λ=532nm; (b) λ=1064nm; (c) fluorescence at 532nm excitation as the waveguide points towards the microscope. (d) and (e): Fluorescence images at 532nm excitation when the waveguide is reoriented to visualize the beam propagation. Light emerging from the tip exhibits a diverging profile, (d), which can be focused by using an optically trapped bead as lens, (e). (scalebar:10μm). (Figure adapted from [25]).

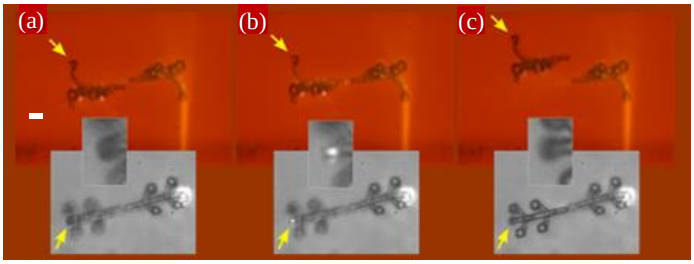

Figure 5.14. Simultaneously manipulated WOWs showing light entering one tool and going through another tool which captures the light from the output of the first tool. No light is coupled while the second tool's tip is not aligned with the first as in (a) and (c). Light can be seen at the "input" tip of the second tool when it is aligned with the first tool (b). The second tool thus effectively functions as a light sensor. (scalebar:10μm). (Figure adapted from [25]).

The light guiding abilities of WOWs are, perhaps, best demonstrated in Fig. 5.14 wherein two of them are simultaneously used to show light coupled through one tool and then captured through another which sends the output to the camera (Fig.

5.14(b)). The second tool effectively acts as a light sensor demonstrating potential use for high resolution microscopy or microscopic endoscopy.

5.6.5 Moving waveguides along static optical distributions

To illustrate some of the features predicted by the theoretical FDTD force analysis, we reused some of the bent waveguides fabricated for the WOW demonstrations. To sustain the motion resulting from the light deflection a static line trap was drawn such that it follows the anticipated motion of the microtool.

Figure 5.15 shows the configuration of the microtool, line traps and camera used for the snapshots shown in Figure 5.16. These snapshots were extracted from video recordings of optical manipulation experiments studying the structure's motion due to the optical force on its waveguide. The results show that the line trap effectively defines a "light track" where the microstructure glides along while it is simultaneously pushed downward against the bottom of the sample chamber. The regular arrangement of equally time-spaced snapshots enables us to plot the structure's position vs. time by using the structure's tip as data points for the plot. The structure's position vs. time plot in Fig. 5.16(a) shows that it moves with fairly constant velocity until the other tip reaches the light track and gets illuminated. The constant velocity suggests that the optical force is matched by dissipative forces (in this case due to fluid drag and friction with the bottom surface of the sample chamber).

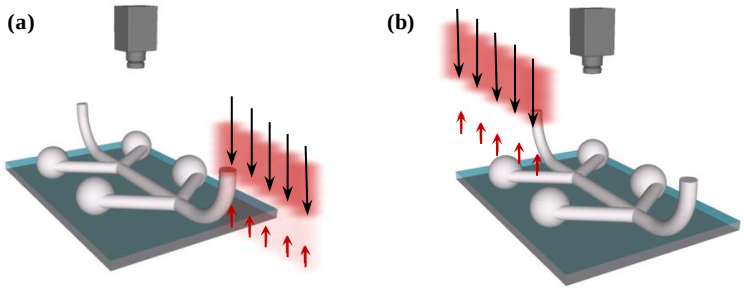

Figure 5.15. Configuration of the microtool, line traps and camera used for the snapshots shown in **Fig 5.16**. A line trap is drawn to maintain guided input light as the microtool moves. In (a) light first goes through the front input facet, while in (b), light first goes through the rear input facet. (Figure adapted from [50]).

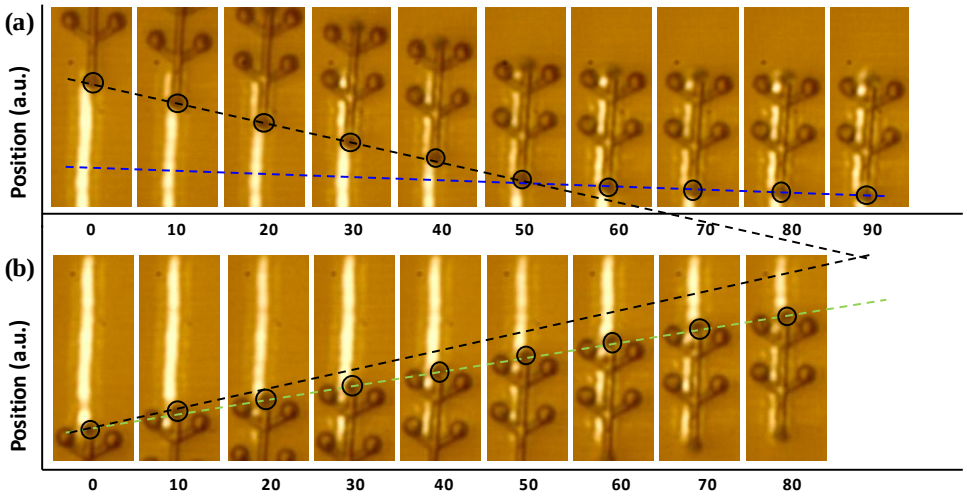

Figure 5.16. Motion of a structure due to the optical force from guided light deflection. The horizontal arrangement of the snapshots, taken at equal time intervals using the top-view microscope, enables using the structure's tip as the position data point at each observation time. (a) Plot of the structure's position vs. time with light first entering one tip. The trendlines indicate that the structure moves with nearly constant velocity when light enters only one tip of the waveguide (frames 0 to 50). The movement pulls the other tip into the line trap; the structure subsequently moves with lower velocity when light enters both tips (frames 60 to 90); (b) Plot of the structure's position vs. time with light first entering the other tip. The green trendline indicates that, with light being guided in the opposite direction, the structure also moves with a nearly constant velocity. The lower slope of the green line compared to the black line indicates that it moves slower compared to (a). (Figure adapted from [50]).

Snapshots of the bent waveguide microstructure moving due to the optical force from guided light deflection are shown in Figure 5.16(b). The structure's position vs. time trendlines indicate that the structure moves with nearly constant velocity when light enters only one tip of the waveguide (frames 0 to 50). Due to opposing forces as the movement pulls the other input tip into the line trap, the structure subsequently moves with lower velocity when light enters both input tips (frames 60 to 90). The green trendline in Fig. 5.16(b) indicates that, with light being guided in the opposite direction, the structure also moves with a nearly constant velocity. However, the lower slope of the green line compared to the black line indicates that it moves slower compared to Fig. 5.16(a). The lowered velocity when starting with the opposite tip (Fig. 5.16(b)) may be a result of the asymmetry in the guided

light's propagation which in turn could be due to the asymmetric geometry of the front and back handles (legs) or asymmetry due to fabrication imperfections.

5.7 Conclusions

We have studied the use of microtools as a means of extending the capabilities of optical trapping experiments and studied alternative modes of optical micromanipulation that rely on the geometry of the microtool instead of the direct motion of optical traps. The engineering of fabricated microtools offer structure–mediated micro to nano coupling that allows nano scale experiments through micro scale optical trapping systems. With dynamic optical trapping and micromanipulation, microtools enable the dynamic routing and targeted delivery of optical energy. Using a bent waveguide, we have shown some of the features and promising potential of shaping objects to create controlled light deflections and, thereby, achieve desired optical forces. The results display an interesting optical manipulation modality where static illumination exerts a position-independent optical force, along one dimension, in contrast to harmonic potential regimes in conventional optical trapping.

This work exploits a convergence of various contemporary photonic technologies ranging from light-based fabrication and mechanical manipulation to optical guiding for light delivery and probing. Thus, it is fertile ground for interfacing with other photonic technologies for enabling novel functionalities.

5.8 Outlook

So far the microtools that we had been manipulating with the BWS are based on proof-of-principle quick engineered designs that can be fabricated straightforwardly and were made with a single material. There is plenty of room for extensive quantitative analysis or computational optimization [51,114] to take advantage of both beam shaping and object shaping [108]. On the other hand, advanced microfabrication techniques, chemical processes or even on-the-fly optical microassembly during experiments can allow composite microtools that take advantage of different material properties of its parts. For example, fluorescent material [115] or gold nanoparticles [116] had been added to microtools using sol-gel or protein based chemical binders. We also present initial progress on a

microassembly approach to build a composite lens microtool for high resolution microscopy [117].

5.8.1 Geometric optimization: sculpting the object

Just as we have shown through FDTD based force calculations how bent waveguides can demonstrate new ways of optical manipulation, there still remains many possibilities that can be discovered faster if optical experiments could be computationally tried out first. For example, a modified open source ray tracing software (POV-Ray), normally used for photorealistic rendering (examples include some figures in this thesis), was used to simulate the "optical lift" of a half cylinder, moving perpendicular to the laser illumination [51] (Fig. 5.17). The geometrical possibilities achievable by 2PP can benefit further from a variety of computational tools for optimization. Advances in computational modeling as well as computing technology allow researchers to optimize the structures in a virtual environment prior to fabrication and testing in real experiments. Such tools can include evolutionary computing, topology optimization, or simply systematic manual trial and error like what we have done in our work. In a nutshell, evolutionary computing simulates survival of the fittest by benchmarking a population of possible designs, getting rid of the poor designs, then combining the better ones then iterating the selection process [118]. Topology optimization, on the other hand, uses sets of iterated differential equations to gradually determine the optimal topology for a given engineering task or design. These design tools have already been successfully applied in a plurality of engineering disciplines by e.g. optimizing the distribution of material for a wide span of situations from the load-bearing structure of an airplane wing [119] and down to the design of tiny micro-robotic grippers [120]. Calculated results can often lead to surprisingly new designs of known and existing structures, hence it is important to consider practical constraints of the fabrication and micromanipulation. We anticipate that scientists and nano-engineers can utilize these emerging 3D computational and engineering schemes to design and sculpt the next generation of top-tuned light–driven micromachines [114].

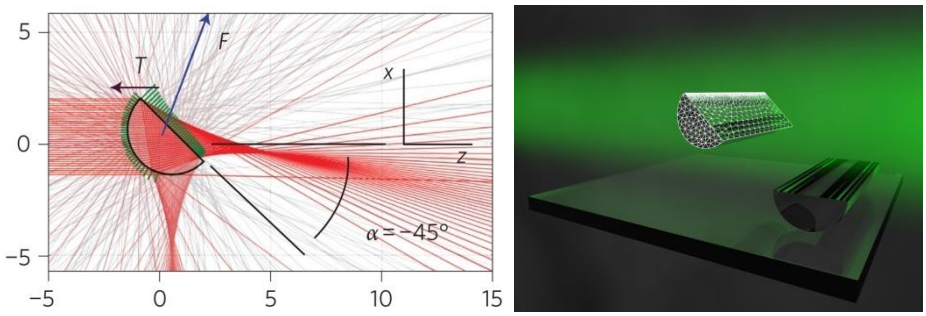

Figure 5.17. The conceptualized use of computational methods such as topology optimization for optimizing light matter interaction in microfabricated structures as envisioned in [114]. (Figure 5. 17(a) adapted from [51]).

5.8.2 Holographic optical tweezing of micro optical magnifiers

Although a major motivation in the development of microtools is the kinematic limitations of commonly trapped microspheres, clever ways of using such microspheres are recently finding new applications [121,122]. For examples several microspheres can be trapped simultaneously to clamp a cell and act similarly to our microtools' optical handles [123]. Furthermore, instead of just moving them around, light can be focused through these spheres, effectively using them as lenses. Unlike 2pp fabricated structures, microspheres, typically formed via surface tension, are near perfect spheres. There is also a greater variety of microsphere materials that can have higher refractive indices compared to those that can be used for 2pp [124]. Hence, by scaling things down the common uses of lenses, focusing light [122] and imaging objects [121] can be done at higher resolutions. Our initial experiments with WOWs for example showed focusing of green light through an optically trapped microsphere brought to the WOW's tip (Fig. 5.13(e)).

For imaging applications, trapping the microsphere lens may not always be a convenient option as it may be undesirable to get radiation into the samples, i.e. for fragile biological specimens. It can get even worse if the trapping light gets focused by the microsphere into the sample. To address these potential problems, we again apply the tool and handle paradigm to isolate the trapping light from the lens. Therefore, we have recently been developing microsphere holders which serve as maneuverable magnifying lens handles (Fig. 5.18).

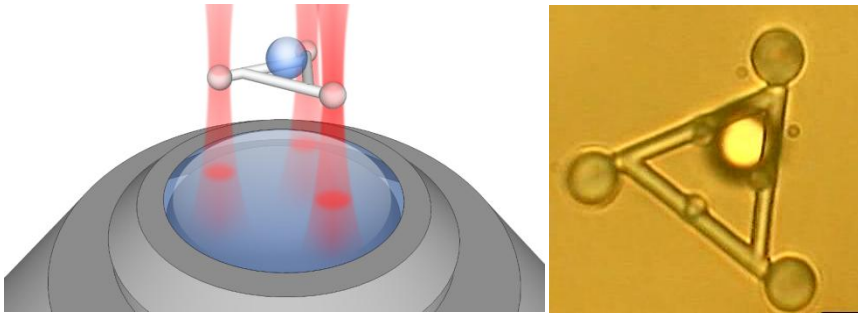

Figure 5.18. A microsphere is supported by an optically actuated "tripod" supporting structure (a). This allows the microsphere to be moved around an imaged sample, even if the sphere itself is not optically trapped. Microscope image of the triangular lens supporting structure and a 6μm bead (off focus) (b).

These micro optical magnifiers (MOM) can be micro-assembled on the fly using a dynamic multi-trap setup. Initial demonstrations of these MOMs were performed with HOTs at the Biological Research Centre at the University of Szeged where they were also fabricated. Although the axial manipulation range in HOT setups is limited, their typical use of high NA optics that results in higher image resolutions, can be an extra advantage for in manipulating MOMs. Once the MOM is assembled, the demand of axial control is also less since imaged samples normally lie at the top or at the bottom surface of the sample chamber.

6 Conclusions and outlook

Several applications and improvements of the BioPhotonics Workstation have been presented so far. Chapters 3 and 4 proposed the use of dynamic axial stabilization and mGPC as a workaround for the stability tradeoffs when using of low NA optics to extend the axial manipulation range. This extended manipulation range, combined with fast beam shaping methods such as GPC or mGPC, in turn, has allowed real time 3D applications such as that demonstrated with microtools. Research with microtools and other structure mediated applications enabled by light based manipulation and light based microfabrication therefore offer novel ways of approaching biological experiments. Furthermore, mGPC, which has been shown to be robust enough to operate on more accessible consumer display projectors, would also make the versatile applications of beam shaping available to more laboratories.

Being an enabling platform, there is still a lot of room for improvements and new experiments to be done in the BWS, in a similar manner that computers are constantly changing and finding new applications. For example, software development can help in catching up with the latest technologies in intuitive computer interfaces such as touchscreens, motion detection, or haptic devices. With the limited time and laboratory resources, a BWS operated with mGPC has, so far, not yet been fully implemented. Nonetheless, there has been initial progress on a cell sorter that takes advantage of mGPC's higher intensities for catapulting objects.

This chapter would therefore briefly describe some of the smaller works towards future goals. Experiments pursued with collaborations that showcase the BWS's capabilities in biophotonics experiments are also presented here. These experiments include the use of a static GPC setup to increase the light throughput in the BWS through more efficient SLM illumination [27] and modified versions of the BWS for biophotonics applications such as pH mapping [70] and sorting of cells [29].

6.1 Gauss GPC: getting more light into spatial light modulators

Achieving high photon efficiency is always important when implementing practical optical systems, including our BWS. Hence, it is important to use light efficiently wherever possible. This is not just limited to the shaping of optical distributions that go into the sample, that are addressed through different beam shaping techniques (Chapter 2). It is easily overlooked, but equally important to get as much light into the spatial light modulators, regardless of what beam shaping technique is implemented.

It is common for conventional laser modes to have a Gaussian, circular symmetric distribution while SLMs are rectangular. This shape mismatch between typical laser profiles and pixel addressed SLMs is usually overshadowed by the main experiment. Hence, losses or inefficiencies are introduced when the input laser is magnified to fill the whole SLM surface or if the whole SLM is not utilized when the laser only illuminates a circular portion of it. Furthermore, when minimizing input truncation, the typical Gaussian profile prevents even illumination of the SLM.

To address this mismatch, we implement GPC beam shaping with fabricated phase plates to efficiently convert a Gaussian amplitude distribution into a rectangle with a more uniform intensity, optimally illuminating an SLM [8,80,125]. The GPC based beam profile converter is implemented through patterned phase plates and a phase contrast filter fabricated via wet etching Pyrex, similar to the mGPC filters discussed in Chapter 4. Experimentally, we have demonstrated the conversion from a Gaussian to a rectangular distribution with 75% efficiency [27].

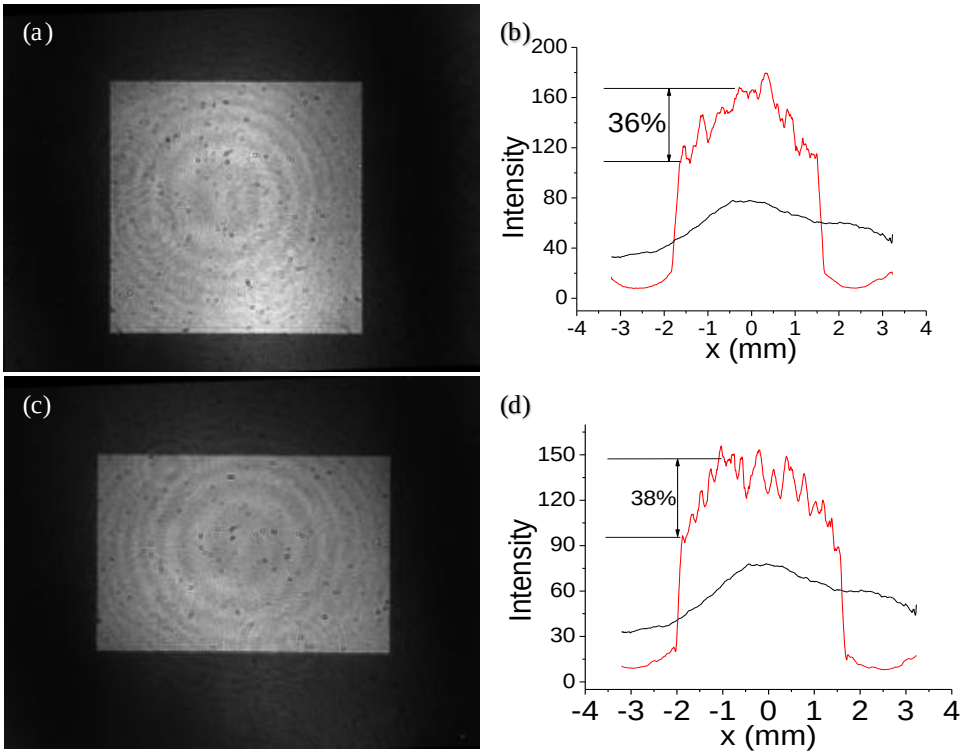

Figure 6.1. Experimentally obtained square and rectangular intensity images (a & c) and their corresponding line scans (b & d). The red line indicates the horizontal scan through the reshaped profile and the black trace is that of the input Gaussian. (Figures adapted from [27]).

The flat phase of GPC shaped light is also an advantage when comparing with commercial engineered diffusers (Thorlabs & RP Photonics). A similar proprietary product, the πShaper, can also convert Gaussian light to a tophat, but loses around 50% of the light and costs more. Furthermore, the benefits of an ideally illuminated SLM are not limited to 4*f* based beam shaping systems such as GPC and mGPC. Evenly illuminating as much area as possible on the SLM allows more high spatial frequency contributions in 2*f* holographic beam shaping setups, which in turn leads to sharper focusing.

6.2 Controlling temperature while characterizing trapped samples

Heat accumulation is a common problem in many machines. Experimental setups and samples are not an exception. Experiments typically contain electronics and some components that may be absorbing light. In a setup containing biological samples, such effects cannot be overlooked, since heat can have effects in the health or viability of living samples. Therefore it is important to assess how these samples are responding to such stressors using characterization techniques that monitor biochemical activity. Such characterization, however, gets complicated with heat effects like sample drift due to thermally induced fluid motion or even damage to immersion microscope objectives as they are in contact with the sample.

The large working distance of the BWS solves this problem by allotting space for a temperature control and monitoring extension while trapping the cells being characterized. We monitor of yeast's internal pH under varying temperature conditions using a BWS setup modified to enable fluorescence imaging. A yeast cell was fluorescence imaged and kept stable by an optical trap while subjected to heat treatment of up to 70°C.

A schematic of the modified BWS setup is shown in Fig. 6.2. A trapping wavelength of 1070nm and power of 5mW was used for trapping. A monochromator is used as the excitation light source for fluorescence and is introduced to the sample via dichroic filters. When required for imaging, such as when viewing the trapped samples, white light is introduced into the sample via an automated shutter. For feedback, the temperature in the sample is controlled with a Peltier element and monitored through thermocouple wires.

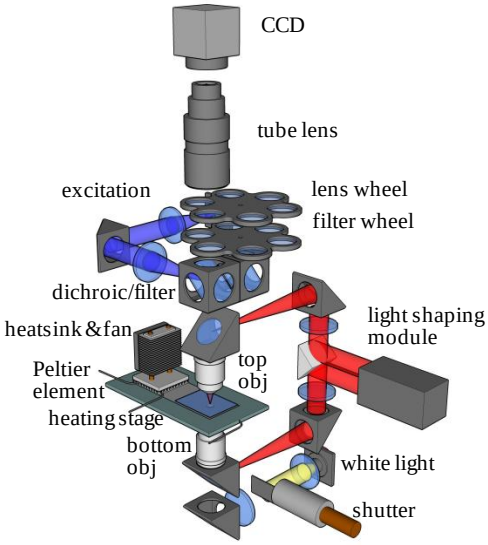

Figure 6.2. The BioPhotonics workstation modified to support a fluorescence setup and a heating stage. The same objectives used for counter-propagating beam traps (red) are also used for fluorescence imaging. The heating stage lies between the opposing objectives. Excitation light (blue) goes through the top objective through the dichroic mirror and passes through filters for imaging. White light (yellow) goes through the bottom objective for bright field illumination. (Figure adapted from [70]).

Using the modified BWS, the internal pH distribution of the cell was mapped via fluorescence ratio imaging at 435 nm and 485 nm, with 5-(and-6)-carboxyfluorescein diacetate, succinimidyl ester (CFDA-SE). Membrane permeability was assessed with the fluorescence from propidium iodide (Pi). Results in Fig. 6.3 show enough spatial resolution within the cell while addressing heating problems like drift due to thermal expansion and possible damage to immersion objectives.

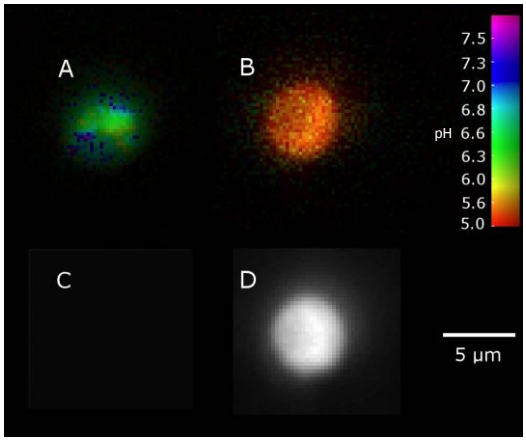

Figure 6.3. Optically trapped single *S. cerevisiae* cell in YPG medium (pH 5.6). All four images are of the same cell. A and B show the spatial pH distribution at 30°C and 70°C, respectively. C and D are PI images at 30°C and 70°C, respectively. (Figure adapted from [70]).

6.3 Cell sorting using machine vision on a reduced BWS

A special case of optical micromanipulation that is useful in medical diagnostics would be the isolation of cells. Samples used in microscopy or micromanipulation usually come in large quantities that it doesn't require hours to locate them under the microscope. But it is often the rare ones, or the defective one-in-a-million that are of most interest in research. As typically the case, especially in apparently healthy people, there are far less sick cells among millions of normal healthy cells. Combined with image processing for the automated detection of target cells, optical forces can be used to move such cells from one fluid channel to another.

In Chapter 3, we showed how software based solutions like machine vision can supplement experimental setups such as stabilizing the axial positions of trapped particles. Again, we propose utilizing machine vision for developing an active cell sorter. The sorter is based on a reduced single beam channel version of the BWS since detected cells only need to be catapulted upward. As the sorting motion is along the axial direction, parallel sorting would be achieved by encoding multiple CP beams on the transverse plane.

6.3.1 Cell sorting

Cell sorting has an increasing importance in biological research and medical applications. For example, the identification and isolation of a few specific indicator cells among millions of others can be used as an early diagnostics tool. Isolating the disease carrying or abnormal cells also speed up the development of drugs by allowing specificity and localization in cell-drug interactions.

Most cell sorting systems today are based on flow cytometers capable of high-speed whole-cell fluorescence measurements, which can be expanded to fluorescence activated cell sorters (FACS) [126]. With FACS machines costing up to $200,000 [127], there has lately been a resurging interest in microscopy-based cytometry systems [128] that can offer the added possibility of non-invasive label-free approaches. This calls for alternative techniques not only for cell measurements [129], but also for cell sorting mechanisms, e.g., based on optical trapping and manipulation [130] that can utilize economical and compact beam modulation approaches [131].

6.3.2 The Cell BOCS

Unlike the complex manipulation of microtools previously discussed, cell sorting trajectories in our proposed scheme are much simpler, tending to have a general (upward) direction. This allows us to trim down the BWS. This reduction has resulted into the Bio-Optofluidic Cell Sorter (BOCS). The BOCS would then utilize machine vision to identify particles for subsequent sorting. To perform sorting, visual features on cell samples such as morphology, size or color are used as a basis of discrimination. Contrast can also be improved using advanced illumination or imaging methods. For example, adapting GPC for phase contrast microscopy could further highlight cells against the background, and make detection more robust. A minimal footprint allows the BOCS to operate as a table top device (Fig. 6.6(a)). Hence, it does not require as much space as a conventional FACS system does. Furthermore, compared to a similar full blown BWS, twice the laser power can be utilized since only an upward beam is needed

Cells in a flow chamber only need to be pushed to a defined height after being detected (Fig. 6.6(b)). The same microscope objective used for catapulting cells can also used for imaging and machine vision. Cells or particles that are

discriminated according to user-defined criteria can be propelled to a height where the laminar flow has a different direction. Due to contribution of fluid flow a cell catapulted up would not necessarily travel along a straight vertical line, i.e. the path may be parabolic. Hence, machine vision can also be used to track the particle's lateral position and update the trap locations, similar to how CP trapped particles are stabilized.

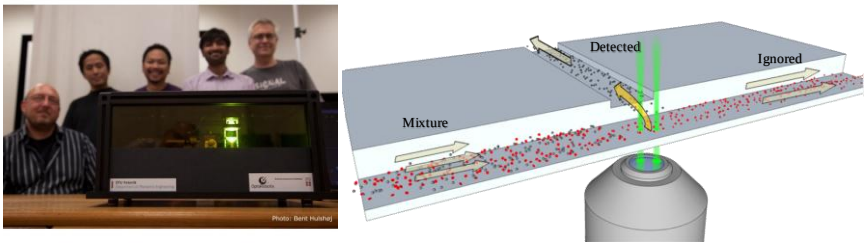

Figure 6.6. The table top cell-BOCS has a base that is roughly A3 in size (45cm x 30cm) (a). The cell-BOCS sorting mechanism depicting two laminar streams displaced in height. The lower stream contains a mixture of cells. Detected cells are pushed up to the other stream (b).

One of the challenges in active cell sorting is the lessened responsiveness due to the low refractive index contrast between cells and the fluid. We previously demonstrated programmable optical sorting using intense optical spikes generated by matched filtering Generalized Phase Contrast (mGPC) implemented with a high end SLM [47]. In Chapter 4, we have also demonstrated that much cheaper LCoS projectors can also be utilized for beam shaping based on mGPC. The compactness of current "pico" projectors allows it to be conveniently integrated in similarly compact optical setups. Being a consumer electronic device, display projectors also have the advantage of being much easier to acquire. Hence, given the ability to gather more optical power per area and its tolerance to imperfections in cheaper SLMs, mGPC may also reduce the cost of the cell-BOCS.

Appendix 1: Abbreviations

2PP. Two photon photopolymerization

BWS. BioPhotonics Workstation

CGH. Computer gernerated hologram

CP. Counter-propagating

cTP. Correlation Target Pattern

FDTD. Finite difference time domain

FFT. Fast Fourier Transform

GPC. Generalized Phase Contras

GS. Gerchbgerg-Saxton

HOT. Holographic Optical Tweezers

LCoS. Liquid crystal on silicon

mGPC. Matched filtering Generalized Phase Contrast

MOM. Micro Optical Magnifier

PCF. Phase Contrast Filter

POC. Phase-only correlation

SLM. Spatial light modulator

WOW. Wave-guided Optical Waveguide

Appendix 2: Related Math

To avoid deviating too much, some topics, although frequently referred to, were not included in the discussions. They are thus presented here for a quick reference.

The Airy function

A circular amplitude distribution with radius, *R*, and a uniform phase would have a Fourier transform described by the Airy function [48].

$$F\{\mathrm{circ}(R)\} = \frac{J_1(2\pi R\rho)}{\rho} \tag{A.1}$$

where J_1 is the Bessel function of the first kind, order 1 and ρ is the radial coordinate at the Fourier plane. Using MATLAB's besselj function, an analytic calculation of this diffraction pattern for an *N*x*N* array, indexed by *i* and *j*, with the radius *R*, now measured in number of samples, can be performed using

$$\begin{cases} R\dfrac{\mathrm{besselj}(1,2\pi R\rho)}{\rho}, & \rho \neq 0 \\ \pi R^2, & \rho = 0 \end{cases} \tag{A.2}$$

Where, the scaling of ρ now depends on *N* and relates to the DFT array indices by:

$$\rho(i,j) = \frac{1}{N}\sqrt{(i - N/2 - 1)^2 + (j - N/2 - 1)^2} \tag{A.3}$$

We also note that the zero[th] order is simply the integrated area of the input circle, thus conveniently handling the discontinuity. Figure A2.1 shows an analytically calculated Airy function superposed to a similar result from a 2D discrete Fourier transform.

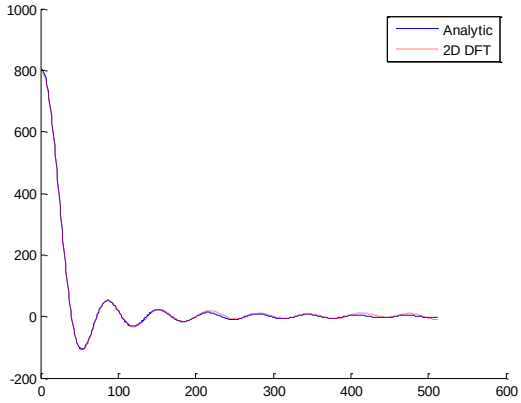

Figure A2.1. DFT based and analytic Airy function. The DFT is performed on a 1024x1024 array with a circle of radius R = 16. Deviations of the DFT values caused by aliasing are visible at greater radial positions.

Numerically solved zeros of the Airy function

The zeroes of the Airy function were searched with a simple brute force MATLAB routine that multiplies adjacent values of a function, similar to bisection root finding methods. A negative (or zero) product from adjacent values indicates a zero crossing. The first 47 zeroes are shown here. These zeroes are typically more than enough for filter fabrication since most of the light energy is contained within the first several zero crossings or filter rings. Nonetheless, having more rings helps in alignment as they give visual cues to where the center is located.

Table A2.1. Numerically obtained zeroes of the Airy function

1	0.609834945636981	**17**	8.62389870613809	**33**	16.6244286432072
2	1.11656529720178	**18**	9.12395904866947	**34**	17.1244453249718
3	1.61915774208977	**19**	9.62401312216452	**35**	17.6244610602748
4	2.12053143190384	**20**	10.1240618553477	**36**	18.1244759274360
5	2.62138218844666	**21**	10.6241060020749	**37**	18.6244899963749
6	3.12196084493967	**22**	11.1241461806923	**38**	19.1245033296864
7	3.62237993436075	**23**	11.6241829032399	**39**	19.6245159836010
8	4.12269745697849	**24**	12.1242165972130	**40**	20.1245280087564
9	4.62294634248536	**25**	12.6242476224341	**41**	20.6245394508762
10	5.12314667436933	**26**	13.1242762838995	**42**	21.1245503513785
11	5.62331139744267	**27**	13.6243028418412	**43**	21.6245607477970
12	6.12344923056284	**28**	14.1243275195890	**44**	22.1245706743425
13	6.62356626108820	**29**	14.6243505100297	**45**	22.6245801621372
14	7.12366686789291	**30**	15.1243719804735	**46**	23.1245892396589
15	7.62375428151724	**31**	15.6243920768432	**47**	23.6245979329517
16	8.12383093734445	**32**	16.1244109269264		

For an NxN 2D FFT of a circle with radius of R samples, these zeroes would be scaled by N/R. In experiments, the radius, R, would be in a unit of length, and the scaling would be $\lambda f/R$ which also depends on the focal length, f, of the Fourier lens and the wavelength, λ.

Beam propagation via angular spectrum method

Although the light distributions at the front and back focal planes of a lens can immediately be obtained via 2D Fourier transforms, obtaining distributions as light propagates away these planes requires a more general propagation calculation. We use the angular spectrum method that effectively decomposes a complex field into its constituent plane waves, applies respective phase shifts to these plane waves, and then recombines the phase shifted plane waves. This approach exploits superposition and relies on the fact that a plane wave only requires a phase shift to determine its state at a different location. Assuming propagation along z, we use the z component of the wave vector

$$k_z(i,j) = \sqrt{k_0^2 - [k_x^2(i) + k_y^2(j)]} \tag{A.4}$$

where $k_0 = 2\pi/\lambda$. The k_x and k_y components are obtained from a (NxN) 2D Fourier transform

$$k_x(i) = \left(i - \frac{N}{2} - 1\right)\frac{N_\lambda}{N}k_0 \text{ and } k_y(j) = \left(j - \frac{N}{2} - 1\right)\frac{N_\lambda}{N}k_0 \tag{A.5}$$

where i and j are matrix indices in the 2D FFT data and N_λ, is the number of samples per wavelength. To propagate to z, a lens-like phase distribution, $k_z(i,j)z$, is then applied at the Fourier plane in a similar manner that the GPC or mGPC phase filters are applied.

When using discrete FFTs, the tricky part is identifying the proper scaling in the discrete Fourier domain. Nonetheless this could be traced back noting that the highest frequency identified in the Fourier domain (along one axis) corresponds to the smallest wave that can be defined with the system's sampling. This corresponds to two data points minimally representing the rise and fall of an oscillation. This also corresponds to the Nyquist sampling frequency limit.

Bibliography

1. M. Mansuripur, "The Van Leeunhoek Microscope," Optics and Photonics News **10**, 39–42 (1999).

2. F. M. Grimaldi, *Physico Mathesis De Lumine, Coloribus, Et Iride, Aliisque Annexis Libri Duo* (1665), pp. 1–11.

3. M. Padgett and R. Di, "Holographic optical tweezers and their relevance to lab on chip devices †," Lab Chip **11**, 1196–1205 (2011).

4. P. J. Rodrigo, R. L. Eriksen, V. R. Daria, and J. Glückstad, "Interactive light-powered lab-on-a-chip: simultaneous actuation of microstructures by optical manipulation," in *Society of Photo-Optical Instrumentation Engineers (SPIE) Conference Series*, A. Rodriguez-Vazquez, D. Abbott, and R. Carmona, eds. (2003), Vol. 5119, pp. 54–59.

5. J. Ando, G. Bautista, N. Smith, K. Fujita, and V. R. Daria, "Optical trapping and surgery of living yeast cells using a single laser," Review of Scientific Instruments **79**, 103705 (2008).

6. E. Papagiakoumou, F. Anselmi, A. Bègue, V. de Sars, J. Glückstad, E. Y. Isacoff, and V. Emiliani, "Scanless two-photon excitation of channelrhodopsin-2," Nature Methods **7**, 848–854 (2010).

7. M. A. Go, C. Stricker, S. Redman, H.-A. Bachor, and V. R. Daria, "Simultaneous multi-site two-photon photostimulation in three dimensions.," Journal of Biophotonics **5**, 745–53 (2012).

8. J. Glückstad and D. Z. Palima, *Generalized Phase Contrast: Applications in Optics and Photonics* (Springer Series in Optical Sciences, 2009).

9. N. Arneborg, H. Siegumfeldt, G. H. Andersen, P. Nissen, V. R. Daria, P. J. Rodrigo, and J. Glückstad, "Interactive optical trapping shows that confinement is a determinant of growth in a mixed yeast culture.," FEMS Microbiology Letters **245**, 155–9 (2005).

10. A. Bañas, D. Palima, and J. Glückstad, "Matched-filtering generalized phase contrast using LCoS pico-projectors for beam-forming.," Optics Express **20**, 9705–12 (2012).

11. A. Bañas, T. Aabo, D. Palima, and J. Glückstad, "Matched filtering Generalized Phase Contrast using binary phase for dynamic spot- and line patterns in biophotonics and structured lighting," Optics Express **21**, 388–394 (2013).

12. Y. Hayasaki, M. Itoh, T. Yatagai, and N. Nishida, "Nonlnechanical Optical Manipulation of Microparticle Usillg Spatial Light Modulator," Optical Review **6**, 24–27 (1999).

13. G. Thalhammer, R. Steiger, S. Bernet, and M. Ritsch-Marte, "Optical macro-tweezers: trapping of highly motile micro-organisms," Journal of Optics **13**, 044024 (2011).

14. P. J. Rodrigo, L. Kelemen, D. Palima, C. A. Alonzo, P. Ormos, and J. Glückstad, "Optical microassembly platform for constructing reconfigurable microenvironments for biomedical studies," Optics Express **17**, 6578–83 (2009).

15. A. Ashkin, "Acceleration and Trapping of Particles by Radiation Pressure," Physical Review Letters **24**, 156–159 (1970).

16. D. Palima and J. Glückstad, "Comparison of generalized phase contrast and computer generated holography for laser image projection," Optics Express **16**, 5338–49 (2008).

17. A. Bañas, D. Palima, S. Tauro, and J. Glückstad, "Optimizing Light-Matter Interaction on the BioPhotonics Workstation," Optics and Photonics News **4**, 39 (2010).

18. D. G. Grier, "A revolution in optical manipulation," Nature **424**, 810–6 (2003).

19. P. J. Rodrigo, V. R. Daria, and J. Glückstad, "Four-dimensional optical manipulation of colloidal particles," Applied Physics Letters **86**, 074103 (2005).

20. S. Kawata, H. B. Sun, T. Tanaka, and K. Takada, "Finer features for functional microdevices," Nature **412**, 697–8 (2001).

21. P. Galajda and P. Ormos, "Complex micromachines produced and driven by light," Applied Physics Letters **78**, 249 (2001).

22. P. J. Rodrigo, L. Kelemen, C. A. Alonzo, I. R. Perch-Nielsen, J. S. Dam, P. Ormos, and J. Glückstad, "2D optical manipulation and assembly of shape-complementary planar microstructures.," Optics Express **15**, 9009–14 (2007).

23. D. B. Phillips, G. M. Gibson, R. Bowman, M. J. Padgett, S. Hanna, D. M. Carberry, M. J. Miles, and S. H. Simpson, "An optically actuated surface scanning probe," Optics Express **20**, 29679–29693 (2012).

24. M. R. Pollard, S. W. Botchway, B. Chichkov, E. Freeman, R. N. J. Halsall, D. W. K. Jenkins, I. Loader, A. Ovsianikov, A. W. Parker, R. Stevens, R. Turchetta, A. D. Ward, and M. Towrie, "Optically trapped probes with nanometer-scale tips for femto-Newton force measurement," New Journal of Physics **12**, 113056 (2010).

25. D. Palima, A. R. Bañas, G. Vizsnyiczai, L. Kelemen, P. Ormos, and J. Glückstad, "Wave-guided optical waveguides," Optics Express **20**, 2004–14 (2012).

26. H.-U. Ulriksen, J. Thogersen, S. Keiding, I. R. Perch-Nielsen, J. S. Dam, D. Z. Palima, H. Stapelfeldt, and J. Gluckstad, "Independent trapping, manipulation and characterization by an all-optical biophotonics workstation," Journal of the European Optical Society: Rapid Publications **3**, (2008).

27. S. Tauro, A. Bañas, D. Palima, and J. Glückstad, "Experimental demonstration of Generalized Phase Contrast based Gaussian beam-shaper," Optics Express **19**, 7106–11 (2011).

28. P. J. Rodrigo, L. Gammelgaard, P. Bøggild, I. Perch-Nielsen, and J. Glückstad, "Actuation of microfabricated tools using multiple GPC-based counterpropagating-beam traps.," Optics Express **13**, 6899–904 (2005).

29. A. Bañas, T. Aabo, D. Palima, and J. Glückstad, "Using pico-LCoS SLMs for high speed cell sorting," in *Proceedings of SPIE*, K. Dholakia and G. C. Spalding, eds. (2012), Vol. 8458, p. 845838.

30. P. J. Smith, C. M. Taylor, A. J. Shaw, and E. M. McCabe, "Programmable array microscopy with a ferroelectric liquid-crystal spatial light modulator," Applied Optics **39**, 2664–9 (2000).

31. E. C. Samson and C. M. Blanca, "Dynamic contrast enhancement in widefield microscopy using projector-generated illumination patterns," New Journal of Physics **9**, 363–363 (2007).

32. K. M. Johnson, D. J. McKnight, and I. Underwood, "Smart spatial light modulators using liquid crystals on silicon," IEEE Journal of Quantum Electronics **29**, 699–714 (1993).

33. J. M. Younse, "Projection display systems based on the Digital Micromirror Device (DMD)," in *Proc. SPIE 2641, Microelectronic Structures and Microelectromechanical Devices for Optical Processing and Multimedia Applications* (1995), Vol. 2641, pp. 64–75.

34. J. Liesener, M. Reicherter, T. Haist, and H. J. Tiziani, "Multi-functional optical tweezers using computer-generated holograms," **185**, 77–82 (2000).

35. G. Sinclair, P. Jordan, J. Leach, M. J. Padgett, and J. Cooper, "Defining the trapping limits of holographical optical tweezers," Journal of Modern Optics **51**, 409–414 (2004).

36. D. Palima and V. R. Daria, "Holographic projection of arbitrary light patterns with a suppressed zero-order beam," Applied Optics **46**, 4197–201 (2007).

37. P. Korda, G. C. Spalding, E. R. Dufresne, and D. G. Grier, "Nanofabrication with holographic optical tweezers," Review of Scientific Instruments **73**, 1956 (2002).

38. I. Moreno, J. Campos, C. Goreck, and M. J. Yzuel, "Effects of amplitude and phase mismatching errors in the generation of a kinoform for pattern recognition," Japanese journal of applied physics **34**, 6423–6432 (n.d.).

39. R. W. Gerchberg and W. O. Saxton, "A practical algorithm for the determination of the phase from image and diffraction plane pictures," Optik **35**, 237–246 (1972).

40. J. R. Fienup, "Phase retrieval algorithms: a comparison," Applied optics **21**, 2758–69 (1982).

41. N. Masuda, T. Ito, T. Tanaka, A. Shiraki, and T. Sugie, "Computer generated holography using a graphics processing unit," Optics Express **14**, 603–8 (2006).

42. G. Thalhammer, R. W. Bowman, G. D. Love, M. J. Padgett, and M. Ritsch-Marte, "Speeding up liquid crystal SLMs using overdrive with phase change reduction.," Optics express **21**, 1779–97 (2013).

43. K. Dholakia and T. Čižmár, "Shaping the future of manipulation," Nature Photonics **5**, 335–342 (2011).

44. M. A. Go, P.-F. Ng, H. a Bachor, and V. R. Daria, "Optimal complex field holographic projection.," Optics letters **36**, 3073–5 (2011).

45. H. O. Bartelt, "Applications of the tandem component: an element with optimum light efficiency.," Applied optics **24**, 3811 (1985).

46. J. L. Horner and P. D. Gianino, "Phase-only matched filtering," Applied Optics **23**, 812 (1984).

47. I. Perch-Nielsen, D. Palima, J. S. Dam, and J. Glückstad, "Parallel particle identification and separation for active optical sorting," Journal of Optics A: Pure and Applied Optics **11**, 034013 (2009).

48. J. Goodman, *Introduction to Fourier Optics*, 3rd ed. (Roberts and Company Publishers, 2004).

49. T. Čižmár, V. Garcés-Chávez, K. Dholakia, and P. Zemánek, "Optical conveyor belt for delivery of submicron objects," Applied Physics Letters **86**, 174101 (2005).

50. D. Palima, A. R. Bañas, G. Vizsnyiczai, L. Kelemen, T. Aabo, P. Ormos, and J. Glückstad, "Optical forces through guided light deflections," **21**, 6578–6583 (2013).

51. G. A. Swartzlander, T. J. Peterson, A. B. Artusio-Glimpse, and A. D. Raisanen, "Stable optical lift," Nature Photonics **5**, 48–51 (2011).

52. A. Ashkin, "Forces of a single-beam gradient laser trap on a dielectric sphere in the ray optics regime," Methods in cell biology **55**, 1–27 (1998).

53. G. C. Spalding, J. Courtial, and R. Di Leonardo, *Holographic Optical Tweezers* (n.d.).

54. J. E. Curtis, B. A. Koss, and D. G. Grier, "Dynamic holographic optical tweezers," **207**, 169–175 (2002).

55. C. Mio and D. W. M. Marr, "Optical Trapping for the Manipulation of Colloidal Particles," Advanced Materials **12**, 917–920 (2000).

56. J. Yamamoto and T. Iwai, "Spatial Stability of Particles Trapped by Time-Division Optical Tweezers," International Journal of Optomechatronics **3**, 253–263 (2009).

57. P. a Kirkby, K. M. N. Srinivas Nadella, and R. A. Silver, "A compact Acousto-Optic Lens for 2D and 3D femtosecond based 2-photon microscopy.," Optics express **18**, 13721–45 (2010).

58. T. Čižmár, M. Mazilu, and K. Dholakia, "In situ wavefront correction and its application to micromanipulation," Nature Photonics **4**, 388–394 (2010).

59. S. Bianchi and R. Di Leonardo, "Real-time optical micro-manipulation using optimized holograms generated on the GPU," Computer Physics Communications **181**, 1444–1448 (2010).

60. M. K. Kreysing, T. Kießling, A. Fritsch, J. R. Guck, and A. K. Josef, "The optical cell rotator," Optics Express **16**, 912–914 (2008).

61. C. Liberale, P. Minzioni, F. Bragheri, F. De Angelis, E. Di Fabrizio, and I. Cristiani, "Miniaturized all-fibre probe for three-dimensional optical trapping and manipulation," Nat Photon **1**, 723–727 (2007).

62. M. Pitzek, R. Steiger, G. Thalhammer, S. Bernet, and M. Ritsch-Marte, "Optical mirror trap with a large field of view," Optics Express **17**, 19414–23 (2009).

63. S. Zwick, T. Haist, Y. Miyamoto, L. He, M. Warber, A. Hermerschmidt, and W. Osten, "Holographic twin traps," Journal of Optics A: Pure and Applied Optics **034011**, (2009).

64. R. Bowman, A. Jesacher, G. Thalhammer, G. Gibson, M. Ritsch-Marte, and M. Padgett, "Position clamping in a holographic counterpropagating optical trap.," Optics express **19**, 9908–14 (2011).

65. M. Woerdemann, K. Berghoff, and C. Denz, "Dynamic multiple-beam counter-propagating optical traps using optical phase-conjugation," **18**, 7968–7973 (2010).

66. P. J. Rodrigo, I. R. Perch-Nielsen, and J. Glückstad, "Three-dimensional forces in GPC-based counterpropagating-beam traps," Optics Express **14**, 5812–22 (2006).

67. N. Bellini, K. C. Vishnubhatla, F. Bragheri, L. Ferrara, P. Minzioni, R. Ramponi, I. Cristiani, and R. Osellame, "Femtosecond laser fabricated monolithic chip for optical trapping and stretching of single cells," Optics Express **18**, 4679–88 (2010).

68. "File:Optical cell rotator.png," http://en.wikipedia.org/wiki/File:Optical_cell_rotator.png.

69. D. Palima, T. B. Lindballe, M. V Kristensen, S. Tauro, A. Bañas, H. Stapelfeldt, S. R. Keiding, and J. Glückstad, "Counter-propagating patterns in the biophotonics workstation: getting more out of light for trapping and manipulation," in *Proceedings of SPIE* (2010), Vol. 7762, p. 77620U.

70. T. Aabo, A. R. Banás, J. Glückstad, H. Siegumfeldt, and N. Arneborg, "BioPhotonics workstation: a versatile setup for simultaneous optical

manipulation, heat stress, and intracellular pH measurements of a live yeast cell," The Review of scientific instruments **82**, 083707 (2011).

71. J. S. Dam, P. J. Rodrigo, I. R. Perch-Nielsen, C. A. Alonzo, and J. Glückstad, "Computerized “drag-and-drop” alignment of GPC-based optical micromanipulation system," Optics Express **15**, 1923–31 (2007).

72. J. S. Dam, P. J. Rodrigo, I. R. Perch-Nielsen, and J. Glückstad, "Fully automated beam-alignment and single stroke guided manual alignment of counter-propagating multi-beam based optical micromanipulation systems," Optics Express **15**, 7968–73 (2007).

73. A. van der Horst, P. D. J. van Oostrum, A. Moroz, A. van Blaaderen, and M. Dogterom, "High trapping forces for high-refractive index particles trapped in dynamic arrays of counterpropagating optical tweezers," Applied optics **47**, 3196–202 (2008).

74. A. Isomura, N. Magome, M. I. Kohira, and K. Yoshikawa, "Toward the stable optical trapping of a droplet with counter laser beams under microgravity," Chemical Physics Letters **429**, 321–325 (2006).

75. A. Ashkin and J. M. Dziedzic, "Observation of Radiation-Pressure Trapping of Particles by Alternating Light Beams," Phys. Rev. Lett. **54**, 1245–1248 (1985).

76. S. Tauro, A. Bañas, D. Palima, and J. Glückstad, "Dynamic axial stabilization of counter-propagating beam-traps with feedback control," Optics Express **18**, 18217–22 (2010).

77. T. B. Lindballe, M. V. Kristensen, A. P. Kylling, D. Z. Palima, J. Gluckstad, S. R. Keiding, and H. Stapelfeldt, "Three-dimensional imaging and force characterization of multiple trapped particles in low NA counterpropagating optical traps," Journal of the European Optical Society: Rapid Publications **6**, (2011).

78. T. Čižmár and K. Dholakia, "Tunable Bessel light modes: engineering the axial propagation," Optics Express **17**, 12688–12700 (2009).

79. A. R. Bañas, D. Palima, and J. Glückstad, "Robust and Low-Cost Light Shaping," Optics and Photonics News **23**, 50 (2012).

80. D. Palima, C. A. Alonzo, P. J. Rodrigo, and J. Glückstad, "Generalized phase contrast matched to Gaussian illumination," Optics Express **15**, 11971–7 (2007).

81. M. Guizar-Sicairos and J. C. Gutiérrez-Vega, "Computation of quasi-discrete Hankel transforms of integer order for propagating optical wave fields," Journal of the Optical Society of America. A, Optics, image science, and vision **21**, 53–8 (2004).

82. R. Bowman, V. D'Ambrosio, E. Rubino, O. Jedrkiewicz, P. Trapani, and M. J. Padgett, "Optimisation of a low cost SLM for diffraction efficiency and ghost order suppression," The European Physical Journal Special Topics **199**, 149–158 (2011).

83. A. Martínez-García, I. Moreno, M. M. Sánchez-López, and P. García-Martínez, "Operational modes of a ferroelectric LCoS modulator for displaying binary polarization, amplitude, and phase diffraction gratings," Applied Optics **48**, 2903–14 (2009).

84. A. Martínez, N. Beaudoin, I. Moreno, M. D. M. Sánchez-López, and P. Velásquez, "Optimization of the contrast ratio of a ferroelectric liquid crystal optical modulator," Journal of Optics A: Pure and Applied Optics **8**, 1013–1018 (2006).

85. K. Guttag, J. Lund, and C. Waller, *854x600 Pixel LCOS Microdisplay with 5.4uM Pixel Pitch for Pico-Projectors* (n.d.).

86. I. Perch-Nielsen, D. Palima, J. S. Dam, and J. Glückstad, "Parallel particle identification and separation for active optical sorting," Journal of Optics A: Pure and Applied Optics **11**, 034013 (2009).

87. P. Marks, "The many flavours of printing in 3D," New Scientist **211**, 18 – (2011).

88. "Nanoscribe," http://www.nanoscribe.de/.

89. D. Tan, Y. Li, F. Qi, H. Yang, Q. Gong, X. Dong, and X. Duan, "Reduction in feature size of two-photon polymerization using SCR500," Applied Physics Letters **90**, 071106 (2007).

90. S. Maruo and J. T. Fourkas, "Recent progress in multiphoton microfabrication," Laser & Photonics Review **2**, 100–111 (2008).

91. A. Búzás, L. Kelemen, A. Mathesz, L. Oroszi, G. Vizsnyiczai, T. Vicsek, and P. Ormos, "Light sailboats: Laser driven autonomous microrobots," Applied Physics Letters **101**, 041111 (2012).

92. D. M. Carberry, S. H. Simpson, J. a Grieve, Y. Wang, H. Schäfer, M. Steinhart, R. Bowman, G. M. Gibson, M. J. Padgett, S. Hanna, and M. J. Miles, "Calibration of optically trapped nanotools," Nanotechnology **21**, 175501 (2010).

93. L. Ikin, D. M. Carberry, G. M. Gibson, M. J. Padgett, and M. J. Miles, "Assembly and force measurement with SPM-like probes in holographic optical tweezers," New Journal of Physics **11**, 023012 (2009).

94. J. L. Hernández-Pozos, M. Lee, L. I. Vera-Robles, A. Campero, and K. Dholakia, "Controlled three-dimensional manipulation of vanadium oxide nanotubes with optical tweezers," Applied Physics Letters **93**, 243107 (2008).

95. J. Glückstad, A. Bañas, T. Aabo, and D. Palima, "Structure-mediated micro-to-nano coupling using sculpted light and matter," in *Proceedings of SPIE* (2012), Vol. 8424, p. 84241L.

96. D. Palima, A. Bañas, J. Glückstad, G. Vizsnyiczai, L. Kelemen, and P. Ormos, "Mobile Waveguides: Freestanding Waveguides Steered by Light," Opt. Photon. News **23**, 27 (2012).

97. D. K. Gramotnev and S. I. Bozhevolnyi, "Plasmonics beyond the diffraction limit," Nature Photonics **4**, 83–91 (2010).

98. D. F. P. Pile and D. K. Gramotnev, "Adiabatic and nonadiabatic nanofocusing of plasmons by tapered gap plasmon waveguides," Applied Physics Letters **89**, 041111 (2006).

99. S. T. Huntington, B. C. Gibson, J. Canning, K. Digweed-Lyytikäinen, J. D. Love, and V. Steblina, "A fractal-based fibre for ultra-high throughput optical probes," Optics Express **15**, 2468–75 (2007).

100. A. Lewis, M. Isaacson, R. E. Betzig, A. Arbor, and A. Harootunian, "Near field scanning optical microscopy," U.S. patent 4917462 (1990).

101. G. P. Agrawal, *Lightwave Technology: Components and Devices* (Wiley, 2004).

102. K. S. Yee, "Numerical solution of initial boundary value problems involving maxwell's equations in isotropic media," IEEE Transactions on Antennas and Propagation **14**, 302–307 (1966).

103. D. B. Davidson and R. W. Ziolkowski, "Body-of-revolution finite-difference time-domain modeling of space-time focusing by a three-dimensional lens," Journal of the Optical Society of America A **11**, 1471 (1994).

104. G. Mur, "Absorbing Boundary Conditions for the Finite-Difference Approximation of the Time-Domain Electromagnetic-Field Equations," IEEE Transactions on Electromagnetic Compatibility **EMC-23**, 377–382 (1981).

105. A. Taflove and S. C. Hagness, *Computational Electrodynamics: The Finite-Difference Time-Domain Method*, 3rd ed. (Artech House, 2005).

106. M. E. Friese, T. A. Nieminen, N. R. Heckenberg, and H. Rubinsztein-Dunlop, "Optical alignment and spinning of laser-trapped microscopic particles," Nature **394**, 348–350 (1998).

107. N. B. Simpson, K. Dholakia, L. Allen, and M. J. Padgett, "Mechanical equivalence of spin and orbital angular momentum of light: an optical spanner," Optics Letters **22**, 52–4 (1997).

108. D. Palima and J. Glückstad, "Gearing up for optical microrobotics: micromanipulation and actuation of synthetic microstructures by optical forces," Laser & Photonics Reviews **17**, n/a–n/a (2012).

109. A. T. O'Neil, I. MacVicar, L. Allen, and M. J. Padgett, "Intrinsic and Extrinsic Nature of the Orbital Angular Momentum of a Light Beam," Physical Review Letters **88**, 053601 (2002).

110. V. R. Daria, D. Z. Palima, and J. Glückstad, "Optical twists in phase and amplitude," Optics Express **19**, 476–81 (2011).

111. W. K. H. Panofsky and M. Phillips, *Classical Electricity and Magnetism*, 2nd ed. (Dover Publications, 2005).

112. D. C. Benito, S. H. Simpson, and S. Hanna, "FDTD simulations of forces on particles during holographic assembly," Optics Express **16**, 2942–57 (2008).

113. L. Kelemen, S. Valkai, and P. Ormos, "Integrated optical motor," Applied Optics **45**, 2777–80 (2006).

114. J. Glückstad, "Optical manipulation: Sculpting the object," Nature Photonics **5**, 7–8 (2011).

115. T. Matsuoka, M. Nishi, M. Sakakura, K. Miura, K. Hirao, D. Palima, S. Tauro, A. Bañas, and J. Glückstad, "Functionalized 2PP structures for the BioPhotonics Workstation," in *Proceedings of SPIE* (2011), p. 79500Q.

116. B. L. Aekbote, J. Jacak, G. J. Schütz, E. Csányi, Z. Szegletes, P. Ormos, and L. Kelemen, "Aminosilane-based functionalization of two-photon polymerized 3D SU-8 microstructures," European Polymer Journal **48**, 1745–1754 (2012).

117. A. Bañas, G. Vizsnyiczai, A. Búzás, D. Palima, L. Kelemen, P. Ormos, and J. Glückstad, "Fabrication and optical trapping of handling structures for re-configurable microsphere magnifiers," in *Proceedings of SPIE* (2013), p. 86370Y.

118. S. Manos, M. C. J. Large, and L. Poladian, "Evolutionary design of single-mode microstructured polymer optical fibres using an artificial embryogeny representation," Proceedings of the 2007 GECCO conference companion on Genetic and evolutionary computation - GECCO '07 2549 (2007).

119. D. S. Ramrkahyani, G. A. Lesieutre, M. Frecker, S. Bharti, S. Ratio, and N. Engineering, "Aircraft Structural Morphing using Tendon Actuated Compliant Cellular Trusses," in *45th AIAA/ASME/ASCE/AHS/ASC Structures, Structural Dynamics & Materials Conference* (2004), p. 1728.

120. M. Helal, L. Chen, L. Sun, and T. Chen, "Topology Optimization of a Three-Dimension Compliant Microgripper Using Multi-objective Compliance," 2009 IITA International Conference on Control, Automation and Systems Engineering (case 2009) 124–127 (2009).

121. Z. Wang, W. Guo, L. Li, B. Luk'yanchuk, A. Khan, Z. Liu, Z. Chen, and M. Hong, "Optical virtual imaging at 50 nm lateral resolution with a white-light nanoscope," Nature communications **2**, 218 (2011).

122. E. McLeod and C. B. Arnold, "Subwavelength direct-write nanopatterning using optically trapped microspheres," Nature nanotechnology **3**, 413–7 (2008).

123. B. Koss, S. Chowdhury, T. Aabo, S. K. Gupta, and W. Losert, "Indirect optical gripping with triplet traps," Journal of the Optical Society of America B **28**, 982 (2011).

124. A. Darafsheh, G. F. Walsh, L. Dal Negro, and V. N. Astratov, "Optical super-resolution by high-index liquid-immersed microspheres," Applied Physics Letters **101**, 141128 (2012).

125. D. Palima and J. Glückstad, "Gaussian to uniform intensity shaper based on generalized phase contrast," Optics Express **16**, 1507–16 (2008).

126. W. A. Bonner, H. R. Hulett, R. G. Sweet, and L. A. Herzenberg, "Fluorescence Activated Cell Sorting," Review of Scientific Instruments **43**, 404–409 (1972).

127. H. M. Shapiro, "The Cytometric Future: It Ain't Necessarily Flow!," Methods in Molecular Biology (Clifton, N.J.), **699**, 471–482 (2011).

128. X. Su, S. E. Kirkwood, M. Gupta, L. Marquez-curtis, Y. Qiu, A. Janowska-wieczorek, W. Rozmus, and Y. Y. Tsui, "Microscope-based label-free microfluidic cytometry," Optics Express **19**, 1573–1581 (2011).

129. H. Zhu, S. Mavandadi, A. F. Coskun, O. Yaglidere, and A. Ozcan, "Optofluidic fluorescent imaging cytometry on a cell phone," Analytical Chemistry **83**, 6641–7 (2011).

130. J. Glückstad, "Sorting particles with light," Nature Materials **3**, 9–10 (2004).

131. A. Bañas, D. Palima, F. Pedersen, and J. Glückstad, "Development of a compact Bio-Optofluidic Cell Sorter," in *Proceedings of SPIE Vol. 8274* (2012), Vol. 8274, p. 82740N.

132. "Syndiant SYL2043 Product Brief," http://syndiant.com/pdfs/SYL2043_ProductBrief.pdf.